

SAR IMAGE CLASSIFICATION OF FIRST-YEAR
ICE TYPES, BAY D'ESPOIR, NEWFOUNDLAND
AND LABRADOR

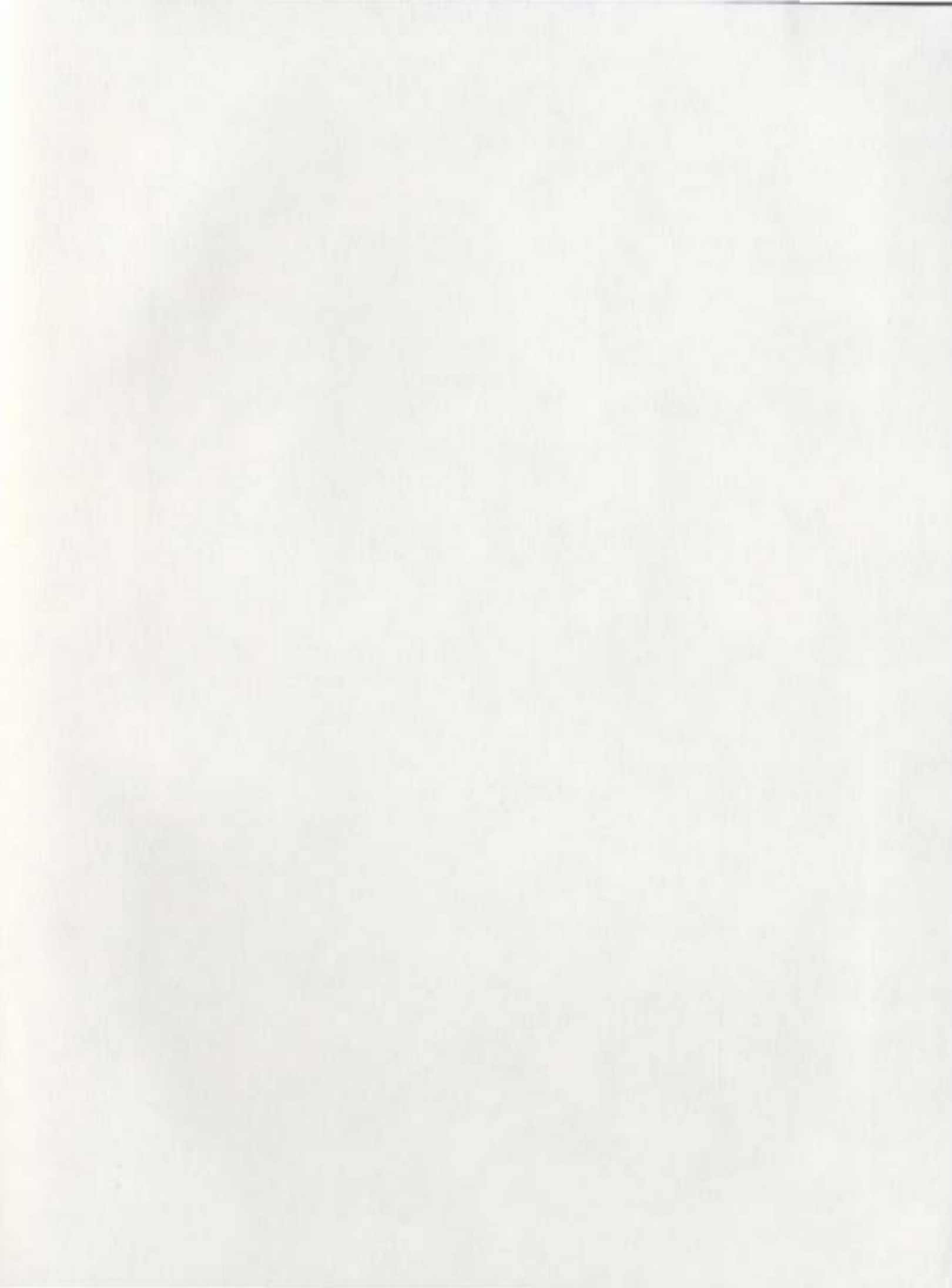
CENTRE FOR NEWFOUNDLAND STUDIES

**TOTAL OF 10 PAGES ONLY
MAY BE XEROXED**

(Without Author's Permission)

PAUL BRETT





SAR Image Classification of First-Year Ice Types, Bay d'Espoir, Newfoundland and Labrador

by

Paul Brett

A thesis submitted to the
School of Graduate Studies
in partial fulfillment of the
requirements for the degree of
Master of Science

Department of Geography
Memorial University of Newfoundland

©2004

St. John's

Newfoundland and Labrador



Library and
Archives Canada

Published Heritage
Branch

395 Wellington Street
Ottawa ON K1A 0N4
Canada

Bibliothèque et
Archives Canada

Direction du
Patrimoine de l'édition

395, rue Wellington
Ottawa ON K1A 0N4
Canada

Your file Votre référence

ISBN: 0-612-99056-7

Our file Notre référence

ISBN: 0-612-99056-7

NOTICE:

The author has granted a non-exclusive license allowing Library and Archives Canada to reproduce, publish, archive, preserve, conserve, communicate to the public by telecommunication or on the Internet, loan, distribute and sell theses worldwide, for commercial or non-commercial purposes, in microform, paper, electronic and/or any other formats.

The author retains copyright ownership and moral rights in this thesis. Neither the thesis nor substantial extracts from it may be printed or otherwise reproduced without the author's permission.

AVIS:

L'auteur a accordé une licence non exclusive permettant à la Bibliothèque et Archives Canada de reproduire, publier, archiver, sauvegarder, conserver, transmettre au public par télécommunication ou par l'Internet, prêter, distribuer et vendre des thèses partout dans le monde, à des fins commerciales ou autres, sur support microforme, papier, électronique et/ou autres formats.

L'auteur conserve la propriété du droit d'auteur et des droits moraux qui protège cette thèse. Ni la thèse ni des extraits substantiels de celle-ci ne doivent être imprimés ou autrement reproduits sans son autorisation.

In compliance with the Canadian Privacy Act some supporting forms may have been removed from this thesis.

While these forms may be included in the document page count, their removal does not represent any loss of content from the thesis.

Conformément à la loi canadienne sur la protection de la vie privée, quelques formulaires secondaires ont été enlevés de cette thèse.

Bien que ces formulaires aient inclus dans la pagination, il n'y aura aucun contenu manquant.

Abstract

Sea ice during spring melt and breakup can prove dangerous to infrastructure located in the coastal zone. Industries such as aquaculture, which houses much of its infrastructure in the near shore environment, are at the mercy of sea ice motion. Knowledge of the condition of ice during the melt season could allow such users of the coastal zone to plan against potential damage due to the premature breakup of the ice coverage.

Traditional methods of sea ice detection and classification have been limited to the open ocean and dedicated to problems associated with navigation. Their primary concern is in the identification of first-year ice, multi year ice and open water.

The use of second order texture measures, along with a new approach to histogram characterization, and neural network classification have allowed the classification of a fine beam mode RADARSAT image to map five sub classes of first-year sea ice - brash, puddle, flooded, rotten, snow covered, - and open water. Classification accuracies achieved are on the order of 60% with user's accuracies for several of the ice types approaching 100%

Acknowledgments

Most importantly I would like to thank my supervisor Dr. Élizabeth L. Simms for her never-ending support and guidance in this project. I also thank Dr. Jim Helbig, of the Department of Fisheries and Oceans Canada, for his supervisory committee work as well as his support in securing funding from the Canadian Space Agency for image acquisition and helicopter time. I am also grateful to Dr. Alvin Simms for the generous contribution of his time, especially during the editing phase of this document.

The analysis of images for this research was completed using the equipment of the Geographical Information and Analysis Laboratory (GEOIDAL) located in the Department of Geography, Memorial University.

Many thanks to the Canadian Centre for Remote Sensing for providing imagery through the Earth Observation Data Sets Program. Mr. Todd Pearson of Radarsat International provided important technical insight in the process of image acquisition planning. I am very appreciative of Dr. Langis Gagnon, who shed much valuable light on the processes of wavelet analysis.

Finally, I want to thank the faculty and staff of the Department of Geography, for their moral support and encouragement during my entire program

To all, Thanks.

Table of Contents

Abstract	ii
Acknowledgments.....	iii
Table of Contents	iv
List of Figures.....	vi
List of Tables	ix
1.0 Introduction.....	1
2.0 Background	6
2.1 SEA ICE TERMINOLOGY	7
2.2 REMOTE SENSING OF SEA ICE	9
2.3 ACTIVE MICROWAVE REMOTE SENSING OF SEA ICE.....	14
2.4 SAR SPECKLE REDUCTION	17
2.5 IMAGE TEXTURE.....	21
2.5.1 First order texture measures	22
2.5.2 Second Order texture measures	23
2.6 SAR IMAGE CLASSIFICATION FOR SEA ICE	26
3.0 Problems and research objectives.....	33
3.1 PROBLEMS	33
3.2 RESEARCH OBJECTIVES	35
4.0 Study area and data	36
4.1 STUDY AREA	36
4.2 DATA	38
5.0 Methodology	40
5.1 AERIAL SURVEY	40
5.1.1 Video assessment	42
5.1.2 Geometric correction of video.....	43
5.1.3 Training and verification data extraction	45
5.2 RADAR IMAGE PROCESSING.....	47
5.2.1 Radiometric calibration	49
5.2.2 Image geometric correction.....	49
5.2.3 Speckle reduction	50
5.2.4 Texture analysis.....	52
5.2.5 Histogram characterization.....	54
5.3 NEURAL NETWORK CLASSIFICATION	59
5.3.1 Neural network architecture	60
5.3.2 Training the neural network	61
5.3.3 Applying the classifier	62
5.4 CLASSIFICATION ACCURACY ASSESSMENT.....	63
6.0 Results	65
6.1 AERIAL SURVEY	65
6.1.2 Video geometric correction	66
6.1.3 Training and verification data extraction	68
6.2 RADAR IMAGE PROCESSING.....	72
6.2.1 Geometric correction.....	72
6.2.2 Speckle filtering	73
6.2.4 Texture analysis.....	76

6.2.4 Signature Statistics	84
6.3 NEURAL NETWORK CLASSIFICATION	94
6.4 CLASSIFICATION RESULTS	96
6.5 ACCURACY ASSESSMENT	103
6.5.1 Classification accuracy	103
6.5.2 Texture accuracies comparison	108
7.0 Discussion	115
7.1 AERIAL VIDEO RECONNAISSANCE	115
7.2 RADAR IMAGE PROCESSING.....	116
7.3 FIRST-YEAR ICE MAPPING CAPABILITIES	120
8.0 Conclusion	124
9.0 References	126

List of Figures

Figure 2.1 First-year ice sub-classification (WMO,1985)	9
Figure 2.2 Modified Rayleigh Criterion of RADARSAT Fine 3	16
Figure 2.3 Graphic representation of level 2 wavelet decomposition	19
Figure 2.4 Typical MLP neural network.....	30
Figure 4.1 Study area with radar image coverage.....	37
Figure 5.1 Video processing	41
Figure 5.2 Coastline with artificial grid.....	44
Figure 5.3 Radar, initial processing	48
Figure 5.4 Wavelet speckle filter procedure.	51
Figure 5.5 Angular second moment texture (d=3) histograms of ice types (a – f)	56
Figure 5.6 ASM d=3 histogram bin image (0.24 to 0.46).....	58
Figure 6.1 Original (a) and classified (b) Lampedois video frame.....	65
Figure 6.2 Classified aerial video bitmap mosaic	68
Figure 6.3 GCP selection and study area	73
Figure 6.4 Speckle reduced image (Daubechies 4, dc=2).....	75
Figure 6.5 Effects of displacement on the coefficient of variation, correlation texture. ..	76
Figure 6.6 Effect of displacement on correlation texture measure with three different window sizes, for snow cover.	78
Figure 6.7 Effect of filter size for SD texture measure, for snow cover.....	79
Figure 6.8 Effect of window size and displacement vector on texture measure for snow cover	81

Figure 6.9 Normalized training statistics for radar backscatter	85
Figure 6.10 Normalized training statistics for SD texture measure displacement of two	86
Figure 6.11 Normalized training statistics for ASM texture measure with displacement of three	87
Figure 6.12 Normalized training statistics for HOM texture measure with displacement of three	88
Figure 6.13 Normalized training statistics for ENT texture measure with displacement of three	89
Figure 6.14 Normalized training statistics for COR texture measure with displacement of three	90
Figure 6.15 Standard deviation histogram comparison	92
Figure 6.16 MLP Normalized total error for SD texture measure	95
Figure 6.17 Standard deviation ice classification results	97
Figure 6.18 Angular Second Moment ice classification results.....	98
Figure 6.19 Homogeneity ice classification results	99
Figure 6.20 Entropy ice classification results	100
Figure 6.21 Correlation ice classification results.....	101
Figure 6.22 User's accuracies across textures by class.....	110
Figure 6.23 Brash, class commission errors by texture measure	111
Figure 6.24 Open Water, class commission errors by texture measure.....	111
Figure 6.25 Puddle, class commission errors by texture measure	112
Figure 6.26 Snow Cover, class commission errors by texture measure	113
Figure 6.27 Flooded, class commission errors by texture measure	114

Figure 6.28 Rotten class commission errors by texture measure..... 114

List of Tables

Table 2.1 Spaceborne ice monitoring satellites	13
Table 2.2 Spaceborne ice monitoring satellite imaging characteristics	13
Table 4.1 Image characteristics.....	38
Table 5.1 WMO sea-ice nomenclature	42
Table 6.1 Aerial video ice description	66
Table 6.2 Geometric correction results for video frames.....	67
Table 6.3 Cross-tabulation results of training data and radar cluster analysis.....	69
Table 6.4 Sample size for each ice class	71
Table 6.5 Wavelet parameters.....	74
Table 6.6 Separability for COR texture measure at displacements of two and three	82
Table 6.7 Separability for ASM texture measure at displacements of two and three.....	83
Table 6.8 Separability for ENT texture measure at displacements of two and three.....	83
Table 6.9 Separability for HOM texture measure at displacements of two and three	83
Table 6.10 Separability for SD texture measure at displacements of two and three	84
Table 6.11 Optimum histogram bins for histogram characterization	91
Table 6.12 ASM database structure	93
Table 6.13 Bhattacharrya distance for backscattered and correlation texture images	93
Table 6.14 Bhattacharrya distance for correlation with the bin images included.....	93
Table 6.15 Neural network input channels	94
Table 6.16 MLP total error	96

Table 6.17 Percent total coverage of ice type as calculated by texture measures.....	102
Table 6.18 Standard deviation error matrix	104
Table 6.19 Angular second moment error matrix	106
Table 6.20 Homogeneity error matrix.....	107
Table 6.21 Entropy error matrix	107
Table 6.22 Correlation error matrix	108
Table 6.23 Texture measure accuracy comparison.....	108
Table 6.24 Z-value test for significance between Kappa.....	109
Table 7.1 Accuracy assessment of ASM texture measure with flooded and puddle combined	122

1.0 Introduction

Information concerning sea ice type and extent in the marine environment is of significant importance to its users. This information is needed to ensure safe and practical human activities in and around the ice. The coastal zone of the ocean is utilized for industrial, recreational, and commercial activities, and requires adequate information about ice. The salmonid aquaculture industry in the province of Newfoundland and Labrador is one such industry that is expanding and requires adequate environmental information to determine its practical and ecological expansion capacity. Ice effects on salmonid species kept in enclosures are of concern to the aquaculture industry, specifically, about the destruction of aquaculture infrastructure by moving ice during spring breakup.

In the aquaculture industry, fishes are held in cages that allow them to move freely about the water column and surface. The cages, which extend above the surface of the water, are susceptible to any movement of ice in their vicinity. A primary concern to aquaculturalists is the potential damage to these cages caused by the movement of ice.

The presence of ice in close vicinity to the cage is also detrimental to fish health. Water temperature is important in determining fish survival; the presence of ice may lower the water temperature below the lethal limit of the species. Salmonid are poikilotherms, whereby body temperature equals that of their surrounding environment.

Body temperature is directly related to metabolic activity, which drives immune responses, tissue repair, and digestion (Tlusty *et al.*, 1999). Fishes prefer to live at a standard environmental temperature (SET), the lower lethal limit of a SET is the lowest temperature in which the species can survive. For salmonid the lower lethal temperature limits are, for salmon –0.7 °C, for trout –0.8 °C, and for Arctic Char –0.95°C (Wheaton, 1987). Some species may be able to survive cold water, but direct contact of the fish with ice may cause freezing across the epidermis of the fish, resulting in death.

Ice around cages has been a problem in the Bay d'Espoir region of Newfoundland and Labrador. During the winter of 1987, an aquaculture site in Roti Bay experienced mass mortality of large salmon kept in sea pens (cages). Operators discovered many of the surviving fish swimming on their sides, and also noted the fish had suffered abrasions to the nostrils. As a result, the fish could not get enough air to fill their swim bladders used to equilibrate their buoyancy. The negative buoyancy experienced by the fish caused stress and eventually death (Tlusty *et al.*, 1999).

Aquaculturalists try to keep cages free of ice during most of the ice season. At the time of spring breakup as the ice cover melts, movement can result in cages being inundated with brash ice leading to all of the problems described above. Brash is a form of ice resulting from the break up of the consolidated mass; it consists of pieces of ice less than two meters across that is free to move by means of wind, wave, and current. At

any time the consolidated ice sheet can break in to brash particles, however as the ice cover melts less energy is needed.

Given the effects of ice on the salmonid species, the aquaculturalist requires information about ice conditions to ensure that proper measures are taken to reduce stress on the fish and mitigate damage to equipment of the aquaculture site. The use of ice surveys to determine the geographic distribution of ice type and concentration in potentially suitable aquaculture sites are required to ensure adequate protection of the infrastructure from ice. Aquaculture sites in coastal Newfoundland and Labrador are normally located adjacent to the shore and occupy an area of less than one square kilometer. These sites are distributed throughout the area to ensure adequate physical makeup, biological structure, oceanographic currents, as well as coastal topography to afford protection from ice damage. Due to the small areal extent and sparse distribution of operational and potential aquaculture sites, suitable ice surveys cannot be performed economically from ground based surveys. On the other hand, ice surveys have traditionally been conducted by aerial reconnaissance. Unfortunately these methods are expensive, time consuming, and are dependent on site accessibility as well as weather conditions.

Radar remote sensing can address the issues of aerial ice surveys, and acquire information about ice distribution and concentration in potential aquaculture sites. Specifically, Canada's synthetic aperture radar (SAR) satellite RADARSAT-1 is used in

this study. RADARSAT-1 has a steerable SAR antenna providing different look angles and image configurations. Radar provides its own source of radiation centered in the microwave portion of the electromagnetic spectrum, allowing all weather, as well as day and night illumination of a scene.

In radar imagery, the intensity of return of the incident radiation is dependent upon surface roughness properties of a feature as well as the dielectric properties of the feature. Differences in the surface roughness of ice cover, as well as differences in its texture will help differentiate ice types. These feature characteristics will relate to differences in radar backscatter, which can be integrated with other processing techniques to map ice types.

The purpose of this research is to develop methods for first-year ice classification in the coastal environment. The study area is the Bay d'Espoir region of Newfoundland and Labrador, an area that is extensively used for aquaculture and has experienced some of the problems posed by ice in a region used for aquaculture.

The background chapter (Chapter Two) introduces definitions of coastal ice types highlighting differences with respect to open sea ice. The concept of sea ice remote sensing is discussed including the nature of radar and optical remote sensing. Radar image processing for speckle reduction, texture analysis, and classification are discussed. Chapter Three introduces the problems of sea ice identification in the coastal zone and its

relevance to aquaculture. The objectives of this thesis are then stated. Chapter Four describes the Bay d'Espoir region of Newfoundland and Labrador, and the data used to develop the classification technique. The methodology employed in the fieldwork and the image analysis is described in Chapter Five. Explanation of the approach to aerial surveys and radar image processing are also presented. The results are presented and discussed in Chapter Six. Chapter seven discusses the results with respect to the success and shortfalls of the methodology. Chapter Eight concludes with a summary of the achievement of the research objectives and proposed approaches to take for further studies.

2.0 Background

Sea ice classification has been an integral part of remote sensing research for over 20 years. Knowledge of the extent, concentration and type of sea ice is important to many marine activities. With the growing recreational and commercial activity in the coastal zone, researchers have attempted to observe ice types and conditions with the purpose of gaining knowledge on typical ice conditions.

This chapter focuses on the early work of ice research with respect to sea ice detection and classification. It begins with sea ice naming conventions, then proceeds to preliminary identification work using optical remote sensing platforms, as well as microwave remote sensing of sea ice. The properties of sea ice during spring melt and breakup are discussed with respect to changes in their microwave signature.

A discussion of radar image analysis including image preprocessing and classification procedures, with the goal of ice cover identification, is presented. This is followed by a discussion of a speckle reduction methodology using wavelet analysis. The concept of image texture is introduced as an extension to the data structure of radar backscatter. Texture parameters will augment that data to permit image classification. Finally, current classification algorithms used in ice studies will be presented with further explanation of artificial neural networks (ANNs), as an alternative to traditional methods used for ice classification.

2.1 Sea Ice Terminology

Sea ice data are normally reported using the standards developed by the World Meteorological Organization (WMO). This universally accepted terminology and sea ice codes ensure consistency between observing countries for the international exchange of ice information. Since this study is concerned with first-year ice only the nomenclature for first-year ice will be discussed.

The subdivision of first-year ice will form the basis of the image classification of ice types. First-year ice, as a broad class, can be defined as sea ice of not more than one winter's growth, developing from young ice, with thickness from 30 cm to 2 m (WMO, 1985). First-year ice can be sub-classified based on thickness and stages of melt. As sea ice grows through different stages, it loses brine, and its surface becomes colder and rougher. In the presence of precipitation, the ice usually acquires a snow cover.

During the stages of development, sea ice can be characterized as follows,

New ice: Recently formed ice that includes frazil ice, grease ice, slush, shuga, ice rind, and dark and light nilas. These ice types are composed of ice crystals that are only weakly frozen together. New ice, as its name implies, is recently formed and has a thickness up to 10 cm.

Grey-ice: This category of ice includes young ice with thickness' of 10 to 15 cm. Grey-ice is less elastic than new ice and usually breaks on swells and rafts under pressure.

Grey-white ice: This form of ice has thickness' ranging between 15 to 30 cm. Under pressure, this type is more likely to ridge rather than raft.

First-year ice: Sea ice of not more than one winters growth, developing from young ice with thickness ranging from 30 cm to 2 m.

With the onset of melt, first-year ice can be further characterized by the presence or absence of standing water as well as the mechanical breakup of the existing ice structure (WMO, 1985). When temperatures rise above freezing, melting occurs and first-year ice goes through a series of stages of degradation, progressing from snow-covered to open water.

Snow-covered ice is the state of ice during most winter months where snow accumulates on top of the ice cover. For example the arrows in Figure 2.1 (a) indicate the presence of snow drifts on snow covered ice. As melting begins, the snow becomes saturated with water, forming puddles on the ice surface. The puddle ice type (Figure 2.1(b)) is characterized by an accumulation of water on top of the ice, mainly due to melting snow, or in the more advanced stages, also of ice. Further melting creates flooded ice (Figure 2.1 (c)), where sea ice has been flooded by melt-water or river water and is heavily loaded with water or wet snow. Continuation of the melting process leads to the creation of thaw holes (arrow in Figure 2.1 (d)), where holes in the ice are formed when surface puddles melt through. Next in the melt process is rotten ice (Figure 2.1 (e)) formed near the end of the cycle. It is characterized by sea ice that has become honeycombed with thaw holes and is in advanced stages of disintegration. During the melt process, if sufficient wind or wave action is present the ice mass may become broken apart into brash ice (Figure 2.1 (f)), defined as an accumulation of floating ice made up of fragments not more than 2 m across.

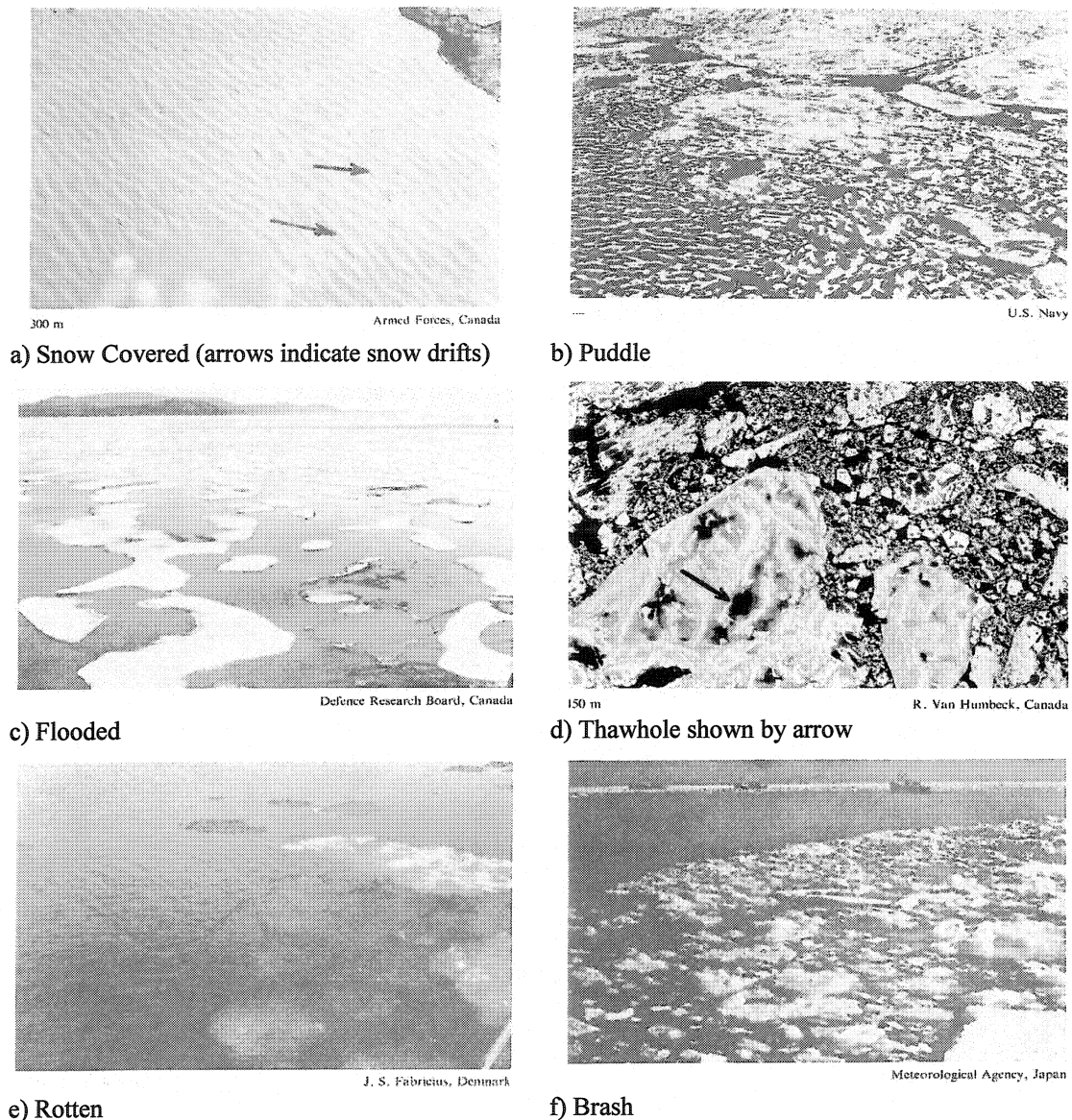


Figure 2.1 First-year ice sub-classification (WMO, 1985)

2.2 Remote sensing of sea ice

Sea ice monitoring is a well-established and organized activity in countries where sea ice occurs, because it has important impacts on transportation, climate, and coastal

zone activities. Data are obtained by several methods: aircraft or helicopter surveys, ship observations, reports from coastal and meteorological stations, data from drifting buoys and satellite data.

Visual reconnaissance of sea ice has played an important role in operational monitoring. Ship-based and fixed wing aircraft meteorological observations provide extensive information on ice type and extent. These ice identification observations are based on WMO standards. However the extent of these observations are restricted to areas of high ship traffic, or frequent fixed wing flights (Falkingham, 1992). This information is normally gathered at a central facility and dispatched to the marine community requiring information on sea ice conditions. In Canada, the primary provider of sea ice information is the Canadian Ice Service, Environment Canada.

Fixed wing aircraft have also been used with sensors mounted on them to provide digital based coverage of selected areas. High flying aircraft (6500 m) equipped with C-band and X-band synthetic aperture radar (SAR) and real aperture side looking radar (SLAR) have proved useful in sea ice monitoring (Melling, 1998). These sensors can provide resolutions in the range of 6 m, with swaths of approximately 19-50 km. While resolution is favorable for these sensors in ice mapping in the coastal zone, most users of ice information do not have the infrastructure or budget to commission aircraft over flights (Ramsay *et al.*, 1993).

The limited geographical coverage provided by visual reconnaissance and airborne systems indicates the requirement for spaceborne systems in the monitoring of sea ice. Tables 2.1 and 2.2 (adapted from Sandven *et al.*, 1998) identify the major spaceborne sensors employed in sea ice monitoring worldwide.

Until recently, spaceborne multi-channel passive microwave radiometers like the Special Sensor Microwave Imager (SSM/I) onboard the Defense Meteorological Satellite Program (DMSP) (Drobot and Anderson, 2000) were the principal satellite sensors used to determine ice concentration information and to distinguish first-year from multi-year ice and open water (Cavalieri *et al.*, 1984, Steffen *et al.*, 1992).

Early surveys established that there are three dominant marine surfaces in the Arctic; (i.) open water, (ii.) first-year ice, and (iii.) multi-year ice. These ice types could be discriminated from each other on the basis of their contrasting passive microwave signatures (Eppler *et al.*, 1994). These observations led to the operational algorithms presently used to derive ice concentration information from passive microwave satellite data. Subsequent work during several ice experiment projects including the Marginal Ice Zone Experiment in the early 1980s, Coordinated Eastern Arctic Research Experiment in the late 1980s, and the Labrador Sea Ice Margin Experiment of the late 1980s demonstrated that a given ice type is characterized by a general signature that dominates the microwave signal. However the signature is actually the sum of emission contributions from features such as ridges, hummocks, melt ponds, snow, snow-ice

interface, brine pockets, relic snow and ice from previous melt episodes. The state of these parameters is controlled by processes to which a floe has been subjected (Eppler *et al.*, 1994). Passive microwave sensors lack the spatial resolution to adequately resolve detail in the ice cover (Lythe *et al.*, 1999). Because SSM/I uses a wide swath of 1394 km and has a coarse resolution of 13 to 70 km it has been limited to applications in the open offshore shelf and oceanic environments.

Visible and infrared imagery from the Advanced Very High Resolution Radiometer (AVHRR) has also been used with some success to distinguish sea ice from open water and clouds (Zibordi and Van Woert, 1993). It is the most widely used spaceborne sensor for sea ice monitoring, due to the free access to data (Sandven *et al.*, 1998). Researchers have been able to map fast ice, leads, and ice concentration of nilas, to thin first-year ice based on tone and texture (Zibordi and Van Woret, 1993; Lythe *et al.*, 1999). Despite its utility in mapping large sea ice features, the low resolution (1.1 km) is limited in the mapping of coastal ice. The optical sensors are also limited by weather conditions, where cloud cover obscures any information about surface ice conditions from these sensors.

Table 2.1 Spaceborne ice monitoring satellites.

	Satellite/Sensor	Start	Comment
Visible and Infrared	NOAA AVHRR	1978	Most extensively used satellite data in ice monitoring. Useful during cloud free conditions.
Active Microwave	ERS SAR	1991	The first satellites to provide extensive SAR coverage in 100km swath, used for operational ice monitoring.
	RADARSAT-1	1996	Regional scale useful for mapping smaller areas. SAR is the most important spaceborne sensor for ice observations because it provides more ice information than any other instrument
Passive Microwave	DMSP SSM/I	1987	Mainly used for climatology studies, because of its low spatial resolution.

Table 2.2 Spaceborne ice monitoring satellite imaging characteristics.

Satellite	Sensor	Channels	Resolution (km)	Swath (km)
DMPS	SSM/I	4 19,22,37,85 GHz	30	1400
NOAA	AVHRR	5 0.58-12.4μm	1.1	2600
ERS	SAR	1 5.3 GHz	0.1	100
RADARSAT	SAR	1 5.3GHz	<= 0.1	50-500

Addressing some of the limitations of optical and passive microwave sensors, ice researchers have used a different form of remote sensing, an approach that could operate independent of daylight and provide suitable information during all weather conditions. Microwave sensors, which operate at wavelengths between 1 cm and 10 m, have this ability. The considerable advantage over optical sensors is that these sensors can “see” through cloud and fog.

2.3 Active microwave remote sensing of sea ice.

Active remote sensors that operate in the microwave portion of the electromagnetic spectrum provide their own source of illumination. More recently synthetic aperture radar data from ERS, JERS, Envisat, and Radarsat satellites, have provided scientists with cloud free, high resolution digital images of sea ice (Lythe *et al.*, 1999). Active microwave instruments measure the amount of backscattered microwave radiation, which is incident upon the ice surface.

Backscattered radiation may consist of two forms, surface scattering and volume scattering (Kwok *et al.*, 1998). Surface scattering results from the incident radiation reflected from the surface of the target of interest, volume scattering occurs when the incident radiation is able to penetrate the target before being scattered. For sea ice, the backscattering can be attributed to differences in surface roughness and the dielectric constants of the ice surface, both of which change with the age of the ice (Melling, 1998). “The bulk dielectric properties of ice are a function of the distribution of brine, air, and solid salt contained within the ice. The differences in distribution of these parameters are directly related to the type of ice. As ice ages, it becomes less saline due to brine drainage, and the ice surface itself becomes rougher, both of which increases the magnitude of the backscatter received at the satellite” (Onstott, 1992).

Onstott (1992) states a first-year ice surface may be smooth or rough depending upon the condition under which it is formed. Importantly, the high brine content of the

first-year ice prevents penetration of electromagnetic radiation, and hence the dominant backscatter mechanism associated is surface scattering. Thus Melling (1998) states “the primary mechanism for backscattering intensity differences is the result of variation in surface roughness, with the dielectric property playing a less important role”

The modified Rayleigh criteria is used to quantify smoothness and roughness to radar (Sabins, 1997). This set of equations discriminates three classes of “roughness” to a specific sensor: rough, smooth, and intermediate. The discrimination is based on the wavelength (λ), and the angle of the incident radiation (θ) and the (RMS) variation in the height (h) of the target surface as:

$$h(\text{Rough}) > (\lambda/4.4) / \cos\theta \quad 2.1$$

$$h(\text{Smooth}) < (\lambda/25) / \cos\theta \quad 2.2$$

For example RADARSAT Fine 3, which is a C-band radar with incident angles between 41° and 44° , the criterion relates to the following ranges of RMS height variation (Figure 2.2).

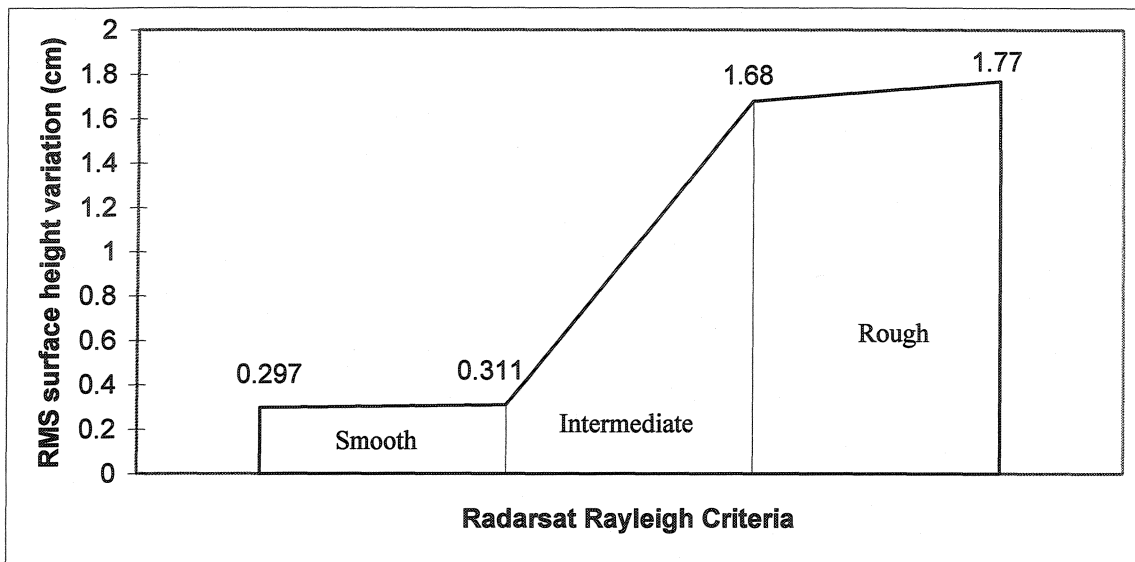


Figure 2.2 Modified Rayleigh Criterion of RADARSAT Fine 3

Smooth surfaces behave as specular reflectors and scatter little of the incident radiation back to the sensor, therefore producing low intensity. Ice types classified as smooth would be open water and standing water in the form of puddles or flooded ice. However this would be dependent on the wind patterns at the time of acquisition, Kwok *et al.* (1992) and Gill and Valeur (1999) identified similar backscatter signatures between first-year ice and wind-roughened water. On the other hand, rough surfaces produce diffuse reflectance with some backscatter of the incident radiation to the sensor. Snow covered ice saturated with water would produce a diffuse reflectance and appear brighter in the resultant image than the ice classes with further stages of melt and differing amounts of standing water (Melling, 1998; Onstott, 1992; Gill and Valeur, 1999).

Vertical structures on the surface may cause corner reflection which increases the radar backscatter. Corner reflectors are formed when two smooth surfaces intersect, this structure backscatters the incident radiation directly back to the sensor producing high returns and very bright spots in the imagery. Brash ice can exhibit this behavior. The fragmented nature of this ice type can produce a series of corner reflectors thus resulting in very bright returns in the resultant image.

The research to date with SAR ice detection has been driven by interest in ice navigation and the role of sea ice in global climatic change (Melling, 1998). It has therefore been limited to general classification of first-year, multi-year ice and open water. Recent work by Simila *et al.*, (1992), Sun *et al.*, (1992), Kwok *et al.*, (1992), Leshkevich *et al.*, (1995), and Smith *et al.*, (1996) have demonstrated the ability of SAR to detect these ice types.

2.4 SAR speckle reduction

It is standard practice that when using radar imagery for classification, efforts are made to reduce the speckle contained in an image before any further image processing is completed. Several approaches have been explored to reduce speckle in radar images, including averaging neighboring pixels, spatial filters, multi-look procedures and more recently wavelet analysis for speckle reduction (Gagnon, 1999).

Speckle on SAR images is caused by coherent interference of backscattered radiation, that is backscatter radiation within a resolution cell having similar amplitude, direction and phase from the multiple scattering elements within a ground resolution cell. The resultant interference is random in nature over the entire image (Dong *et al.*, 1998). Speckle reduction techniques have been developed to improve the presentation of the information content of a SAR image. During image formation several statistically independent looks of the same scene can be averaged to reduce speckle, however this causes a reduction in the spatial resolution of the corrected image. This approach is currently used on present day systems such as ERS-1 and RADARSAT, which use multiple look perspectives to reduce the presence of image speckle (Martin and Turner, 1993).

Adaptive spatial filtering of SAR images proposes to increase the information content of individual pixels through the assessment of the statistical content of an ensemble of pixel values in a given location. In this way, the granular variability introduced by speckle may be reduced by local pixel relationships (Martin and Turner, 1993). The most common spatial speckle filters are the Frost, Lee, and Kuan filters, which are adaptive filters based on the local statistics computed in a fixed square window (Lopes *et al.*, 1993). These filters are known as adaptive filters in that they adapt to the amount of local variation in backscatter in a SAR image. Adaptive filters can smooth speckle in homogeneous areas while preserving high frequency information in heterogeneous areas (Shi and Fung, 1994). Gagnon (1999) indicates that investigations

into the evaluation of existing speckle filters state the need for preservation of the mean, reduction of standard deviation, preservation of edges, and preservation of intrinsic texture as measures of a good speckle reduction filter. Existing speckle filters can effectively reduce the speckle level, however these algorithms also, to some degree, smear edges and blur images. Dong *et al.* (1998) states that smoothing uniform areas while preserving and or enhancing edges is difficult to accomplish.

Donoho (1995), presents wavelet analysis as a means of speckle reduction to overcome some of the problems of traditional spatial filters. A wavelet transform is a recursive decomposition of an original image by means of a mother wavelet, into subsequent quarter area results. The resultant images are independently filtered to remove the noise in the original image.

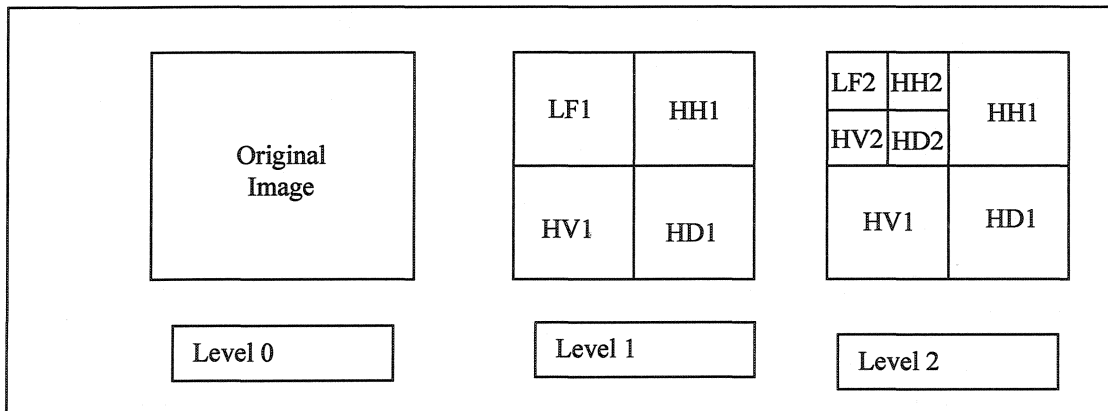


Figure 2.3 Graphic representation of level 2 wavelet decomposition

Figure 2.3 illustrates the decomposition of an image of resolution R during a wavelet transform. The first level of the transform (from Level 0 to Level 1) generates a resultant image consisting of 4 quarter area sub images. The LF1, is a context image, which represents the low frequency components of the original image. It is a lower resolution, $2R$, representation of the original image. The three detail images, HD1, HH1, and HV1 correspond to high frequency wavelet coefficients of the high frequency diagonal, horizontal, and vertical components of the original image respectively. These represent high frequency components of the original image. Level two of the decomposition works on the context image generated in the first level of the decomposition. This results in the level two of the decomposition. Including LF2, the new context image at spatial resolution $4R$, with the resultant three detail images HD2, HH2, HV2 as described above. This wavelet transform is continued until a preset lowest resolution is reached (Donoho, 1995).

During speckle suppression, the values of the wavelet coefficients in the detail or high frequency images are subjected to a threshold value to remove the speckle. If the image is corrupted by noise, it will dominate the wavelet coefficients at higher levels of decomposition. The level of the threshold value is proportional to the noise standard deviation (Gagnon, 1999). It in essence puts all coefficients to zero that are above the estimated noise parameter. Since the noise parameter is not known, it must be estimated from the data. Guo *et al.* (1994) uses the detail images of the first level decomposition to estimate the threshold value. The standard deviation of this series equals the noise

variance for the thresholding algorithm. Thus thresholding the noisy wavelet coefficient removes most of the noise while preserving true image detail.

Another factor to take into consideration in applying wavelet analysis for speckle suppression in SAR imagery is choice of wavelet used for the decomposition. In wavelet theory there are a number of different wavelet families such as Daubechies, Coiflets, M-band wavelets, and space varying, each with different lengths and characteristics used to perform decompositions. In terms of speckle, longer wavelets with higher regularity produce a better result. However, if the wavelet filter is too long, details of the image might be smoothed too much. Guo *et al.* (1994), Dong *et al.* (1998) and Gagnon and Smaili (1996) use the Daubechies family of wavelets for SAR image speckle reduction. The Daubechies' wavelet of length 4 was found to achieve a balance between speckle reduction and the improvement in target to clutter contrast, and is also computationally very efficient (Guo *et al.*, 1994).

2.5 Image texture

Image texture is the spatial variability of the tonal values within an image. The large scale, uneven nature of a surface causes variation in pixel backscatter values that is expressed as image texture. Heterogeneous surfaces will produce a large range of backscatter values over an area, and this high degree of variability is expressed as coarse texture. Homogeneous surfaces have low variability and hence, fine image texture (Ulaby *et al.*, 1986). Shokr *et al.*, (1996) states that the visual interpretation of ice by trained

professionals is based on image tone and texture. Therefore, it is natural to extend the texture parameter to automated techniques of ice classification. Soh and Tsatsoulis, (1999) state the classification and separation of sea ice is augmented by the ability to represent sea ice texture. Statistical texture analysis is important in SAR sea ice imagery research since it allows better representation and segmentation of sea ice regions, compared to analysis based on intrinsic grey levels only.

Mathematically, texture can be evaluated through first and second order approaches. Each texture measure attempts to quantify the relationship that a pixel has to its neighboring pixels within a texture window. The window is structured as a square filter of order 3X3, 5X5, 7X7, etc., so that the center pixel may be assigned the value computed by the texture measure algorithm. The size of the texture window is an important consideration when extracting image texture, it must be smaller than the expected area of the features to be identified (Baraldi and Parmiggiani, 1995) in order that a true ice class texture statistic is extracted, and not textural variation caused by different ice types.

2.5.1 First order texture measures

First order texture measures quantify the amount of tonal variation within a texture window in terms of a neighborhood's mean, standard deviation, variance, power to mean ratio (PMR), skewness and kurtosis. A low variance characterizes a homogeneous area while a high variance implies a heterogeneous area. Skriver (1994) suggested that PMR, which is a measure of heterogeneity, could be used to differentiate

between regions of water and ice. Skewness and kurtosis, which measure the asymmetry and the degree of flattening of the distribution respectively, are useful in discriminating sea ice types, such as open water, fast ice, ice concentrations of 40 to 90 percent, and thin ice or ice of low concentration from ERS imagery (Lyden *et al.*, 1984; Gill and Valeur, 1999).

2.5.2 Second Order texture measures

Second order texture measures utilize the spatial information that arises from the statistical relationship between each resolution cell and its neighbors. This relationship is captured in the grey level co-occurrence matrices (GLCM) as introduced by Haralick *et al.* (1973). The GLCM entries are derived from the grey level of pixels located within a predefined window. Each entry in the matrix represents the occurrence of a possible pair of grey levels measured at two pixels, which are separated by a given vector of particular displacement and orientation (Shokr, 1991). By quantifying the distribution patterns of the elements within the GLCM, texture measures are able to provide information about the nature of the tonal variation, rather than just the amount of variation as calculated by the first order texture measures.

Holmes *et al.* (1984) evaluated the capability of two GLCM measures as sea ice classifiers, inertia a measure of local variation, and entropy a measure of the average uncertainty of grey tone occurrence or disorder. They concluded that inertia could be used to characterize first-year and multi-year ice, while entropy could be used to characterize ice regions of rough surfaces.

Shokr (1991) evaluated several second order texture measures, including inertia and entropy, as well as uniformity which measures how uniform the grey tones are in the region. Inverse difference moment is a measure of homogeneity, and maximum probability normally returns high values in areas of homogeneous grey tone. He found that with respect to the different texture measures each was highly correlated with the other, but not with image tone. Also with respect to displacement vectors the ice floes and structure do not normally maintain any given orientation, therefore a directionally invariant or isotropic GLCM is better utilized in ice classification.

Barber *et al.* (1993), Barber (1989), and Barber and Ledrew (1991), while comparing second order texture classifiers for SAR sea ice discrimination, identified energy, entropy, contrast, variance or standard deviation, correlation, and inverse difference moment as texture measures equally useful for discrimination of first-year ice, multi-year ice and open water.

More recently Soh and Tsatsoulis (1999), evaluated ten GLCM based texture measures including, energy (or angular second moment), contrast, correlation, homogeneity, entropy, autocorrelation, dissimilarity, cluster shade, cluster prominence, and maximum probability. The authors concluded that each texture measure is suitable for sea ice classification, with the exception of cluster shade and cluster prominence. Their findings also illustrate the importance of the size of the displacement vector as opposed to its orientation.

Homogeneity, contrast, standard deviation, entropy, angular second moment and correlation texture measures are readily available in image analysis software, and reflect similarities of the measures studied above. Homogeneity returns high values when the image is locally homogenous at the scale of the displacement vector. Contrast and standard deviation are the opposite of homogeneity, where contrast is a measure of the amount of local variation in the image, and standard deviation is calculated for the texture window, and therefore is a level of local variation as well. Entropy and angular second moment are opposing measures of neighborhood order. Entropy, a measure of disorder, is high in non-uniform areas and low in areas of uniformity. Angular second moment is just the opposite, returning high values when the GLCM has few entries of large magnitude and low when all entries are almost equal or when the grey level distribution over the window has a constant or periodic form. Finally, the correlation texture measure is a measure of grey tone linear dependencies in the image (Baraldi and Parmiggiani, 1995).

The application of texture in the classification of ice seems to be a natural one. However, much of the research to date has been directed to open ocean discrimination of multi-year ice types and that of first-year ice and open water (Shokr, 1991; Barber and Ledrew, 1991; Barber *et al.*, 1993; and Soh and Tsatsoulis, 1999). In coastal systems, several different first-year ice types need to be identified and texture parameters have the potential for characterizing first-year ice types.

Previous studies on SAR image analysis (Guindon *et al.*, 1982; Frost *et al.*, 1984; Ulaby *et al.*, 1986) demonstrate the importance of textural information for image classification. This permits better representation and segmentation of sea ice regions as compared to analysis based on intrinsic grey levels only (Soh and Tsatsoulis, 1999). Using derived textural descriptors, Holmes *et al.* (1984) classified one SAR image to new and first-year ice with an overall accuracy of more than 65%. Nystuen and Garcia, (1992) used standard and higher order texture statistics generated from the co-occurrence matrices to classify SAR sea ice data collected during the marginal ice zone experiment; accuracies reported were over 89.5%. Sun *et al.* (1992) used normalized local average and standard deviation as first order texture parameters to classify sea ice images into open water, young ice, level ice, brash ice and ice ridges.

2.6 SAR image classification for sea ice

The primary goal of image classification is to automate the identification of features in an image scene. Classification of sea ice based on SAR imagery is a difficult task and the research community has not been able to present a generally accepted method to classify sea ice in all areas and around all seasons (Eckes and Fritzke, 2001).

“Automated methods of image classification for radar data are based on image scene statistics and may be divided into unsupervised and supervised approaches. Unsupervised sea ice radar image segmentation automatically determines the number of classes and assigns class labels to each pixel” (Soh and Tsatsoulis, 1999). The spectral

clusters are identified and labeled by the analyst as information classes using ancillary data sources or traditional knowledge. Hara *et al.* (1995) and Rajesh *et al.* (2001) used unsupervised techniques to classify SAR data and find clusters corresponding to first-year and multi-year ice. Leshkevich *et al.* (1995), Kwok *et al.* (1992), and Shokr *et al.* (1996) used an unsupervised K-means clustering method in which the user assigns the number of classes to be extracted from the data. Through an iterative approach, the K-means algorithm seeds the number of cluster centers in the multidimensional feature space. Each pixel is assigned to the cluster whose mean vector is closest. After all pixels have been classified in this manner, revised mean vectors for each cluster are computed. The revised means are used as the basis to reclassify the image data. This procedure is repeated until there is no further significant change in the location of class mean vectors between successive iterations. At this point the analyst determines the ice cover of each class from prior knowledge or ground observation data (Soh and Tsatsoulis, 1999).

The supervised approach on the other hand extracts sample spectral signatures from pixels of known ice cover type referred to as training areas. These sample signatures train the classifier in the recognition of areas of similar response in the image, and a classification algorithm is used to classify the entire image and produce a thematic map.

Among all supervised non contextual classification methods such as K-means, K-nearest neighbors, parallelepiped, and maximum likelihood, the latter is considered to be the best in the sense of obtaining optimal recognition rate. However, these approaches

assume a multivariate Gaussian (normal) distribution. "Each class in feature space is to have an n-dimensional (where n is the number of input variables) multivariate Gaussian distribution for the probability estimation in the discriminant function" (Solaiman and Mouchot, 1994).

A problem with the statistical approach is that the data in feature space may not follow the Gaussian model. Further it may be possible that an information class may be represented in multiple places in feature space, exhibiting separate clusters in several locations. This is particularly the case when classes (for example rotten ice and puddle ice) are amalgamated at a higher level in the classification system (for example into ice) (Atkinson and Tatnall, 1997).

The use of artificial neural networks (ANN) classification of remote sensing data has become increasingly accepted. The ANN is modeled on the human brain as a means of processing data. Neurons in the human brain receive inputs from other neurons and produce an output (if the sum of the inputs are above a synapse firing threshold). The output is then passed on to other neurons. ANNs in the simplest sense may be seen as data transformers, where the objective is to associate the element in one set of data with the elements in a second set. When applied to classification, for example, they are concerned with the transformation of data from feature space to class identification (Atkinson and Tatnall, 1997)

The rapid uptake of ANN approaches in remote sensing is due mainly to their advantages relative to conventional classifiers. These include an independence of distribution assumptions, and the ability to handle data acquired at different levels of measurement (Foody and Arora, 1997).

The most commonly used neural network model for image classification in remote sensing is the multi-layer perceptron (MLP) trained by the back-propagation algorithm (Rumelhart *et al.* 1986). The MLP neural network consists of a number of interconnected nodes. Each node is a simple processing element that responds to the weighted inputs it receives from the other nodes. The MLP normally consists of three types of layers. The first layer is the input layer, where the nodes are the input image bands of a multispectral or multivariate data set. The second type of layer is the hidden layer since it does not contain output units. An increase in the number of hidden layers enables the network to learn more complex problems, but the capacity to generalize is reduced (Foody, 1995). The third type of layer is the output layer and this represents the output data (for example, for image classification, the number of nodes in the output layer is equal to the classes in the classification) (Figure 2.4).

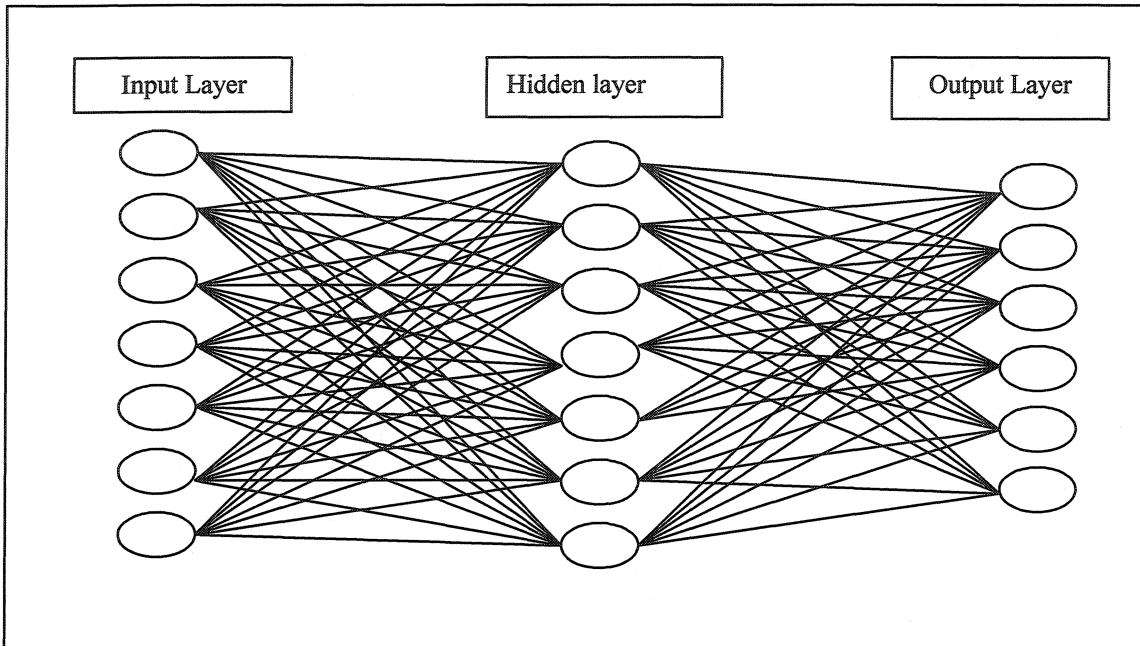


Figure 2.4 Typical MLP neural network

Each node in the network is attached to the nodes in both the preceding and following layers by connections. Connections are associated weights that are trained and manipulated to create the classification. In remote sensing techniques a feed forward and back propagation concept is used to train on the input data to optimize the network for further classification use. In the MLP algorithm, an input pattern is presented to the network from the input layer, and the input signals are passed to the nodes in the next layer in a feed-forward manner. As the signal passes from node to node, it is modified by the weights associated with the connection. The receiving node sums the weighted signals from all input nodes to which it is connected in the preceding layer (Foody and Arora, 1997).

The aim of training a network is to build a model of the data generating process so that the network can generalize and predict output from inputs it has not seen before (Atkinson and Tatnall, 1997). For the MLP, a training pattern is presented to the network and the signals are fed-forward as described above. Then the network output is compared with the desired output (a set of training data of known classes) and the error computed. This error is then back propagated through the network and the weights of the connections are altered to achieve the desired outcome. This process of feed-forward and back propagation is repeated iteratively until the error of the network as a whole is minimized or reaches an acceptable magnitude (Foody and Arora, 1997).

Classification occurs upon completion of the training phase of the network. The multivariate inputs are presented to the network and a resultant classified image is created. Verification of the network can be performed using a data set not seen in the training process. The choice of data for verification should, like the training data be representative of the entire distribution of values associated with a given class. In practice the available validation data is often divided into a training data set and a verification data set to evaluate the performance of the model (Foody, 1995).

Kanellopoulos and Wilkinson (1997) suggest, to ensure that a network learns to classify efficiently, it is important that the input values are scaled to the activation functions range order of magnitude. Failure to perform such normalization can stall learning at an error level that is too high.

Sea ice classification has been reviewed and studied extensively with varying degrees of success. Novel approaches to image processing and classification extend the ability of users to accurately describe ice characteristics from remote sensing data. Much of this work has been limited to navigation purposes and consequently to major ice types of open water, first-year and multi-year types with minimal sub-classification of a major ice type. This research will use the past remote sensing practices on sea ice with new approaches to use radar to classify first-year ice types in a coastal environment.

3.0 Problems and research objectives

The sea ice map user community is diverse, with a number of industries operating in ice affected waters, including commercial shippers, offshore oil exploration and development operators, fisheries, military regulatory agencies, and scientists (Ramsay *et al.*, 1993). The salmonid aquaculture industry in Newfoundland and Labrador is at the point of expansion, it is limited by the availability of suitable coastal sites and requires adequate environmental information to determine it's practical and ecological expansion capacity. One of the main concerns with aquaculture of salmonid species is the damage caused by ice on the fish cages, as well as effects of ice on the fish themselves.

3.1 Problems

The sea ice around Newfoundland and Labrador forms in the Labrador Sea, and the Gulf of St. Lawrence, and drifts south and east with the aid of the Labrador Current. As the ice travels it surrounds and enters the bays and inlets of the Island portion of the province. These ice packs can consist of first-year ice, or multi year ice. In addition, many sheltered bays and inlets freeze during the winter months and form a layer of land fast first-year ice. In spring, the land fast ice melts or breaks under wind and wave action, leaving most areas free of ice by May or early June. It is during the melt and break up of the ice cover that aquaculture infrastructure is at greatest risk.

In order to determine the conditions associated with ice in coastal regions, a means of classifying first-year sea ice during spring melt is needed. The literature has shown that a majority of the research to date has been directed to navigational problems associated with sea ice. Classifications of radar images have been limited in further subdividing first-year ice during spring melt. Most of the researchers have developed unsupervised classification algorithms based on backscatter. These algorithms are only efficient for first-year, multi-year, and open water discrimination. These approaches have difficulty in separating most ice types during the melt season (Ramsay *et al.*, 1993). Texture algorithms, although less efficient, have been shown to complement the backscatter based information in better identifying morphological differences in ice types. (Barber and Ledrew, 1989; Shokr, 1991; Olaussen *et al.*, 1990)

Considering the effects of ice on the aquaculture infrastructure and the fish, the aquaculturalist requires as much information about ice as possible to ensure proper measures are taken to alleviate any undue stress on the fish species, or damage to physical property. Aquaculture sites and potential aquaculture sites are typically located adjacent to the shore and occupy an area of less than one square kilometer. These sites are distributed throughout the areas to ensure adequate physical dispersion, biological structure, oceanographic currents, as well as coastal topography to ensure protection from ice damage. In order to minimize cost and maximize coverage of reliable information, a new methodology for ice reconnaissance is required.

3.2 Research Objectives

The principal objective of this research is:

- To develop a methodology to accurately classify fine beam RADARSAT imagery, identifying the types of first-year ice during the spring melt period.

The secondary objectives are related to computational approaches to image classification, and selection of parameters to facilitate accurate classification. These include:

- To incorporate aerial video for use in spaceborne imagery verification.
- To use texture measures for classification of first-year ice types, assessing the required texture measure parameters and each measure's capability of distinguishing ice types.
- To devise procedures to digitally represent ice type histograms for use in image classification.

4.0 Study area and data

The Bay d'Espoir region of Newfoundland and Labrador provides a suitable study area for the development of coastal ice classification methodology. It was chosen because it exhibits problems associated with the management of an aquaculture industry. This industry utilizes the coastal zone and is concerned with the effects ice have on infrastructure, product, and personnel. This section describes the study area and data used in the research.

4.1 Study area

The study area is located in and around Bay d'Espoir, on the south coast of Newfoundland and Labrador (Figure 4.1). This region is being used extensively for salmonid aquaculture. The Bay d'Espoir region is a complex system of fjords consisting of elongated passages and bays oriented in a general southwest – northeast direction. The bay and channel widths range from 1 to 6 km. The coastal configuration provides shelter for the aquaculture infrastructure from ocean elements like moving ice and extreme wave action.

Several bays presently have aquaculture sites as well as sites used for overwintering for fish pens. Long term maintenance and expansion of the industry requires adequate knowledge of ice conditions. This knowledge will allow selection of new sites as well as the mitigation of problems associated with existing ones.

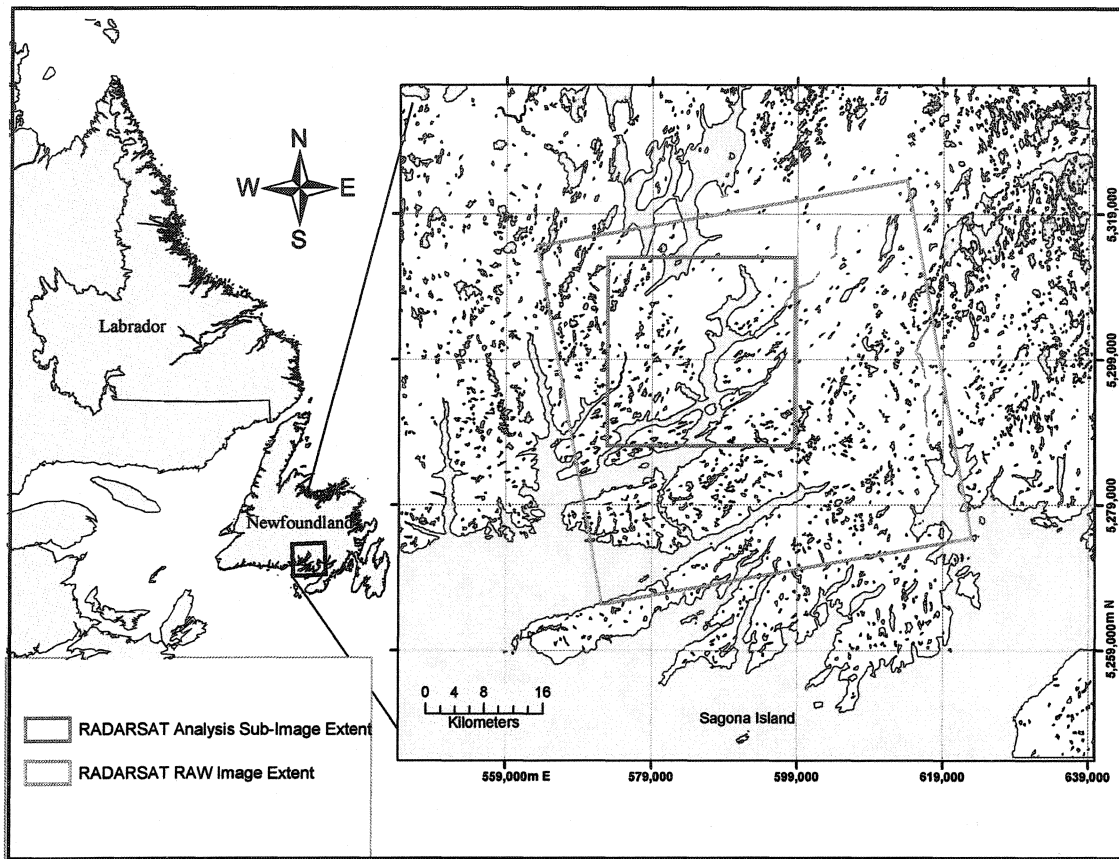


Figure 4.1 Study area with radar image coverage

The study area is located on the south coast of the island portion of the province of Newfoundland and Labrador. This area rarely if ever experiences multi year sea ice, as it lies outside the thirty-year maximum ice limit (Canadian Ice Service, 1997). The yearly ice cover in the region is normally due to local freezing conditions. First-year ice formation reaches its maximum extent in February and usually begins to melt with the area becoming ice free by May or early June of each year (Tlusty *et al.*, 1999).

4.2 Data

The primary data set is a fine beam radar image from RADARSAT-1. Airborne video was used to complement the imagery for use in training and verification of the classification algorithm. Also the digital 1:50,000 vector National Topographic Series (NTS) mapsheets of the study area were used for image geo-referencing.

The RADARSAT-1 SAR system records horizontal like polarized (HH) C-band (5.6 cm) pulses. The image was distributed in CEOS (Common Earth Observation System) a standard format for SAR images worldwide. The image of the Bay d'Espoir study area was acquired on April 15, 1997 six days after the aerial video. Due to the relatively narrow coastal structure and the ice types being classified a fine mode image was selected with an incident angle near the center of the ranges available. Table 4.1 presents the image characteristics.

Table 4.1 Image characteristics

Image Variable	Value
Beam Mode	Fine 3
Incidence angle (°)	41 – 44
Pixel spacing (m)	6.25
Pixels	8247
Lines	7985
Orbit	Ascending
Scene coverage (km)	50 x 50
Imaging format	Single look
Date	97/04/15
Time (UTC)	21:39

The weather conditions during the day of acquisition exhibited a maximum temperature of 2.5°C and a minimum temperature of -1.0°C. Wind conditions during image acquisition varied from 30 – 40 km/h from the WNW, at Sagona Island, 40 km southeast of the study area. The coverage of this scene is outlined on Figure 4.1.

A color aerial video was acquired on April 9, 1997 from a nominal altitude of 1000m. A standard handheld Zenith VHS camera with an 8 power zoom was used onboard a helicopter of the Canadian Coast Guard. Taping was performed through an open cargo door with the camera held by hand. This video was used to extract 640X480 pixel frames for the verification and training sample data. The aerial video acquisition occurred six days before the radar image was acquired. During this period many changes occurred in the ice cover. For example areas that were in advanced stages of melt changed to open water states, while other ice types have progressed further through the melting process.

Four digital 1:50,000 scale NTS vector datasets were used for image geo-registration and base map creation. Each map sheet used the Universal Transverse Mercator (UTM) projection, Zone 21, based on North American Datum 1983 (NAD83). Each digital data set has a horizontal positional accuracy of 12.5m. The map sheets included: 11P/09 Facheux Bay (1985), 11P/16 D'Espoir Brook (1991), 1M/12 Gaultois (1985), and 1M/13, St. Alban's (1985).

5.0 Methodology

This chapter is divided into two sections. The first provides details on the steps involved in processing the training and verification data from the aerial video. The second section presents the approach to image analysis including the application of the neural network training and classification procedure as well as the accuracy of each classified image is assessed.

5.1 Aerial survey

The reference data for the project was collected in a forty minute aerial video of the study area. Visual observations and data processing of this video form the basis of training area and verification data for the image-processing component of the research. Figure 5.1 summarizes the method in a flow chart, beginning with the raw aerial video and proceeding through to the creation of a series of geo-referenced bitmaps of the varying ice classifications found in the study region. The resultant bitmaps were needed for later steps in the radar image processing.

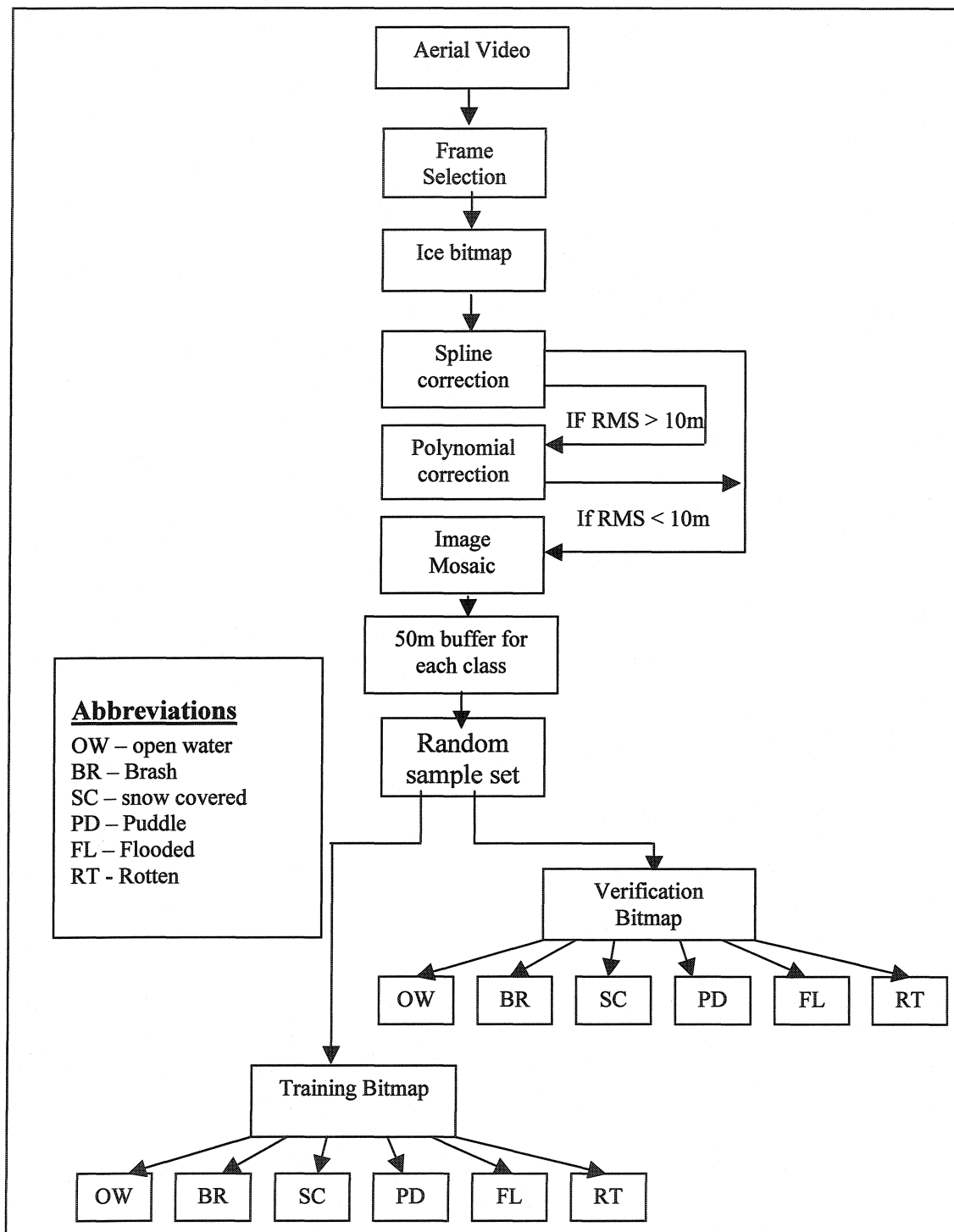


Figure 5.1 Video processing

5.1.1 Video assessment

Upon completion of the aerial survey, the videotape was viewed and frames were selected to represent the ice cover. The flight plan and selection of frames ensured all ice in the study area was captured. At each chosen section of video, the tape was paused and an image “grabbed” with a digital frame grabber. Each frame had a size of 640X480 pixels. The ice types in each frame of the video were then visually identified and assigned to one of the classes listed in Table 5.1. These classes correspond to definitions used in the WMO (1985) sea ice nomenclature. The published photographs from WMO (1985) were used as aids in determining ice type.

Table 5.1 WMO sea-ice nomenclature

WMO Ice Nomenclature	Definition
Puddle	An accumulation on ice of melt-water, mainly due to melting snow, but in the more advanced stages also to the melting ice. Initial stage consists of patches of melted snow.
Thaw Hole	Vertical holes in sea ice formed when surface puddles melt through to the underlying water.
Rotten Ice	Sea ice which has become honeycombed and which is an advanced stage of disintegration.
Flooded Ice	Sea ice which has been flooded by melt-water or river water and is heavily loaded by water or wet snow
Snow Covered	Ice covered with snow
Brash	Accumulations of floating ice made up of fragments not more than 2m across
Open Water	A large area of freely navigable water in which sea ice is present in concentrations less than 1/10. Where there is no sea ice present, even though icebergs are present

These ice classes are recognizable mainly by their tone or relative brightness and color as well as the texture from the color video. Also the presence or absence of features

such as puddles or potholes aided in ice type identification. Interpretation was performed from the video alone with no *insitu* observations of the actual ice.

Each ice type or feature was digitized on the original image frame grab, creating a color-coded bitmap with the same size and orientation of the original frame. The color-coded bitmaps were imported into the frame grab image database for further processing.

5.1.2 Geometric correction of video

Upon completion of the visual interpretation, each frame and its associated classified bitmap were geo-referenced to the UTM coordinate system with a two-step correction process. Given that each video frame was a low oblique image of a section of the study area, a third order polynomial transformation did not give adequate positional RMS for verification. Therefore, a thin plate spline was first used to orient the image in a near nadir view, and second a third order polynomial correction was used to either assess the results of the spline correction or, if necessary, geo-reference the spline result.

The thin plate spline was used since the derived function of the spline has minimal curvature between control points and becomes almost linear at great distances from the control points (Franke, 1985). Since all of these frames were of sea ice with minimal stationary features to aid in correction, an arbitrary grid was used in the initial orientation of the frame.

For the thin plate spline correction, a 10 m arbitrary grid was superimposed over the vector data for display of the visual perspective once the correction is applied. Perspective would show parallel line converging as distance increase and was used as an aid in determining GCP location. A number of ground control points were selected in each frame on the visible coastline. Other GCPs were selected on the artificial grid to force the grid into an acceptable perspective while maintaining adequate coastal registration (Figure 5.2)

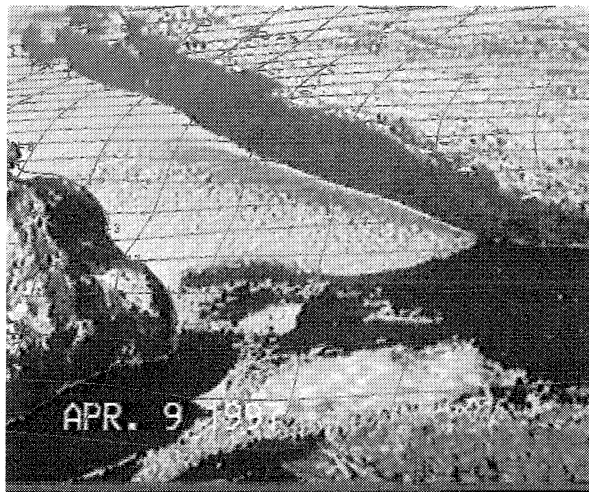


Figure 5.2 Coastline with artificial grid

Performance assessment of the thin plate spline correction was done using the root mean square error (RMS), which measures the deviation between the actual location of the control point, and the estimated location derived from the correction. Since a thin plate spline forces the correction through each control point there is no associated RMS, or means of directly measuring one. Therefore the RMS of each frame was computed using the GCPs of the spline model used in a polynomial model.

Given the data is to be used as verification data for a RADARSAT-1 fine beam mode image with a pixel spacing of 6.5 m and a resolution of 13 m, an acceptable RMS for the ground data was determined to be 10 m. This would ensure the video data exhibited positional accuracy consistent with the radar imagery. If the assessment of the RMS from the spline correction was below 10 m, it was used in the final mosaic. However where the values of the RMS exceed 10 m, a second correction based on a polynomial model was applied to the spline result to reduce the RMS below the 10 m target. Control points for the final correction were located along the coast only, and no artificial GCPs were used. The useable part of the image was located in the lower two thirds of the oblique view data. Distortion in the far range of the frames was too great to be useable for ground data. It should be noted that the vector data used to geo-reference the imagery has a 12.5 m positional accuracy, therefore the calculated RMS can show values below 10 m, but in reality have absolute positional accuracies not better than 12.5m.

The resultant corrections of the individual video frames and their accompanying classified bitmap were mosaicked to form a seamless image and bitmap set of the study area.

5.1.3 Training and verification data extraction

Training and verification data were primarily extracted from the classified aerial video and screened using an unsupervised classification of the speckle filtered radar image.

Training area selection in transition zones between ice classes was avoided by using a 50 m buffer. A fifty meter buffer would ensure the texture windows would not extract statistics on the transition zones, and only train on data within one region of an ice class. The buffer was calculated inside the digitized edge boundary of each ice class polygon so as to exclude training or verification near the transition zones between ice classes. In essence, the training and verification polygons were limited to locations at least 50 m from original polygon edges.

The change in condition between the video imagery and the radar image caused the training area sampled on the video to have heterogeneous brightness and texture characteristics in the radar image. For example, simple visual assessment allowed the identification of locations where sampling for an ice type was distributed over two or three different ice types on the radar brightness image. Brightness values of the radar image were clustered using an unsupervised classification to compensate for this problem. This procedure creates clusters based on tonal similarities in the ice and open water classes. A large number of 40 clusters were used, allowing several distinct clusters to be identified. The buffered bitmaps of the aerial video ice classification were then randomly sampled to produce the other image used in a two map cross tabulation. The six classes of the input bitmap classes and the 40 classes of the unsupervised cluster results.

The results of the cross-tabulation were used to locate and eliminate areas of change. The majority of the study region was open water at the time of image acquisition, as was evident in the size of the clusters that were visually interpreted to be open water. Consequently, the high number of ice classified pixels in the bitmap that fell in the water cluster could be eliminated. Further labeling of valid pixels was based on a visual interpretation of the cross-tabulation image. Inclusion of a pixel in an ice class training set depended upon the pixel previously being classed as that ice type, that is it must be from the original bitmap sample. The procedure was used only to eliminate erroneous pixels from the initial sample set, not to create new training and verification sites.

5.2 Radar image processing

This section describes the stages of the radar image preprocessing and processing. Preprocessing which includes radiometric and geometric correction are described, followed by speckle suppression using wavelet analysis. Next, training data extraction methods using the classed bitmaps from section 5.1 is discussed. Texture parameter selection and signature generation are used to define optimum texture parameters. A novel approach to histogram characterization is presented. Neural network image classification is discussed followed by image accuracy assessment.

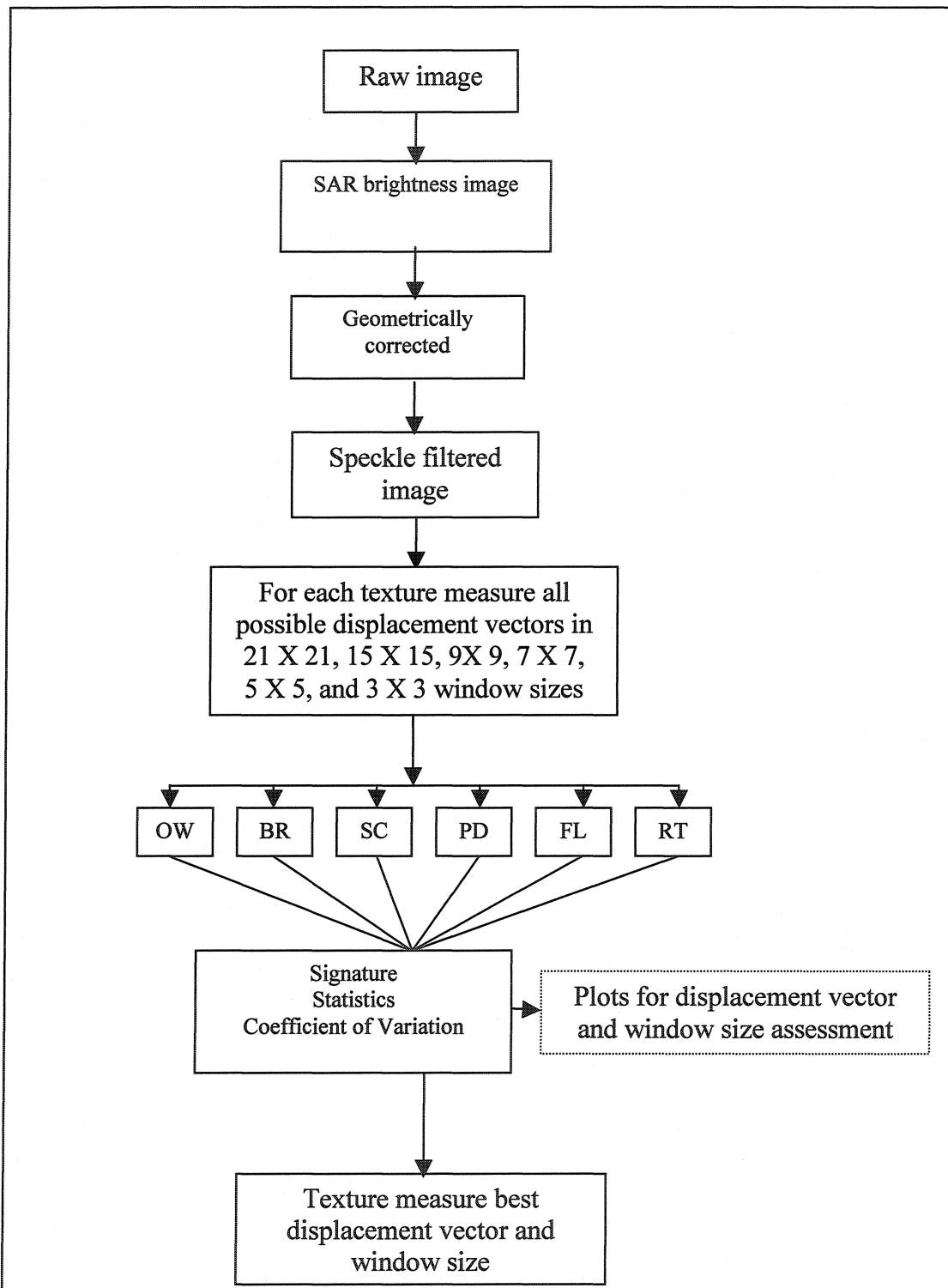


Figure 5.3 Radar, initial processing

5.2.1 Radiometric calibration

Radar brightness (β°) is the radar signal backscattered from the ice surface and recorded by the sensor. Normal CEOS data have visual lookup tables applied to the data to enhance pixel appearance, the data must be calibrated to brightness values in order to extend the research to other radar scenes in an operational methodology. The algorithm to convert the CEOS image format distributed by RADARSAT-1 is given by equation 5.1 (Sheppard, 1998). Values for scaling (A_{2k}) and offset (A_3) are provided in image header files.

$$\beta^\circ_k = 10 \cdot \log_{10} [(DN_k^2 + A_3)/A_{2k}] \quad 5.1$$

where,

- β°_k : radar brightness for pixel (dB)
- DN_k : magnitude of the k^{th} pixel from the start of the range line in the image data
- A_{2k} : scaling gain value for the k^{th} pixel from the start of the range line in the image data
- A_3 : offset

5.2.2 Image geometric correction

The geometric correction is required to transform the raw image to a known coordinate system, and to match the radar image with the video mosaic. The UTM, Zone 21, North American Datum 1983 was used. Geometric correction is achieved by selecting a series of ground control points (GCPs), which are features that can be easily recognized

on both the image and the digital vector map used for the correction. Due to the coastal orientation and abundant lakes throughout the study area the GCPs were selected at land water interfaces on the image and in the vector data.

The GCPs were used to calculate a third order polynomial transformation, which would be used to resample the image. The resultant transformation reports an overall RMS error. Considering a RADARSAT-1 fine beam image has pixel spacing of 6.5 m an acceptable RMS of one half a pixel was sought corresponding to 3.25 m (Jenson, 1996).

The extent of the corrected radar image is outlined in red on Figure 4.1. A nearest neighbor resampling method was selected to ensure no change in pixel values in the resultant image. No change in brightness values ensures classification was based on ice type radar backscatter and not an average of the pixels in the neighborhood as results from other resampling methods.

5.2.3 Speckle reduction

In this study, a “soft thresholding” procedure for speckle reduction was used, as originally defined by Donoho (1995). In order to determine the optimum Daubechies wavelet to use, a series of test were performed.

Six different combinations of wavelet lengths and levels of decomposition were performed on a 1024X1024 pixel sub image in the study area for evaluation. Due to the nature of wavelet decomposition it is a requirement of the algorithms that the images

used for processing exhibit a size of $2^n \times 2^n$, that is 2x2, 4x4, 8x8... 1024x1024, 2048x2048, or 4096x4096 etc.. The wavelet filtering procedure is outlined in Figure 5.4. The first step in the filter process was to use a logarithmic transform of the original image to convert the multiplicative nature of speckle noise to an additive form (Guo *et al.*, 1994). The wavelet decomposition and thresholding procedure were performed on the result. An inverse wavelet decomposition or image reconstitution and finally an inverse logarithm transform results in the speckle reduced brightness value output image.

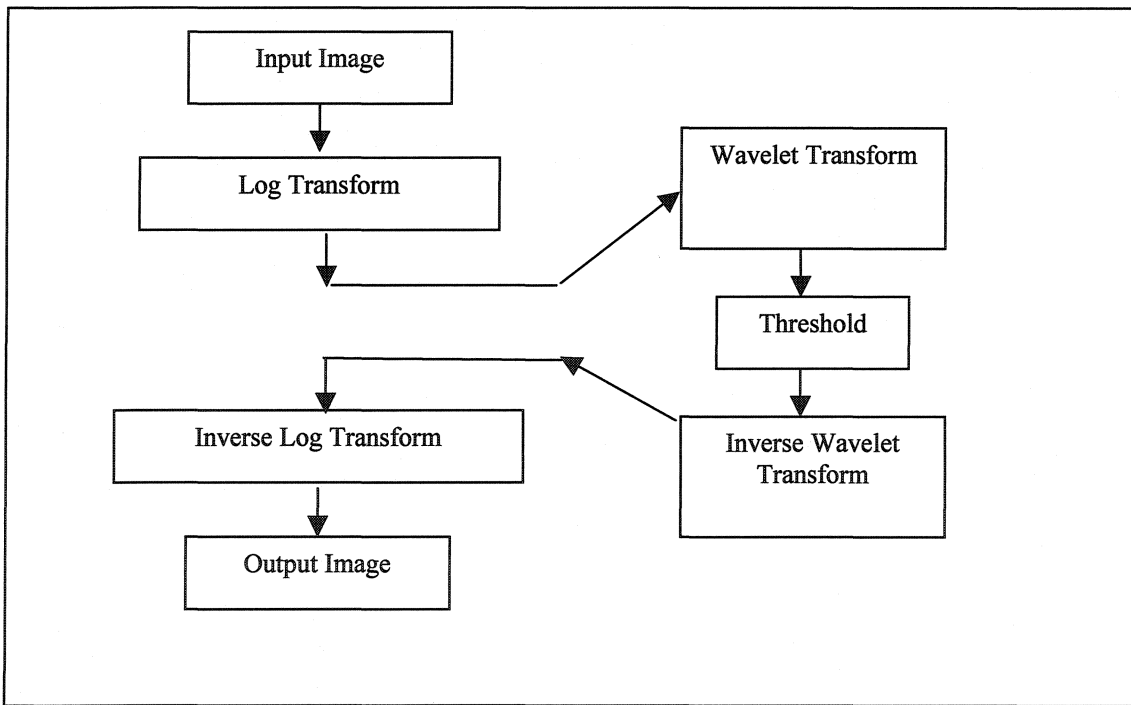


Figure 5.4 Wavelet speckle filter procedure.

Performance assessment of each combination of wavelet and decomposition level, was done using speckle index which is calculated as a measure of the amount of speckle

in an image, and used to examine the success of a speckle filter by comparing its value for different filters.

$$S = \left(\frac{\bar{X}}{SD} \right)^2 \quad 5.2$$

where, S: speckle index

SD: standard deviation of input brightness value.

\bar{X} : mean of brightness value.

A uniform area of backscatter in the test scene, over all combination of wavelets was used for finding the approximate speckle index. The goal is to increase the value of S as much as possible while still preserving the local spatial information in the image. Thus the index must be considered together with the processed image in order to determine how well the filter performs (Gagnon and Smaili, 1998). The optimum wavelet length and level of decomposition was then used to filter the entire image.

5.2.4 Texture analysis

Five texture measures were selected for further investigation, these were based on inclusion of the texture measures in previous work on sea ice classification by Barber *et al.* (1993), Shokr (1991), and Soh and Tsatsoulis (1999). The selection includes, standard deviation (SD), angular second moment (ASM), homogeneity (HOM), entropy (ENT), and correlation (COR).

Each texture measure has a window size, vector orientation and displacement that affect the value of the texture measure. Selection of the optimum window and displacement parameters was based on an exploration of signature statistics derived from each of the individual texture measures. With respect to orientation of the displacement vector it was decided to use direction invariant displacement vectors, since there is no *a priori* knowledge of spatial orientation of the ice features present in the study area (Shokr, 1991).

A systematic approach was used to identify the optimum displacement and filter size for each texture measure. For all five texture measures, filter sizes ($fs \times fs$) of 5 X 5, 7 X 7, 9 X 9, 11 X 11, 15 X 15 and 21 X 21 were tested with displacements ranging from 1 pixel to $fs/2$ pixels. For example for the 21 X 21 filter size vector displacements of 1 to 10 pixels were tested.

The overall objective for selection of filter size and displacement vector is to have the smallest texture window possible, while preserving maximum separability between classes. A smaller texture window allows a smaller discernable area for classification. Displacement vector selection requires a value that allows the filter to identify the spatial arrangement of tonal variation causing the texture (Soh and Tsatsoulis 1999). Signature statistics were developed for the six ice classes over the range of texture measures calculated.

The evaluation of optimum texture parameter was based on coefficient of variation and signature separability using Bhattacharrya distance. The coefficient of variation is a measure of the signatures relative dispersion, a high coefficient of variation indicates a training area that is not homogeneous in its texture measure, and conversely the return of a low value indicates a homogenous training area. The Bhattacharrya distance is a measure of class separation. The goal is to minimize the coefficient of variation while maintaining signature separability between classes.

5.2.5 Histogram characterization

Due to the complex surface characteristics of ice in various stages of melt, the histogram of each ice class exhibits non-normal distributions. Gill and Valeur (1999) explored measures of skewness and kurtosis to characterize the non-normal distributions exhibited by ice types. However in this research a new methodology was developed to address the non-normal signature distributions of the texture measures. The procedure characterizes the histogram through a neighborhood filtering process.

Exploration of the histograms for each ice type with respect to the texture measures, showed that the ice classes have unique histogram shapes. While the approximate shapes of the histograms remained similar, the number of pixels within specific texture ranges (frequencies) showed differences across ice classes. This unique response of each class of ice within specific texture value ranges was used to characterize the histogram. Figure 5.5 indicates the individual histograms for the ASM texture

measure with a displacement vector of $d = 3$. While all histograms cover the same range of values 0 to 2.0, each ice type shows a distinctive difference in histogram shape, mean and standard deviation are similar but the relative frequency of peaks vary in the histogram.

The behavior of a textural measure is dependent upon the beam mode of image selected, with one beam mode capturing a particular texture that another does not. The actual range of values returned by a texture measure is dependent on the dynamic range of the initial image (Ulaby *et al.*, 1986). While this research uses only one RADARSAT-1 image, the methodology can be extended to other imagery. The shape of the textural histograms may change based on the image type, but the methodology of characterization is essentially linked to the optimum bin size.

Characterization of the histograms involves the determination of the optimum bin size. The most important parameter of a histogram is the bin width because it controls the tradeoff between presenting a picture with too much detail or too little detail with respect to the true distribution (Wand, 1997).

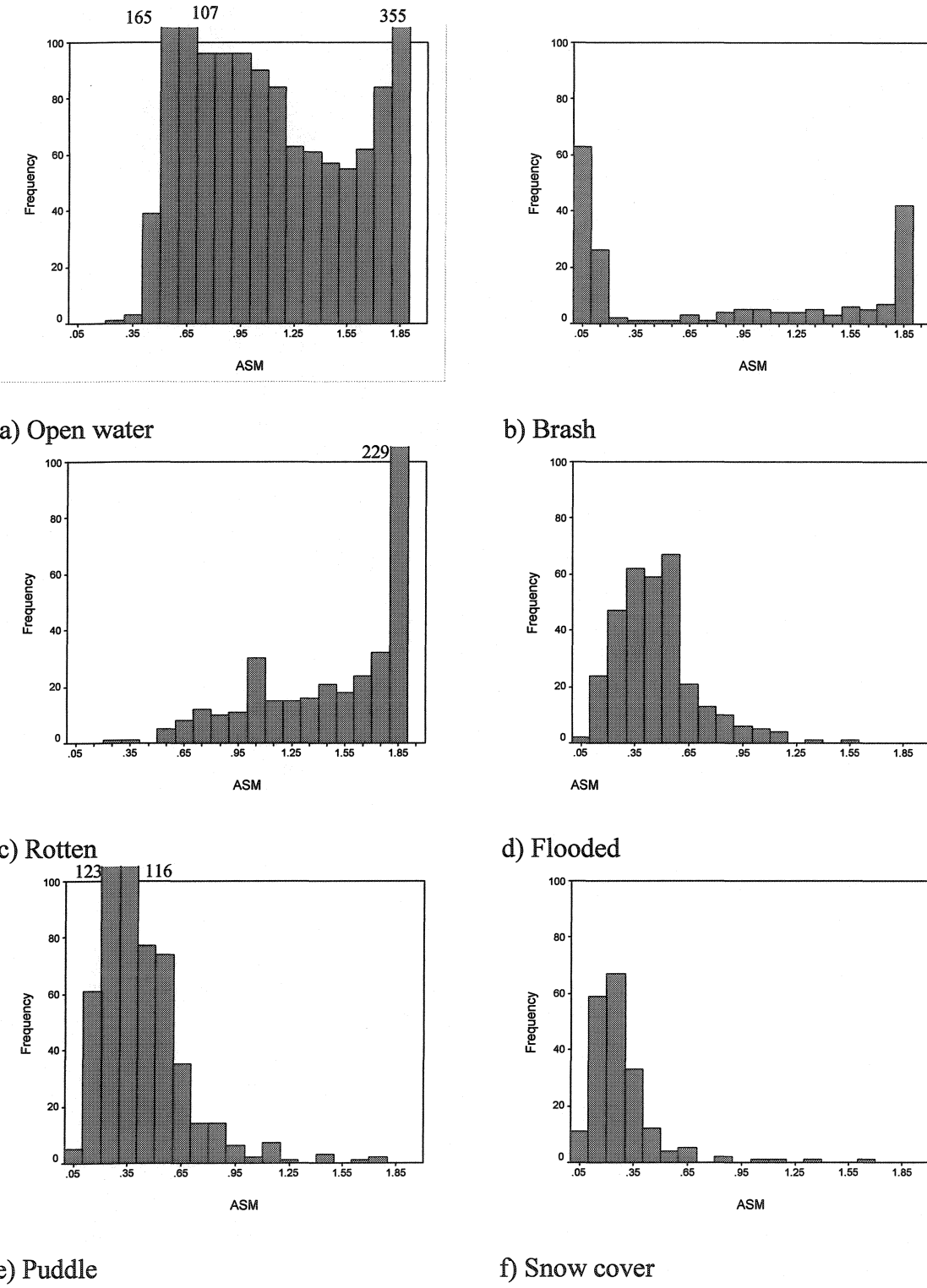


Figure 5.5 Angular second moment texture ($d=3$) histograms of ice types (a – f)

Scott (1979) states an estimate of the best histogram to accurately describe a data set requires an optimum bin size. To achieve this, knowledge of the true underlying density function is needed. However this knowledge is rare, therefore a data based method was derived based on the Gaussian density function. The resulting estimate was also shown to be applicable to non-normal data sets (Scott, 1979). The optimum bin size for a given distribution is calculated by equation 5.4.

$$h_n = 3.49sn^{\frac{-1}{3}} \quad 5.4$$

where,
 h_n : bin size
 s : estimate of the standard deviation
 n : population size

Extension of the histogram representation to a classification approach required the creation of individual images that represented the number of pixels in each histogram bin of the texture measure. That is, if a distribution required 10 bins to represent that histogram, then 10 images representing each histogram bin would have to be created. Figure 5.6 illustrates a characteristic histogram bin image, for ASM bin level 0.24 to 0.46. The highest value of one indicates that all pixels in the defined neighborhood have a value that fall in that histogram bin, which is between 0.24 and 0.46. Conversely a value of zero indicates that no pixels within the neighborhood have texture values that fall in the histogram bin.

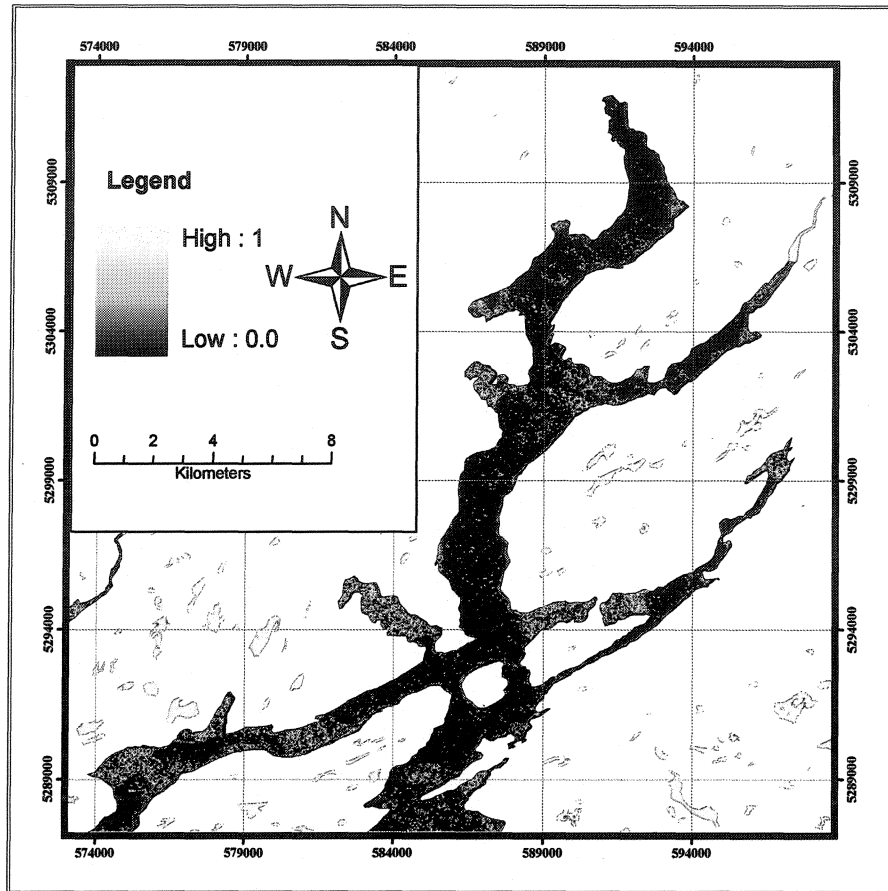


Figure 5.6 ASM $d=3$ histogram bin image (0.24 to 0.46)

A bin image is created based on an average filter with a size equal to that of the texture measures. Each texture image was first re-classed to values of one (1) when the pixel value was within the specified bin width, and zero (0) where the pixel value was not. The resultant Boolean image represented areas within the original texture image where values satisfy the histogram bin of interest. This Boolean image was then used to calculate frequencies of bin values based on an average filter. The filter returned a value ranging between 0 and 1 depending upon the frequency of ones (1s) within the filter window. A value of 1 represents all pixels within the filter window are within the

histogram bin of interest, a value of zero represents no pixels within the filter window have values in the range of the histogram bin of interest. This window in essence normalizes the histograms for each ice class to allow discrimination.

The result of the characterizing procedure recreates an ice class textural histogram distribution based on signature statistics over the calculated bin images and the texture window. While histogram shapes are similar the normalized frequencies of the peaks are different, with each bin image capturing the corresponding ice class peak differences.

5.3 Neural network classification

Traditional classification approaches based on Gaussian distributions are not ideal for the texture images due to the non-normal characteristics of the image statistics. In addition to being applicable to non-normal distributions, the artificial neural network has advantages relative to conventional classifiers. These advantages include, the ability to handle data acquired at different levels of measurement precision and noise, which is the case of radar backscatter and image texture calculations (Foody and Arora, 1997).

A multi-layer perceptron (MLP) neural network trained by the back-propagation algorithm (Kanellopoulos and Wilkinson, 1997) was implemented for each texture measure. In this study these were processed independently of one another to compare each texture measures capabilities in the discrimination of the fist-year ice subdivisions.

The next three sections describe the neural network architecture, training process and application of the classifier for each texture measure.

5.3.1 Neural network architecture

The MLP was a three-layer model consisting of an input layer, a hidden layer, and corresponding output layer. The input layer consisted of a mean filtered brightness value image to add tonal variation to the classification procedure, as well as the calculated histogram bin images of the texture. The number of input nodes varied for each texture measure approach depending on the number of bin images needed to characterize the histogram for that texture measure. The output layer corresponded to the six classes of ice identified in the study area. The general architecture of each network is similar to the one presented in Figure 2.4. A single hidden layer was selected to allow for efficient training and to allow the network to generalize the data (Foody and Arora, 1997).

Each node in the architecture is connected; with each connection is an associated weight. It is through training the network that these weights are assigned. The input to a node j in such a network is the weighted sum of the output from the layers below, given by equation 5.6 (Kanellopoulos and Wilkinson, 1997).

$$net_j = \sum_i w_{ji} o_i \quad 5.6$$

where,

- net_j : connection weight
- o_i : output, node i
- w_{ij} : weight between output node i and input node j

This weighted sum is then transformed by the nodes' sigmoid activation function; to produce the node output calculated by equation 5.7:

$$o_j = \frac{1}{1 + \exp(-net_j + \theta_j)} \quad 5.7$$

where,

o_j : node output
 θ_j : constant.

When the signal reaches the output layer it forms the network output. In traditional hard classifiers, pixels are assigned to a single class only, the output of a node is set to one if its inputs outweigh that of the other output node, while all other nodes in the output layer are set to zero (Kanellopoulos and Wilkinson, 1997).

5.3.2 Training the neural network

Training a neural network requires the estimation of each of the weights in the network mentioned above. The back-propagation algorithm for estimation of weights aims to minimize a differentiable error function of the network outputs calculated over a set of training samples (Kanellopoulos and Wilkinson, 1997). The bitmaps created from the training and verification data extraction (section 5.1.3), were used as both training and verification datasets. The resultant bitmaps were separated using a random sample, whereby 50 percent of the data was used for training the neural network while the other 50 percent was used for error assessment.

During the training process, the network initially has arbitrary weights assigned. The training data is presented to the network and signals are fed through the network,

with a resultant output. The network output is then compared with the desired output as dictated by the training data. The error is then computed and back propagated through the network. The weights of the connections are then altered accordingly to what is known as the generalized delta rule, as defined by equation 5.8 (Atkinson and Tatnall, 1997).

$$\Delta w_{ji}(n+1) = \eta(\delta_j o_i) + \alpha \Delta w_{ji}(n) \quad 5.8$$

where: δ_j :index of the rate of change of the error
 η :learning rate parameter
 α :momentum parameter.

This process of feeding forward signals and back propagating the errors is repeated iteratively until the error of the network as a whole is minimized. It is through the successive modification of the adaptive weights that the neural network is able to learn (Atkinson and Tatnall, 1997).

5.3.3 Applying the classifier

Upon completion of the iterative training process, the neural network is prepared for image classification given that the weights of each connection have been assigned. In the classification process, inputs in the form of image layers are exposed to the network. Through the weights and connections, each successive pixel in the input data set is classified. The output result is a classified image with one of the six ice classes assigned to each pixel.

5.4 Classification accuracy assessment

The accuracy of each texture approach is assessed with the verification data from the extraction process of section 5.1.3 used to create an error matrix. The error reported through the back propagation process of network training is also assessed.

The error matrix is a standard form for reporting classification accuracies (Congalton, 1991). The matrix identifies not only the overall accuracy and error for each ice class, but also the level of misclassification or confusion between classes. Class commission and omission errors are investigated, together with producer's, user's and overall accuracy statistics. Producer's, user's, and overall accuracies of the classification can be calculated from the confusion matrix. The producer's accuracy is the percent probability that a pixel from the validation data has been classified correctly. The user's accuracy is the percent probability a classified image pixel is actually that class on the ground.

Errors of omission occur when pixels are not included in classes they should be and the commission errors occur when pixels are included in a class they should not be. For example, considering the category flooded ice on the classified radar image, an error of omission could result from an actual area of flooded ice being classified as water and the commission error would be to have areas of open water to be wrongly included in the flooded ice category.

Operational requirement would prefer the user's accuracy as a measure of classification accuracy between classes, since knowledge of what is in the study area is the goal. Overall accuracy can provide an estimate of image accuracy; however, it may also conceal significant variability in the accuracy of classification between classes (Congalton, 1991).

Finally the Kappa statistic is also evaluated. The Kappa statistic is a measure of the difference between the actual agreement between the reference data and an automated classifier and chance agreement between the reference data and a random classifier. Kappa ranges between zero and one, where true agreement equals one and chance agreement equals zero. A value of 0.45 % indicates that the classifier is 45 % better than the chance classifier or random assignment of pixels. Kappa agreement values less than 0.4 are poor, 0.4 to 0.75 are good and greater than 0.75 are excellent (Rosenfield and Fitzpatrick-Lins, 1986).

6.0 Results

The results are presented in two major sections. The first section describes the aerial survey, with training and validation data extraction. The second section shows the results of the SAR image analysis.

6.1 Aerial survey

The initial observation of the aerial video produced nineteen frames spanning the extent of ice present in the study area. Visual observation of the reconnaissance video identified five ice types, plus open water. Figure 6.1 represents an example of an original frame and the resultant classified bitmap in its original geometric orientation.

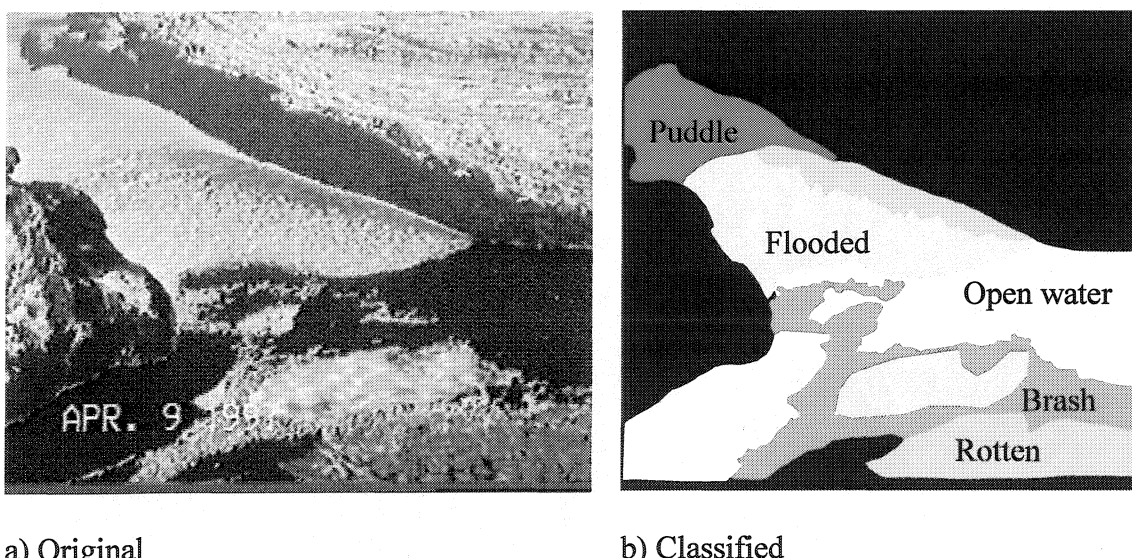


Figure 6.1 Original (a) and classified (b) Lampedois video frame.

Table 6.1 shows the five ice types located in the study area, with visual descriptions of each ice type with respect to tone and texture. The relative percent coverage of each ice class as derived from the aerial video interpretation is also presented. Over 50% of the area is classified as either puddle or flooded ice. There is very little remaining snow covered ice indicating the advanced stage of the melting season. One fifth of the classified area is brash and rotten combined; further evidence the area is in the advanced stages of melt. Approximately one quarter of the classified area is open water, however not all open water was covered in the video, therefore the estimation is lower than in reality.

Table 6.1 Aerial video ice description

Ice Class	Tone	Texture	Comments	Area Classified (%)
Snow covered	1	1	Consolidated ice	8
Puddle	2	2	Snow cover left in piles	32
Flooded	3	3	Water saturated, few thaw holes	29
Rotten	4-5	4	Abundant thaw holes	7
Brash	1-5	4	Fragments of floating ice	15
Open water	5	1	Less than 1/10 sea ice	22
Tone: 1. bright to 5. dark			Texture: 1. fine to 4 coarse	

6.1.2 Video geometric correction

The initial step in the geometric correction of the video imagery was the thin plate spline. The accuracy assessment of the thin plate spline was completed by entering the GCPs into a third order polynomial to calculate the RMS, as displayed in Table 6.2. Four of the nineteen spline corrected frames had overall RMS errors lower than 10m, which

are tolerated to match the resolution of the SAR image after the first stage of the correction. Where X or Y RMS did not meet acceptable levels, a second geometric correction was applied using a third order polynomial model with new ground control points.

Table 6.2 Geometric correction results for video frames

Frame	Spline correction		Polynomial correction	
	X RMS (m)	Y RMS (m)	X RMS (m)	Y RMS (m)
Arran 1	14.09	9.92	9.90	2.82
Arran 2	19.2	6.05	8.39	2.61
Conne1	12.5	5.65	8.40	5.75
Conne 2	25.8	5.38	7.06	7.92
French	15.7	3.05	5.01	2.92
Hardy	24.49	21.40	9.36	9.76
Lampedois 1	11.42	7.55	7.54	5.21
Lampedois 2	9.79	8.66	N/A	N/A
Lampedois 3	16.3	9.4	5.05	6.19
Little River 1	34.54	8.01	5.57	6.96
Little River 2	9.77	7.63	N/A	N/A
Muddy	21.71	14.43	7.81	6.02
Pomely	14.07	4.95	5.05	7.08
Riches	37.14	15.75	9.98	9.27
Roti 1	21.50	11.32	8.92	8.74
Roti 2	15.5	11.1	2.99	9.83
Roti 3	17.9	14.2	9.16	9.81
St. Joseph	9.05	7.57	N/A	N/A
Swanger	5.62	3.69	N/A	N/A

The resultant 19 frame bitmaps were geo-corrected and mosaicked to form a seamless data set for the study area as illustrated in Figure 6.2.

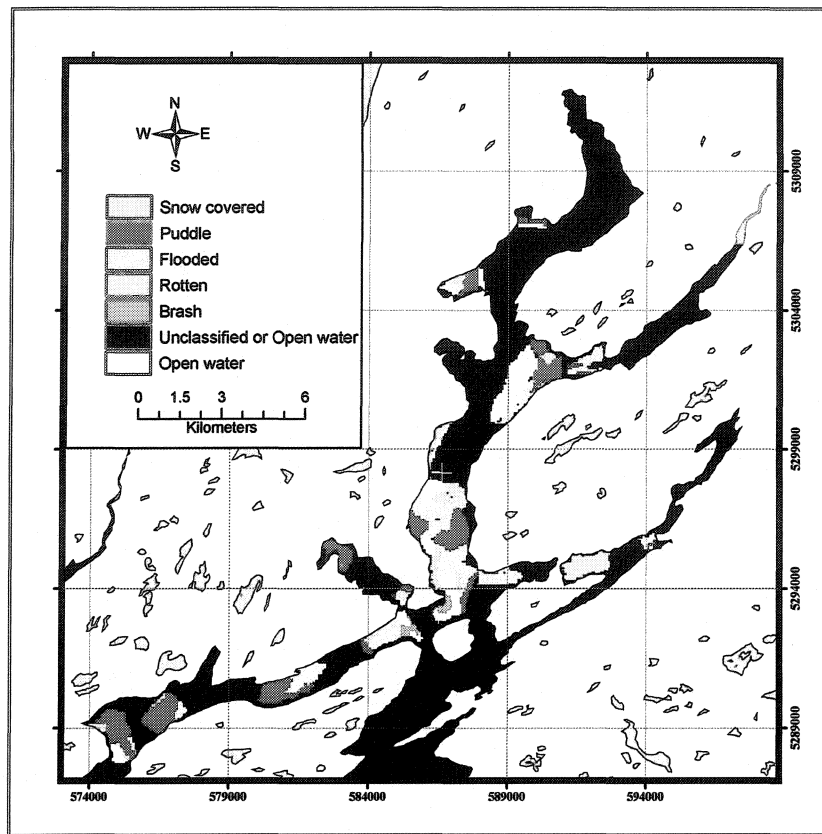


Figure 6.2 Classified aerial video bitmap mosaic

6.1.3 Training and verification data extraction

The cross tabulation procedure employed to identify homogeneous training data produced the following. Visual inspection of the clustered image was first performed to identify the major clusters of ice, open water and land. It was noted that the largest cluster was attributed to land, corresponding to cluster six in Table 6.3. The water clusters were identified using areas that were 100 % open water on the aerial video acquisition; considering that the temperature during the six day period was consistently above zero no new ice formation was expected. Based on this premise, open water on

April 9 would be open water on April 15 unless wind moved brash ice into a region.

Cluster one and cluster three were identified to be open water.

Land and open water were the largest clusters and consequently resulted in the majority of erroneous pixels being eliminated from the training and validation sites. Further study of the coincidence of the remaining original training pixels with the other clusters helped label these clusters. The highest occurrences across all classes occurred in clusters four and five. Unfortunately observation of the coincidence patterns could not allow the accurate labeling of those clusters, and therefore they were omitted. Their composition, however, closely resembled that of open water.

Table 6.3 Cross-tabulation results of training data and radar cluster analysis

CLUSTER	SC	BR	RT	OW	FL	PD	Total	Class Assigned
1	36	119	376	1003	1741	932	4207	Open water
2	128	81	901	1403	3547	2180	8240	Rotten
3	268	71	830	3054	3589	2860	10672	Open water
4	476	44	475	2884	2614	3321	9814	none
5	715	9	221	1889	1689	3388	6390	none
6	851	2	100	990	1497	2967	6407	Land
7	662	0	56	323	655	1921	3617	Flooded
8	441	0	20	67	343	1077	1948	Puddle
9	236	0	5	24	180	504	949	Snow covered
10	107	0	1	8	71	228	415	Snow covered
11	38	0	0	5	26	69	138	Snow covered
12 to 39	0 to 24	0	0	0 to 5	0 to 8	1 to 16	135	none
Total	4016	331	2985	11690	15969	19469	52932	

Cluster two exhibited similar tonal characteristics as the open water clusters, however study of the spatial location of these clusters with respect to the other ice classes resulted in its identification. The clusters were typically located in or near the transition zones between the open water and the consolidated ice pack. Considering the transition of ice from snow covered ice through to open water, rotten ice should occur in this location.

Identification of the other ice types came in succession after the above labeling was completed. Since flooded ice contains large amounts of surface water it was expected to have similar tonal characteristics to open water. Cluster seven exhibited the closest tonal characteristics to open water. Observation of the coincidence of puddle pixels show that in cluster seven it has the second highest value, exceeded by flooded only.

Cluster eight corresponded to puddle, matching over 50% of the pixels falling in its cluster. Clusters nine, ten and eleven occurred in the areas of snow covered ice from the aerial video. As well, the proportion of pixels that fall in these clusters is higher for snow cover than for the preceding clusters. These clusters were consequently labeled snow cover. Three clusters were used for this class to ensure sufficient numbers of training and verification pixels at the end of the process. The remaining clusters 12 to 39 were not used due to the small number of pixels matching any class of interest.

The cluster analysis was useful for screening the training data for five of the six ice classes. The dynamic nature of brash ice results in no consistent match between the brash training areas and a homogeneous image cluster. Brash is defined as an accumulation of floating ice made of fragments not more than two meters across. Due to its physical make up, brash ice is in constant motion until it hits a barrier, such as a coastline or a consolidated ice pack. Considering the 20-40 km/h WNW winds in the 12 hours preceding image acquisition, new training areas for brash ice were defined. Based on the above clusters the transition zone between open water and a consolidated ice pack or land mass was identified. These areas were located on southerly or southeasterly shores where onshore winds would have been evident during the 12 hours preceding image acquisition. If there was any brash in the study area it is in this location that it should be located. Several training sites were digitized in these transition zones and randomly sampled, for the brash training and verification data set.

Table 6.4 lists the number of sampled pixels for each of the five ice classes and open water. Each set of pixels were sampled and divided half and half for training and verification.

Table 6.4 Sample size for each ice class

Ice Class	Number of sampled pixels	Percent
Snow Cover	381	6
Puddle	1077	17
Flooded	655	10
Rotten	901	14
Brash	358	6
Open Water	3054	48

6.2 Radar image processing

This section presents the radar image analysis. The accuracy of the geometric correction is presented. The results of the wavelet analysis investigation for speckle suppression are presented with the parameters used to filter the image. Summaries of the signature development and texture analysis followed by the characteristics of the ice class histograms are presented with the resulting histogram bin image characteristics. Finally the neural network training is shown with the resulting imagery assessed for accuracy.

6.2.1 Geometric correction

The geometric correction was based on 28 ground control points (GCPs), their distribution is shown on Figure 6.3 as red crosses, the blue crosses represent GCP's with high individual RMS error. The GCPs are clustered on the coastline, with sparse distribution in the northwest portion of the study area. However the transformation exhibits control in the coastal regions. The polynomial transformation produced a RMS of 1.53m in the X direction and 1.25m in the Y direction. A nearest neighbor resampling method was selected to ensure no change in pixel values in the resultant image. The corrected image area indicated by the yellow line was 4096 pixels by 4096 lines with a 6.25m pixel spacing corresponding to that of the raw SAR image.

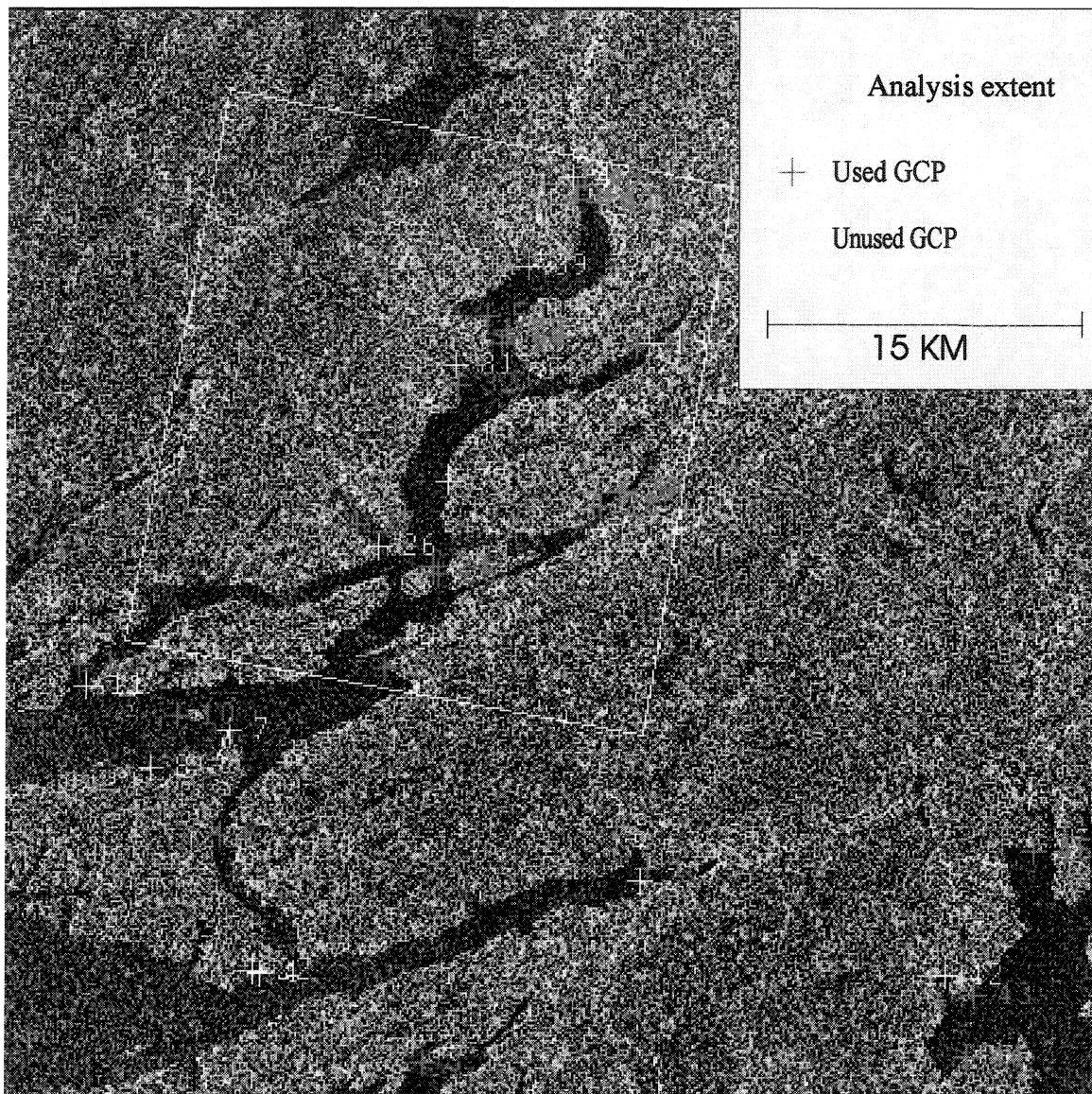


Figure 6.3 GCP selection and study area

6.2.2 Speckle filtering

In the analysis of wavelets for the reduction of speckle in the radar image, six combinations of level of decomposition (dc) and wavelet base were used to assess which parameters best suited speckle reduction for this application. The study was performed

on a 1024 X 1024 pixel sub-image centered at 2100 pixel, 3000 line illustrated by the red line in Figure 6.4. Table 6.5 presents the results.

Table 6.5 Wavelet parameters

Wavelet Base	dc	Mean	Standard deviation	Speckle Index (S)
Daubechies 1	2	2363.4	743.1	10.10
Daubechies 1	3	2363.3	671	12.41
Daubechies 4	2	2365.7	798.2	10.90
Daubechies 4	3	2366.3	686.2	11.89
Daubechies 8	2	2365.7	807.9	8.57
Daubechies 8	3	2366.2	688	11.82

After considering both the speckle index value and the resultant processed images a selection of optimum wavelet parameters were made. Comparison of the dc = 3 to dc = 2 images showed an over smoothing of dc = 3. Visual observation of the dc = 2 shows the level of smoothing to be minimal as compared to dc = 3. Results for the wavelet bases were similar in appearance over the bases tested, however the speckle index exhibited a maximum value of 10.90 for the wavelet base of Daubechies 4. Therefore the Daubechies 4 wavelet base with a decomposition of level two was selected as the optimum parameters based both on the higher speckle index and the visual characteristics of the resultant image. Figure 6.4 shows the result.

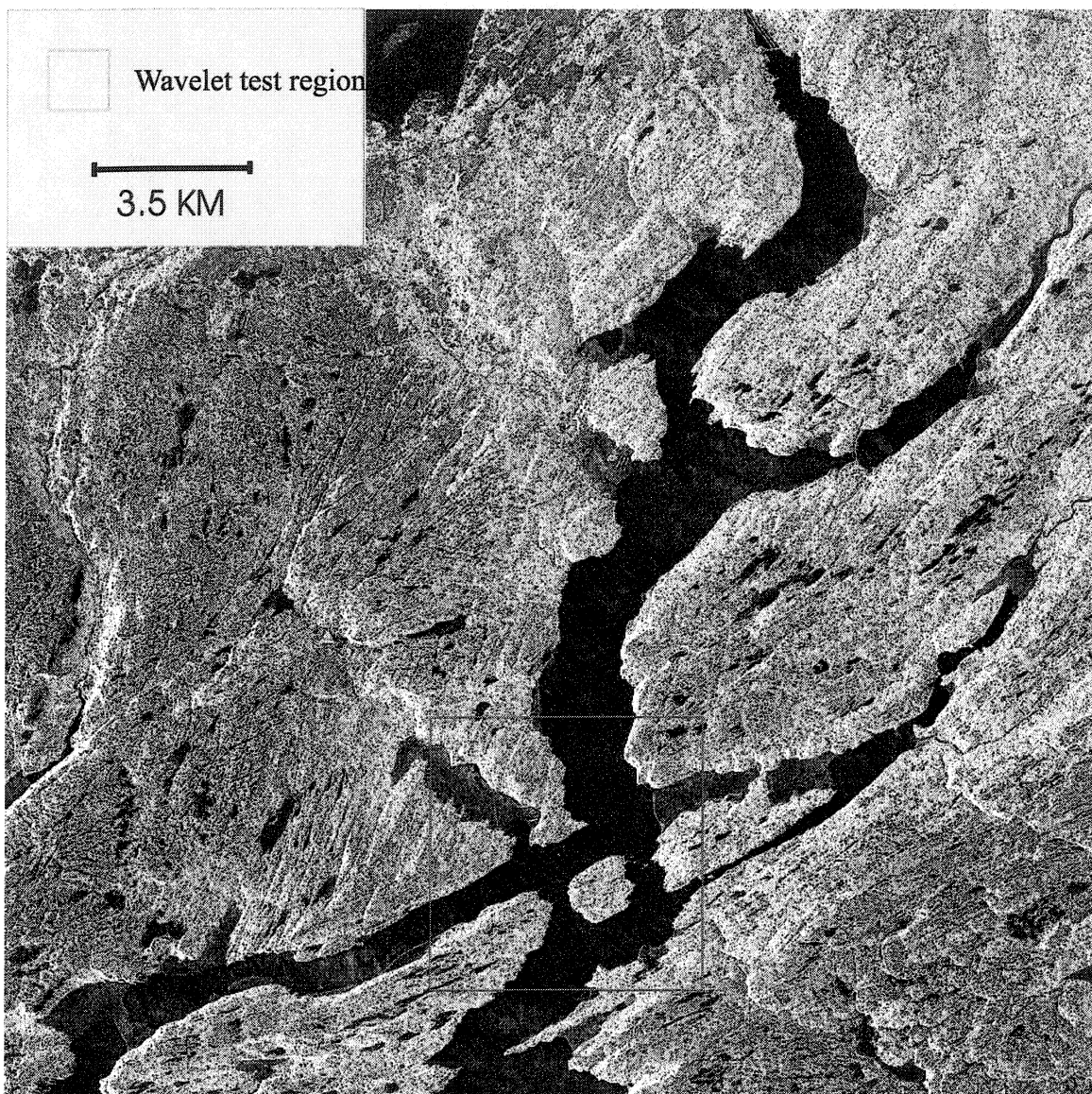


Figure 6.4 Speckle reduced image (Daubechies 4, dc=2)

6.2.4 Texture analysis

The texture analysis involved the selection of the most appropriate displacement vector and window size for each of the five texture measures applied.

Figure 6.5 shows an example of the relationship between texture measure with respect to each ice type. The graph is for the correlation texture with a 21X21 window size over all calculated displacement vectors.

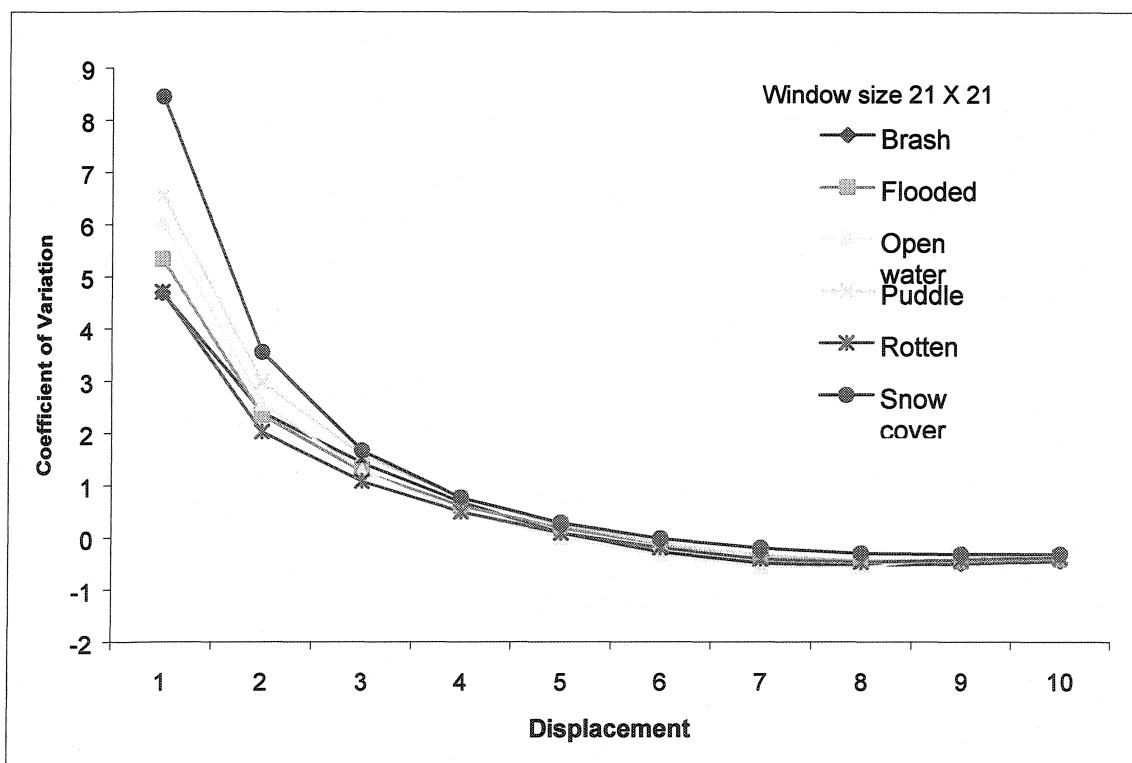


Figure 6.5 Effects of displacement on the coefficient of variation, correlation texture.

The coefficient of variation steadily decreases for all ice types up to a displacement of six, where values approach zero or below, exhibiting little or no change above this displacement. Where the correlation values of zero are shown, no spatial relationship in the scene texture is present. Also the coefficient of variation shows near complete overlap between ice classes at these displacements. This relationship implies a neighborhood effect at 7 pixels or less for the ice types studied.

Relationships similar to the above were observed for the angular second moment, homogeneity, standard deviation, and entropy texture measures as well. The coefficient of variation of the homogeneity texture measure, increases as the displacement vector increases with values stabilizing at displacements of six or seven. The maximum slope of the curve is observed at displacement values of two or three. The angular second moment texture measure shows an increase in the coefficient of variation with increased displacement vector. The maximum rate of change in the coefficient of variation occurs at displacements of two or three. At lags of four and above there is no perceived change in the coefficient of variation or separability between ice classes.

Entropy values show very little variation over the range of displacements calculated. Slight increases are observed at displacements of two or three with no perceived change at higher displacements.

Similar relationships are observed in each texture measure as the window size is decreased. Figure 6.6 illustrates the typical effect of windows size on the relationship between the displacement vector and the texture. This relationship is representative for all ice types characterized. The correlation texture measure exhibits the same downward trend for each of the three window sizes depicted in the graph.

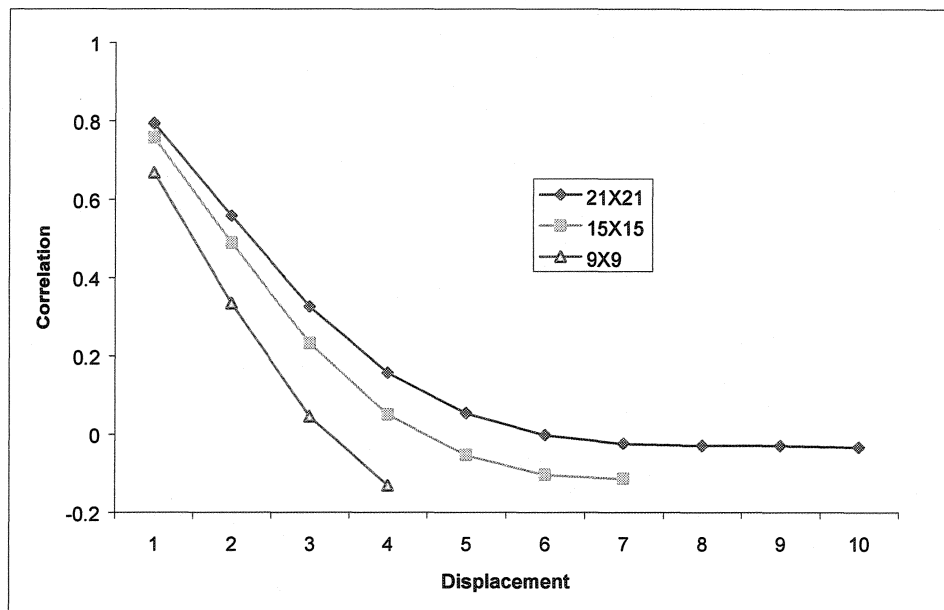


Figure 6.6 Effect of displacement on correlation texture measure with three different window sizes, for snow cover.

The texture measure of standard deviation shows a different relationship. Standard deviation shows a maximum at displacements of approximately one quarter the filter size for all filter sizes. That is for a 21x21 size filter the standard deviation reaches a maximum for a displacement of six. For filter size of 15x15, maximum is reached at spatial displacement of 4, 9x9 maximum is reached at spatial displacement of two or

three, and finally for a 7x7 filter size maximum is attained at spatial displacement of two (Figure 6.7)

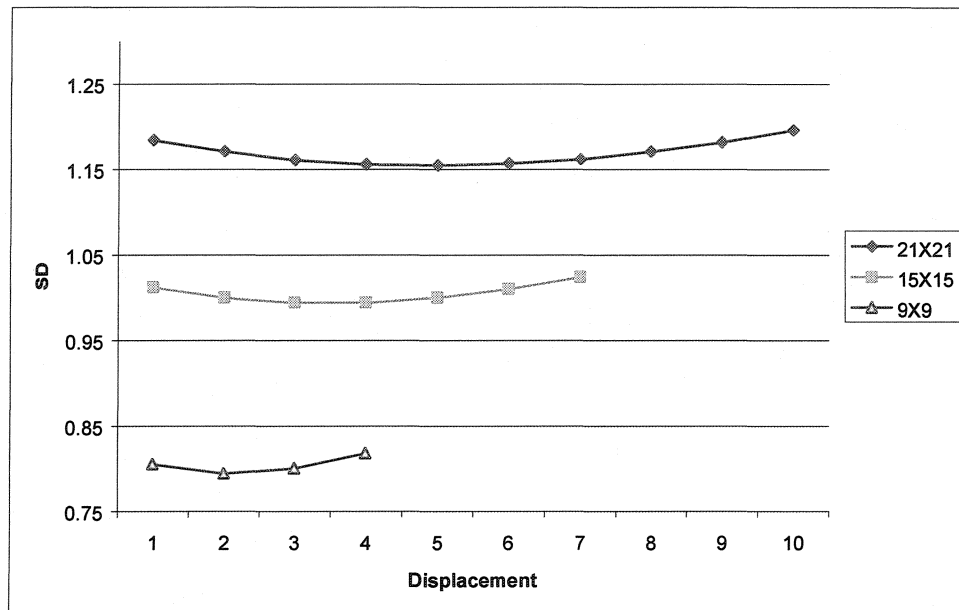


Figure 6.7 Effect of filter size for SD texture measure, for snow cover

Given the goal of reducing the coefficient of variation while maintaining signature separability, each of the five texture measures displayed the above at displacement vectors of two or three pixels. The optimum filter size is determined to be a 7 X 7 window given the neighborhood effects apparent in the correlation texture measures of Figure 6.5. After legs of 7 in the correlation texture measure, correlation values go to zero indicating no spatial relationship beyond 7 pixels.

Figures 6.8 illustrates the effects of displacement on each texture measure for different window sizes as calculated for the snow cover ice class. The relationships illustrated are similar for each of the other ice types. Angular second moment and correlation (Figure 6.8 a) and c)) exhibit similar relationships with their coefficient of variation decreasing with increased displacement, and at spatial displacement of two or three, maximum separation is seen. For Figure 6.8 b) and d) representing entropy and homogeneity respectively, the portion of each graph with the maximum rate of change in values, and minimum coefficient of variation occurs near spatial displacement lags of two or three. Figure 6.8 e) shows that value of standard deviation reach maximum at displacement lags of approximately one quarter the filter size. For a 7x7 filter size maximum is attained at spatial displacement of two.

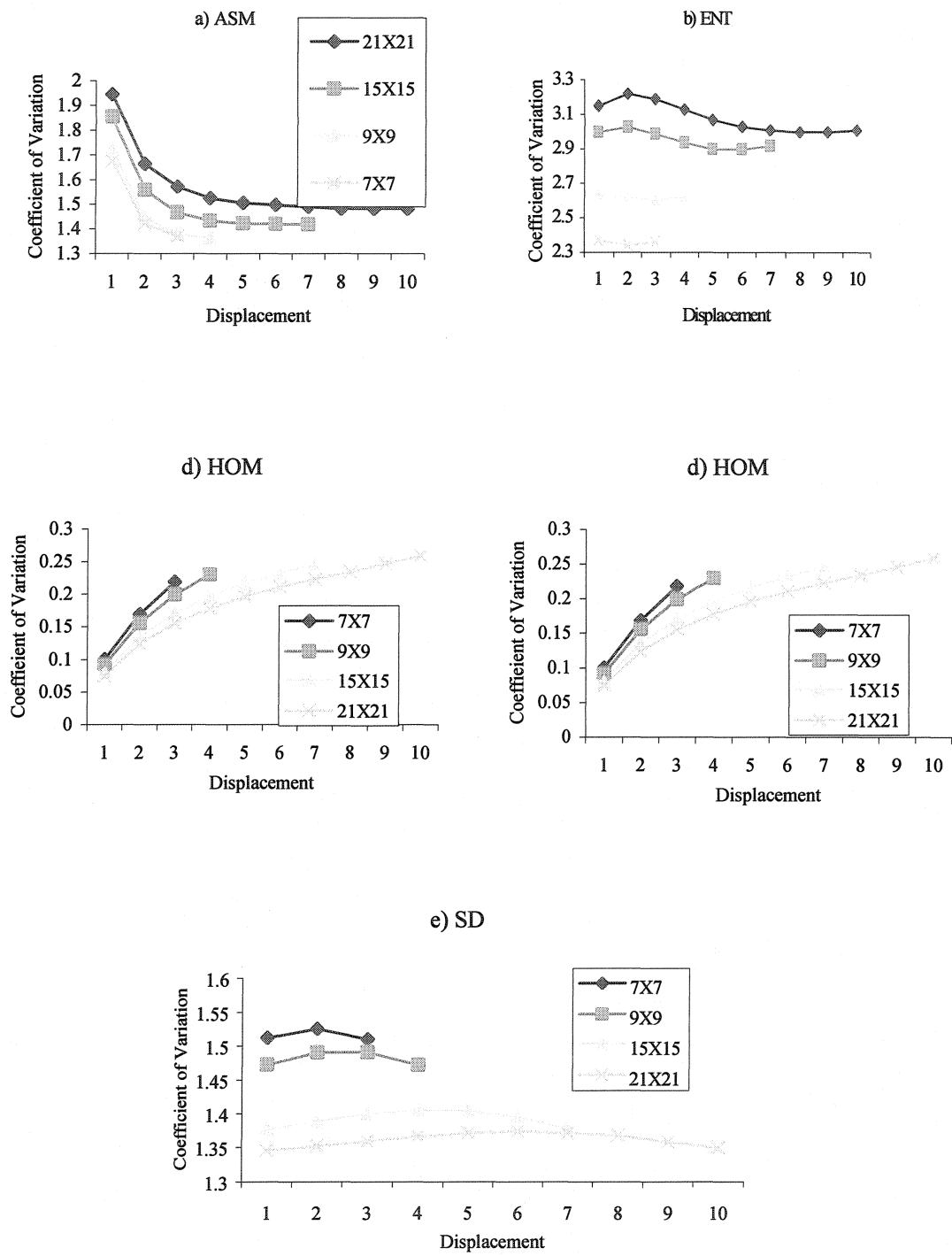


Figure 6.8 Effect of window size and displacement vector on texture measure for snow cover

Given the ambiguity between the displacement of two or three for each texture measure, further analysis was needed to define an optimum displacement vector. The final decision of displacement vector was based on signature separability, by extracting ice class signatures and calculating Bhattacharrya (or Jefferies-Matusita) distance for each texture measure over the two spatial displacements. The Bhattacharrya distance indicates class separation assuming normal distribution of the data (Swain and Davis, 1978).

Tables 6.6 through 6.10 compare the signature separability of each ice type for each texture measure as calculated with spatial displacement at two and three. Separability is similar for each texture measure with only slight improvement exhibited between each displacement. Based on the calculations, correlation, angular second moment, entropy and homogeneity, show slightly better separations between classes for spatial displacement of three, with differences in average separations of 0.03, 0.14, 0.04, 0.04 respectively, whereas the standard deviation texture measure shows better separability with displacement of two by an average difference of 0.01.

Table 6.6 Separability for COR texture measure at displacements of two and three

Legend	Displacement= 3			Displacement= 2		
	SC	FL	PD	RT	OW	BR
Snow Cover		0.35	0.29	1.82	1.61	0.61
Flooded	0.38		0.03	1.71	1.37	0.72
Puddle	0.33	0.04		1.81	1.57	0.75
Rotten	1.85	1.72	1.87		0.32	1.18
Open Water	1.65	1.38	1.63	0.33		1.01
Brash	0.63	0.73	0.81	1.19	1.12	

Table 6.7 Separability for ASM texture measure at displacements of two and three

Legend	Displacement= 3			Displacement= 2		
	SC	FL	PD	RT	OW	BR
Snow Cover		0.30	0.40	1.65	1.52	1.76
Flooded	0.33		0.04	1.67	1.64	1.87
Puddle	0.44	0.06		1.78	1.33	1.83
Rotten	1.68	1.68	1.84		0.33	0.99
Open Water	1.56	1.65	1.40	0.35		0.88
Brash	1.79	1.88	1.90	1.00	0.99	

Table 6.8 Separability for ENT texture measure at displacements of two and three

Legend	Displacement= 3			Displacement= 2		
	SC	FL	PD	RT	OW	BR
Snow Cover		0.41	0.32	1.85	1.7	0.73
Flooded	0.43		0.13	1.67	1.44	0.72
Puddle	0.36	0.15		1.76	1.53	0.89
Rotten	1.88	1.68	1.82		0.35	1.20
Open Water	1.75	1.45	1.60	0.37		1.11
Brash	0.75	0.73	0.95	1.21	1.21	

Table 6.9 Separability for HOM texture measure at displacements of two and three

Legend	Displacement= 3			Displacement= 2		
	SC	FL	PD	RT	OW	BR
Snow Cover		0.39	0.29	1.89	1.65	1.92
Flooded	0.41		0.02	1.87	1.52	1.96
Puddle	0.32	0.04		1.80	1.43	1.89
Rotten	1.92	1.88	1.87		0.30	1.00
Open Water	1.68	1.53	1.50	0.31		0.86
Brash	1.94	1.98	1.95	1.02	0.97	

Table 6.10 Separability for SD texture measure at displacements of two and three

Legend	Displacement= 3			Displacement = 2		
	SC	FL	PD	RT	OW	BR
Snow Cover		0.38	0.33	1.79	1.47	1.90
Flooded	0.35		0.04	1.69	1.27	1.69
Puddle	0.30	0.03		1.84	1.30	1.74
Rotten	1.75	1.68	1.79		0.28	0.97
Open Water	1.44	1.25	1.25	0.27		0.77
Brash	1.87	1.67	1.68	0.99	0.87	

6.2.4 Signature Statistics

The histograms of the training sites exhibited skewed distributions, which was evident in the difficulty of separating ice classes for each measure. The measure of separability assumes a normal distribution and may report inaccuracies when calculated on skewed distributions. Figures 6.9 to 6.14 present normalized histograms of each ice class as represented by the speckle reduced radar backscatter and five texture images. The training data shows symmetrical distributions for all ice classes for the radar backscatter, except brash, which exhibits a bi-modal distribution. However the training site statistics for the second order texture measures show distributions that are bimodal and highly skewed, with significant peaks throughout the histogram. For each ice type these peaks occur at the same location in the histogram, but exhibit different frequency between ice classes.

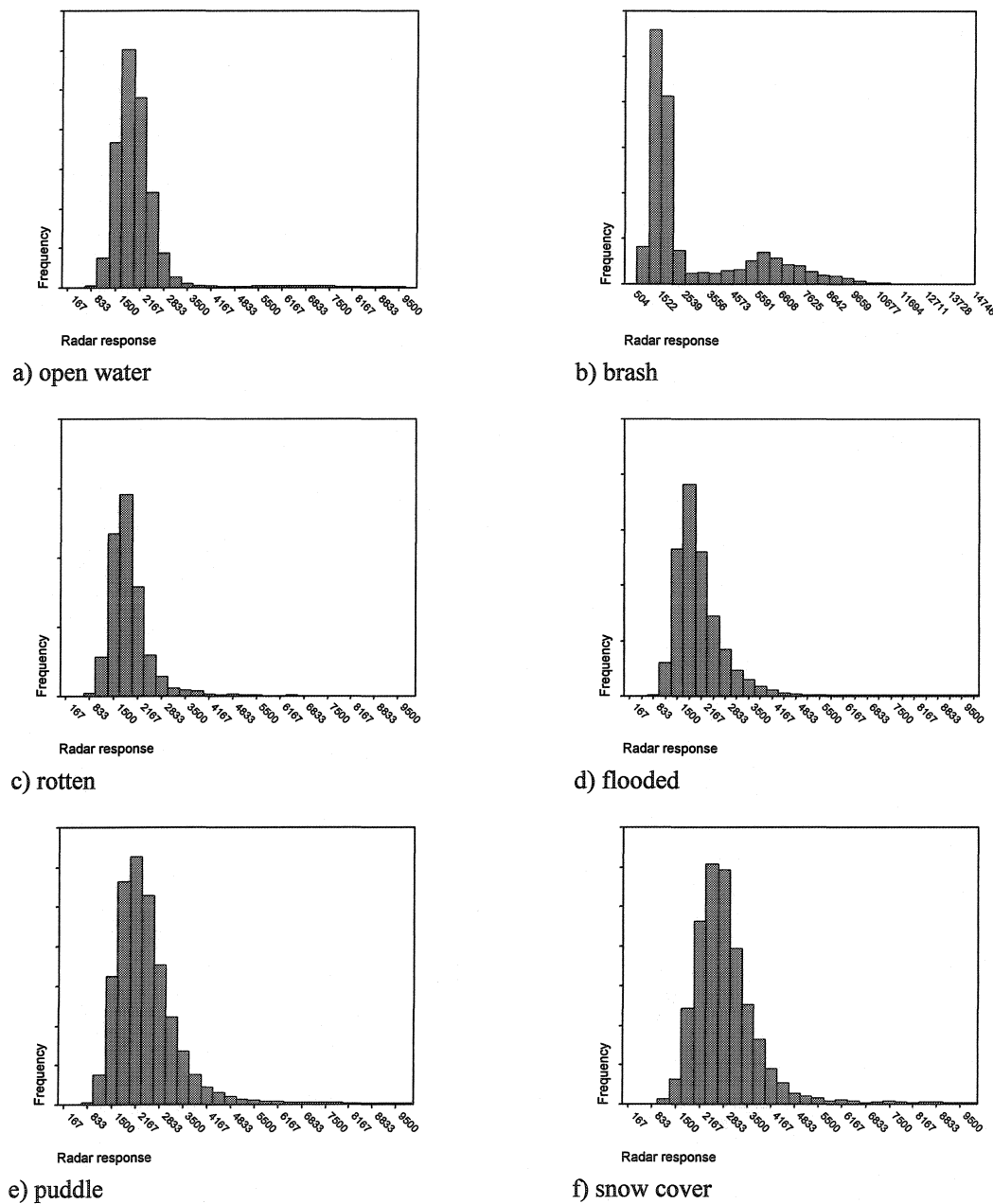


Figure 6.9 Normalized training statistics for radar backscatter

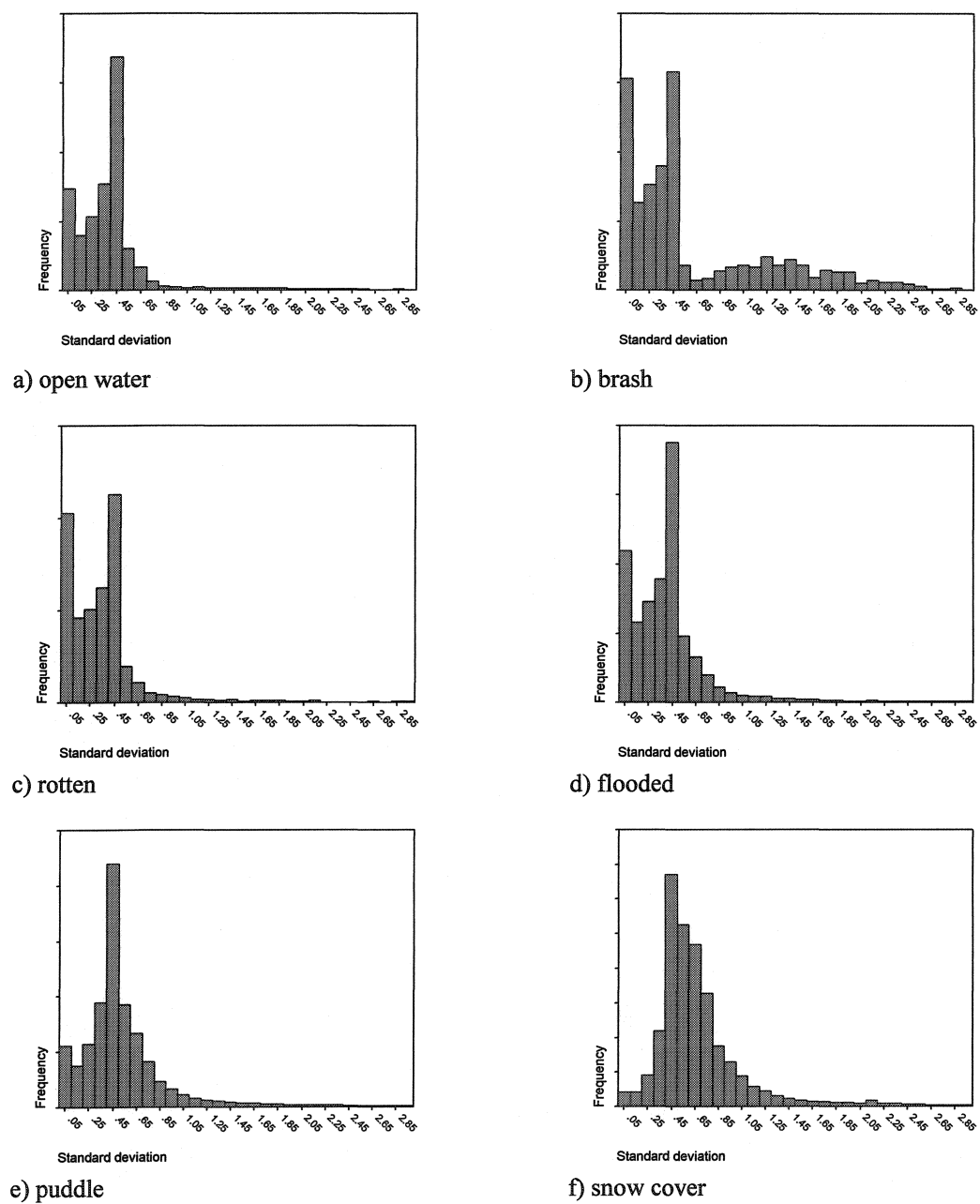


Figure 6.10 Normalized training statistics for SD texture measure displacement of two

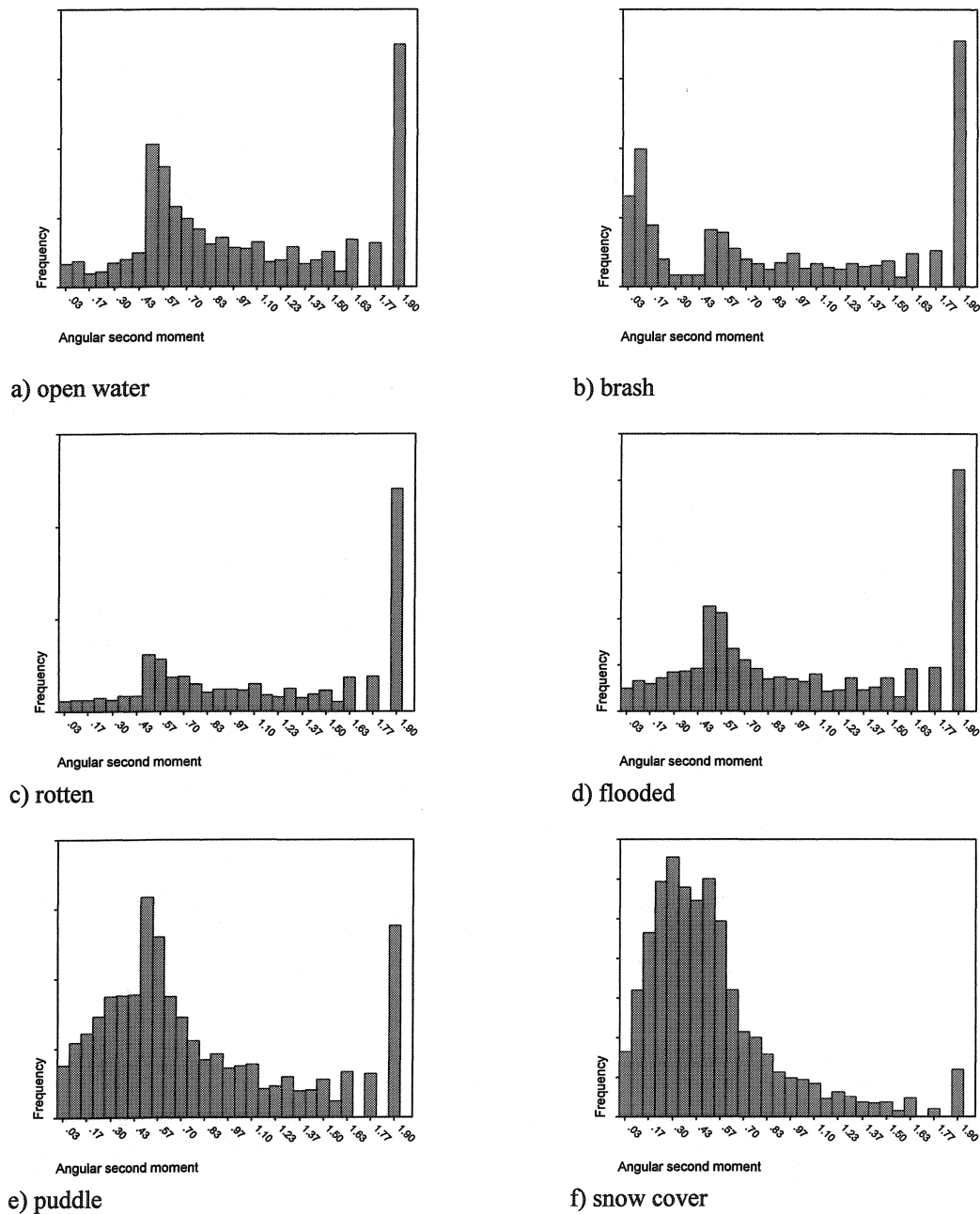


Figure 6.11 Normalized training statistics for ASM texture measure with displacement of three

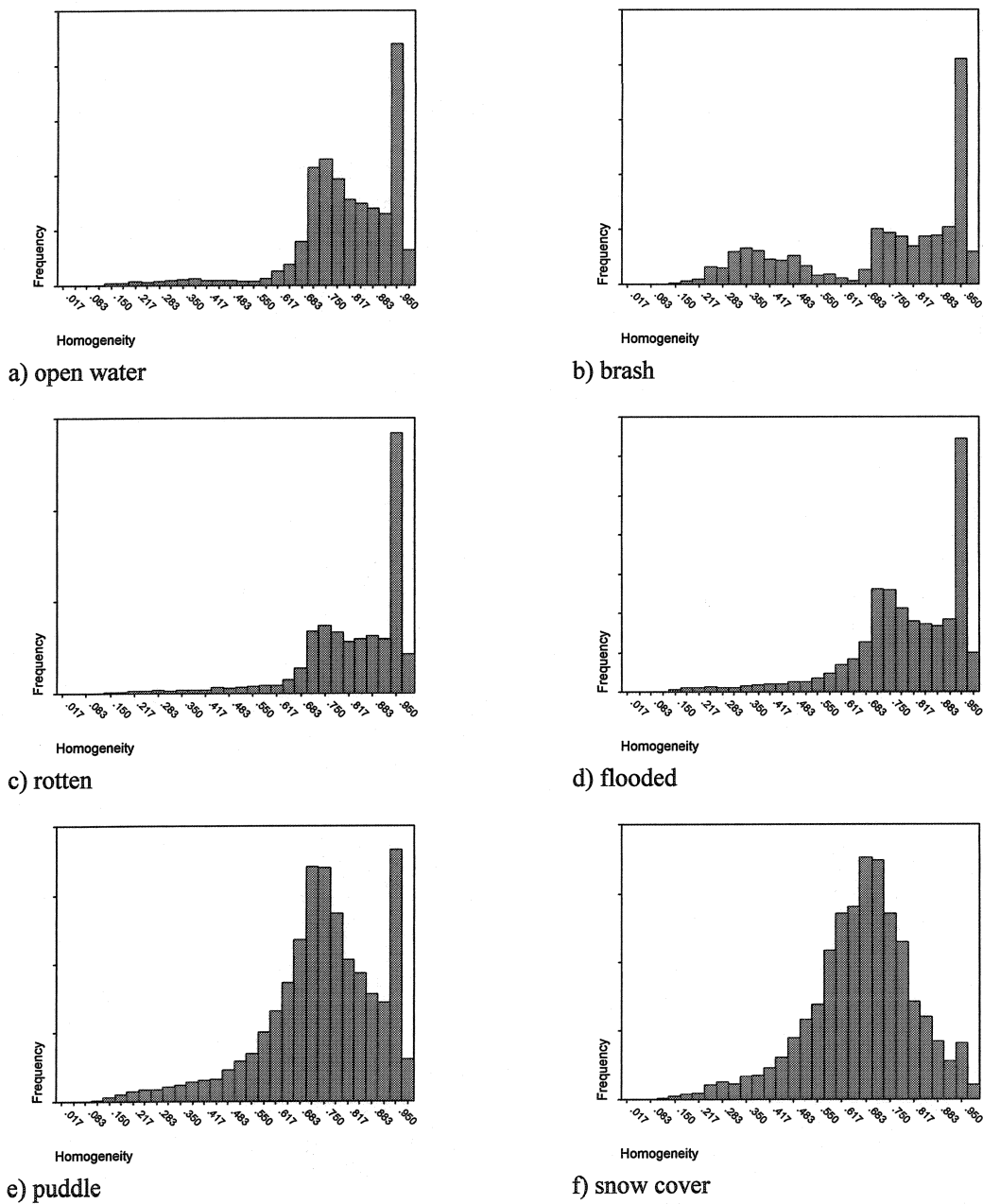


Figure 6.12 Normalized training statistics for HOM texture measure with displacement of three

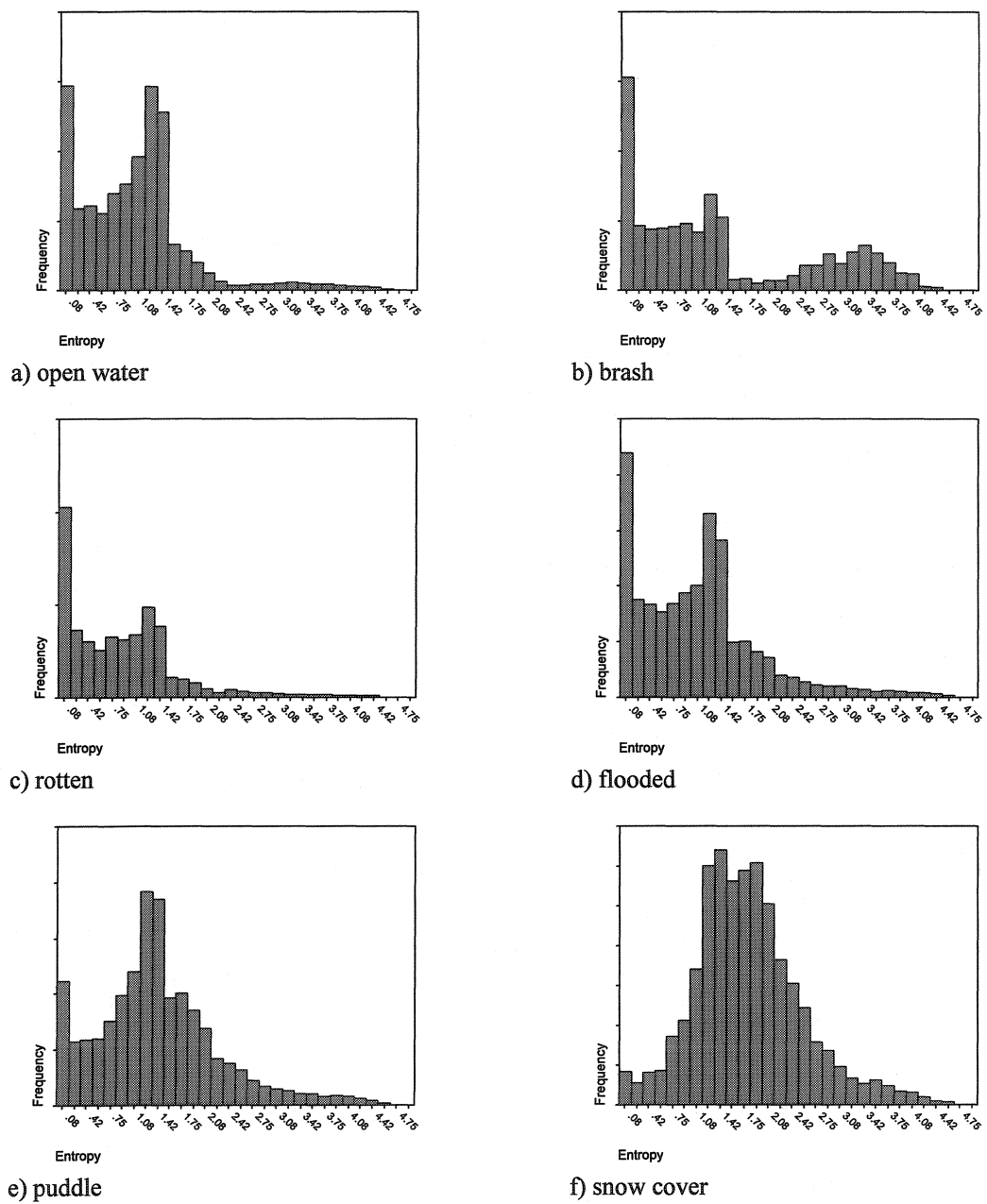


Figure 6.13 Normalized training statistics for ENT texture measure with displacement of three

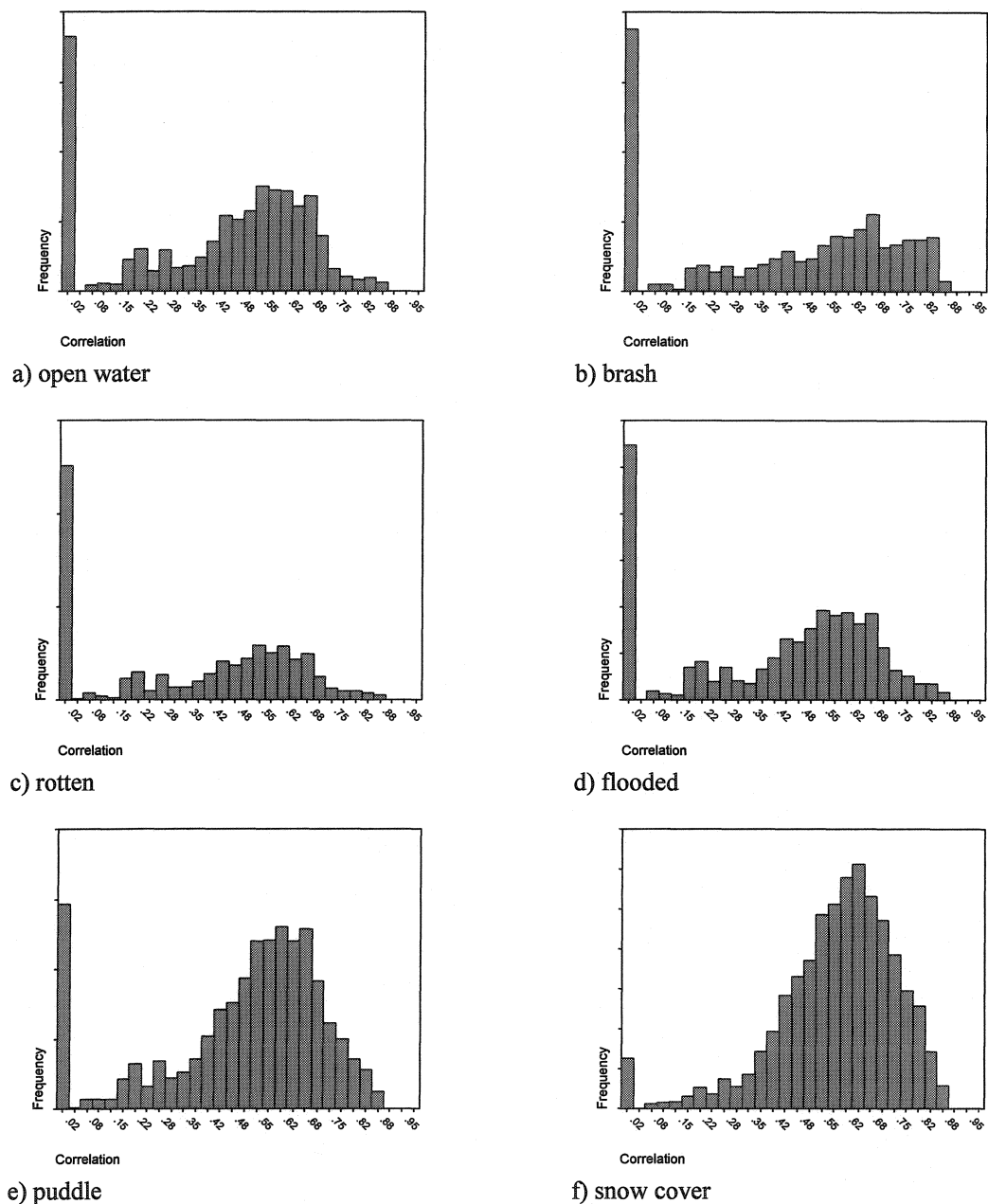


Figure 6.14 Normalized training statistics for COR texture measure with displacement of three

To extend the histogram representation to a classification approach, individual images were created to represent each histogram bin of the texture measure. Creation of

the histogram bin images requires knowledge of the signature histograms optimum bin width for each ice type. Table 6.11 presents the number of bins needed to represent each texture measure based on optimum bin width h_n as calculated by equation 5.4. The values were calculated for each texture measure, based on the texture measure range and the smallest sample size of all ice classes, which was brash ice. A single value for bin size was needed to calculate the bin images. Selecting the smallest sample size ensured no loss of information in this class, while preserving the information in the subsequent classes that exhibited higher samples.

Table 6.11 Optimum histogram bins for histogram characterization

Texture measure	Range	h_n	Number of bins
SD	6.39	0.2	32
ASM	1.96	0.22	9
HOM	0.78	0.07	12
ENT	4.75	0.4	12
COR	1	0.09	11

The number of images created to represent each bin of the histograms varies from nine, for the Angular Second Moment texture, to 32 for the standard deviation texture. The standard deviation texture measure database was very large (4 GB); however from studying the histogram of this dataset (Figure 6.15, a) a histogram tail trim of 2% would result in a more manageable range, with a little loss of data (Figure 6.15, b).

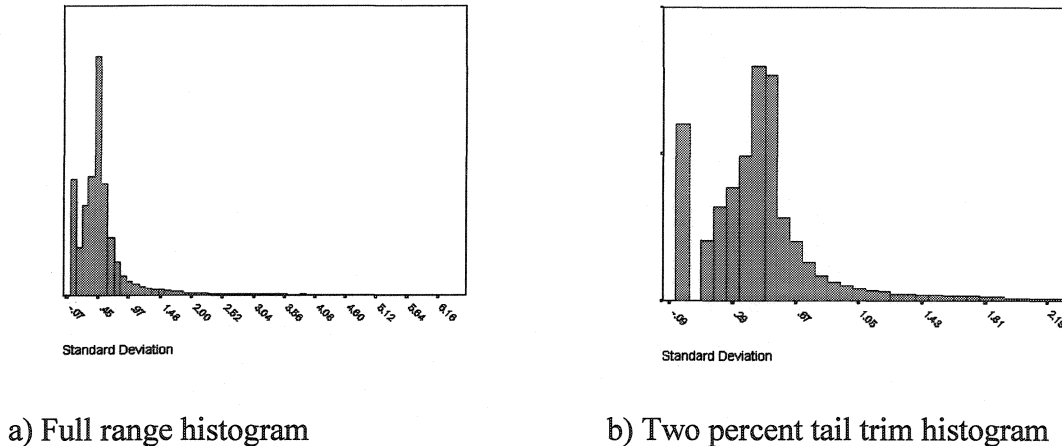


Figure 6.15 Standard deviation histogram comparison

With a two percent tail trim of the data the new working range for the standard deviation texture measure is now 2.2, rather than 6.39, and with the optimum histogram bin size of 0.2, the histogram for standard deviation can be represented with 11 bins.

Each of the resulting images is used in the classifications. For example the database file for the angular second moment texture measure now has 10 images including the 9 histogram bin images and the speckle filtered radar image (Table 6.12).

Table 6.12 ASM database structure

Channel number	Description
1	Speckle Filtered Radar
2	Bin 0.02 -0.24
3	Bin 0.24 -0.46
4	Bin 0.46 -0.68
5	Bin 0.68 -0.90
6	Bin 0.90 -1.12
7	Bin 1.12 -1.34
8	Bin 1.34 -1.56
9	Bin 1.56 -1.78
10	Bin 1.78 -2.00

Signature separability was assessed using the histogram bin images. An average difference of 0.82 in separability was revealed with the addition of the bin images in the classification (Table 6.13 and Table 6.14). Between class separation measure increase for all ice types with highest improvements of 1.54 for Rotten vs. Open water, to a low of 0.27 for Flooded vs. rotten.

Table 6.13 Bhattacharrya distance for backscattered and correlation texture images

	Snow Cover	Flooded	Puddle	Rotten	Open Water
Snow Cover					
Flooded	0.38				
Puddle	0.33	0.04			
Rotten	1.85	1.72	1.87		
Open Water	1.65	1.38	1.63	0.33	
Brash	0.63	0.73	0.81	1.19	1.12

Table 6.14 Bhattacharrya distance for correlation with the bin images included

	Snow Cover	Flooded	Puddle	Rotten	Open Water
Snow Cover					
Flooded	1.78				
Puddle	1.62	0.94			
Rotten	2.00	1.99	1.99		
Open Water	2.00	1.98	1.99	1.87	
Brash	1.98	1.98	1.98	1.99	1.91

6.3 Neural network classification

The histogram characterization procedure resulted in a number of bin images associated with each texture measure. These bin images, along with a 15 X 15 mean filtered image of the radar backscatter were used as neural network inputs. Table 6.15 illustrates there are 10 images used as input layers for the ASM neural network. These include the 9 bin images and a 15 X 15 mean filtered image of the radar backscatter.

Table 6.15 Neural network input channels

Classification	Texture	Number of inputs
1	Standard Deviation	12
2	Angular Second Moment	10
3	Homogeneity	13
4	Entropy	13
5	Correlation	12

Training of the multi layer perceptron (MLP) neural network required that it be exposed to the six sets of sample data corresponding to the five ice types plus open water. The weight adjustments used one thousand iterations for each of the texture networks. The iteration process changes the weights as samples are fed forward, and the normalized total error is back propagated through the network. The process continues until the network reaches a predetermined level of error or the number of iterations is met.

“The total error reported in a neural network must be considered only as a measure of how well the network can reproduce the training data; no inferences into its ability to accurately classify unseen pixels can be made. This total error is propagated back through the network in its learning process” (Atkinson and Tatnall, 1997).

Figure 6.16 illustrates the total error as reported for the standard deviation MLP. For example, with the standard deviation MLP, the normalized total error is about 55% at initialization, and is reduced to 36% after 1000 iterations.

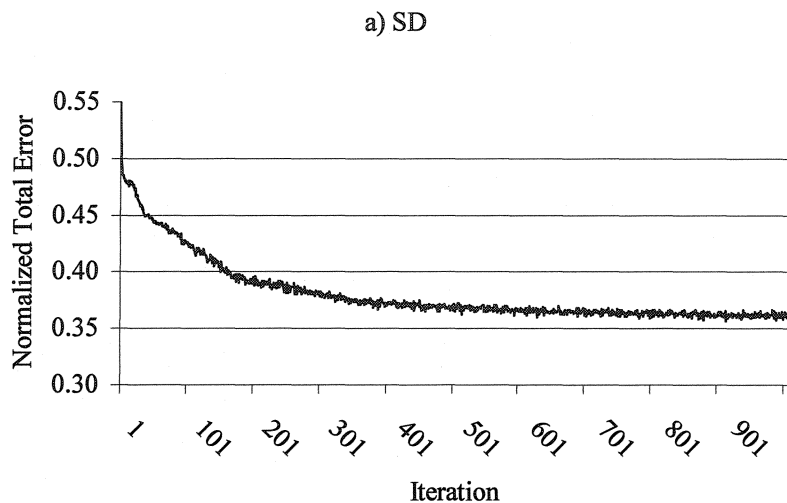


Figure 6.16 MLP Normalized total error for SD texture measure

Table 6.16 reports the final level of total error reached by each of the networks training processes. Normalized total errors ranged between a low of 34.6% for the homogeneity texture neural network, and a high of 39.9 % for the angular second moment texture neural network. This corresponds to the MLP being able to reproduce the training data correctly between 65.4% with the homogeneity inputs and 60.1% with the angular second moment inputs.

Table 6.16 MLP total error

Texture Neural Network	Normalized Total Error (%)
Standard Deviation	36.0
Angular Second Moment	39.9
Homogeneity	34.6
Entropy	35.2
Correlation	34.8

6.4 Classification results

Classification of the entire data set was performed with the trained neural networks. The resulting images are presented in Figures 6.17 to 6.21. Visual characteristics of the five classifications showed similar distributions of the five ice types plus open water. The snow cover class showed limited distribution, near the shoreline and in a few very sheltered coves. During video collection there was only a small amount of snow covered ice remaining in the study area. On the classified image the majority of the ice was either flooded or rotten, limited patches of puddle were visible throughout the region. Brash ice, the most dynamic of the five ice types studied, was classified on several of the south eastern shores of the bay system, as well adjacent to some consolidated ice covers with the same orientation.

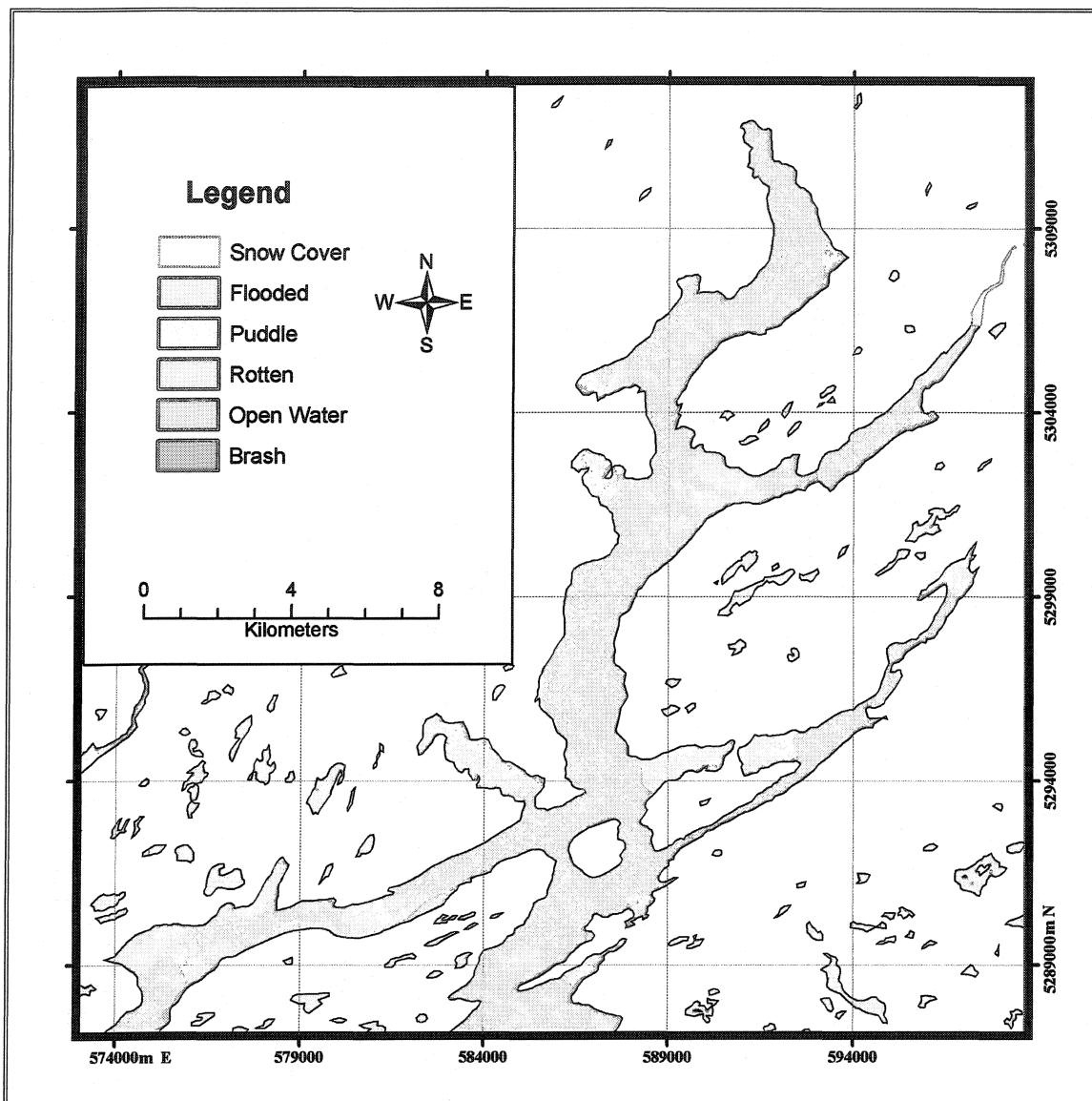


Figure 6.17 Standard deviation ice classification results

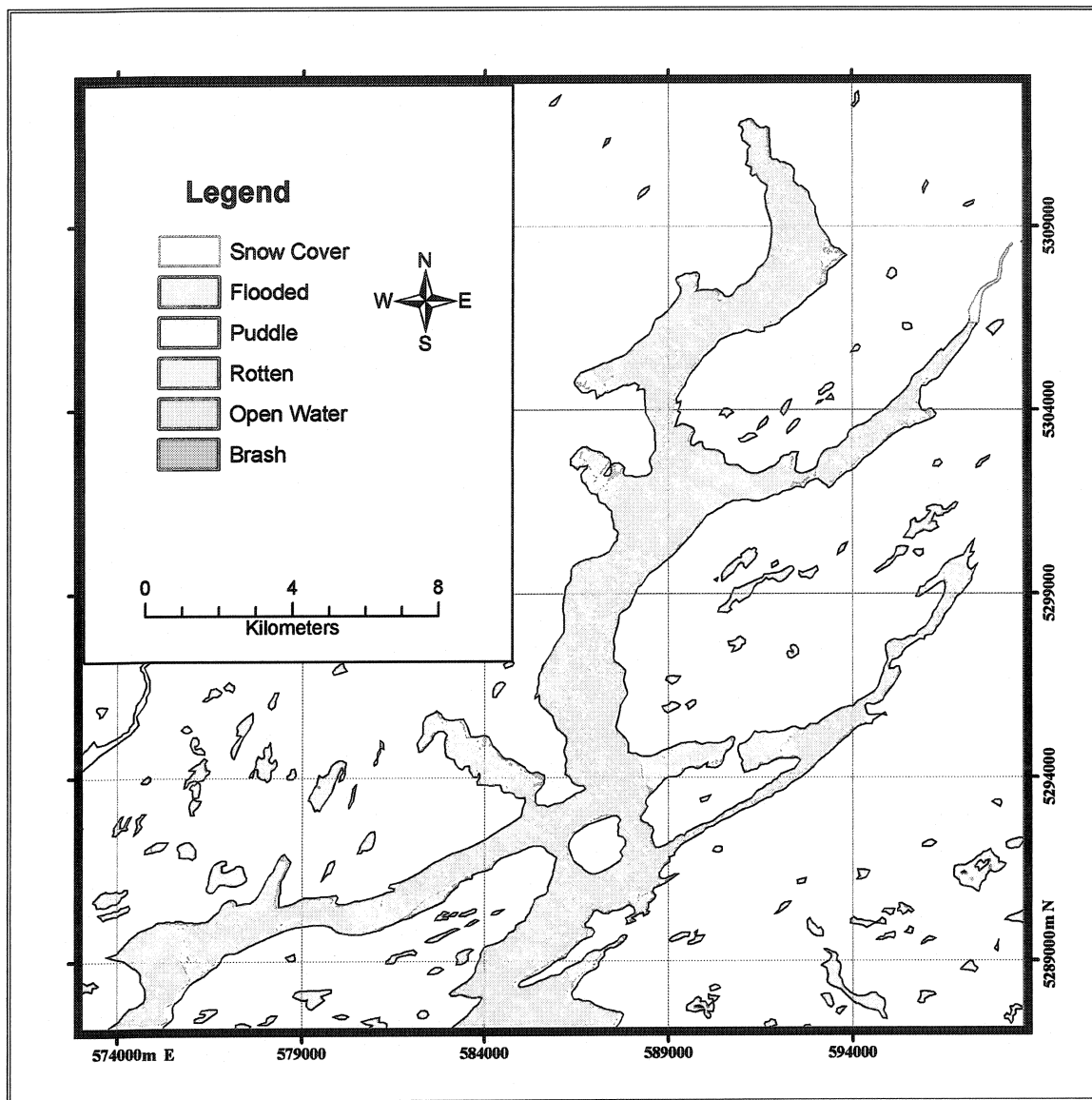


Figure 6.18 Angular Second Moment ice classification results

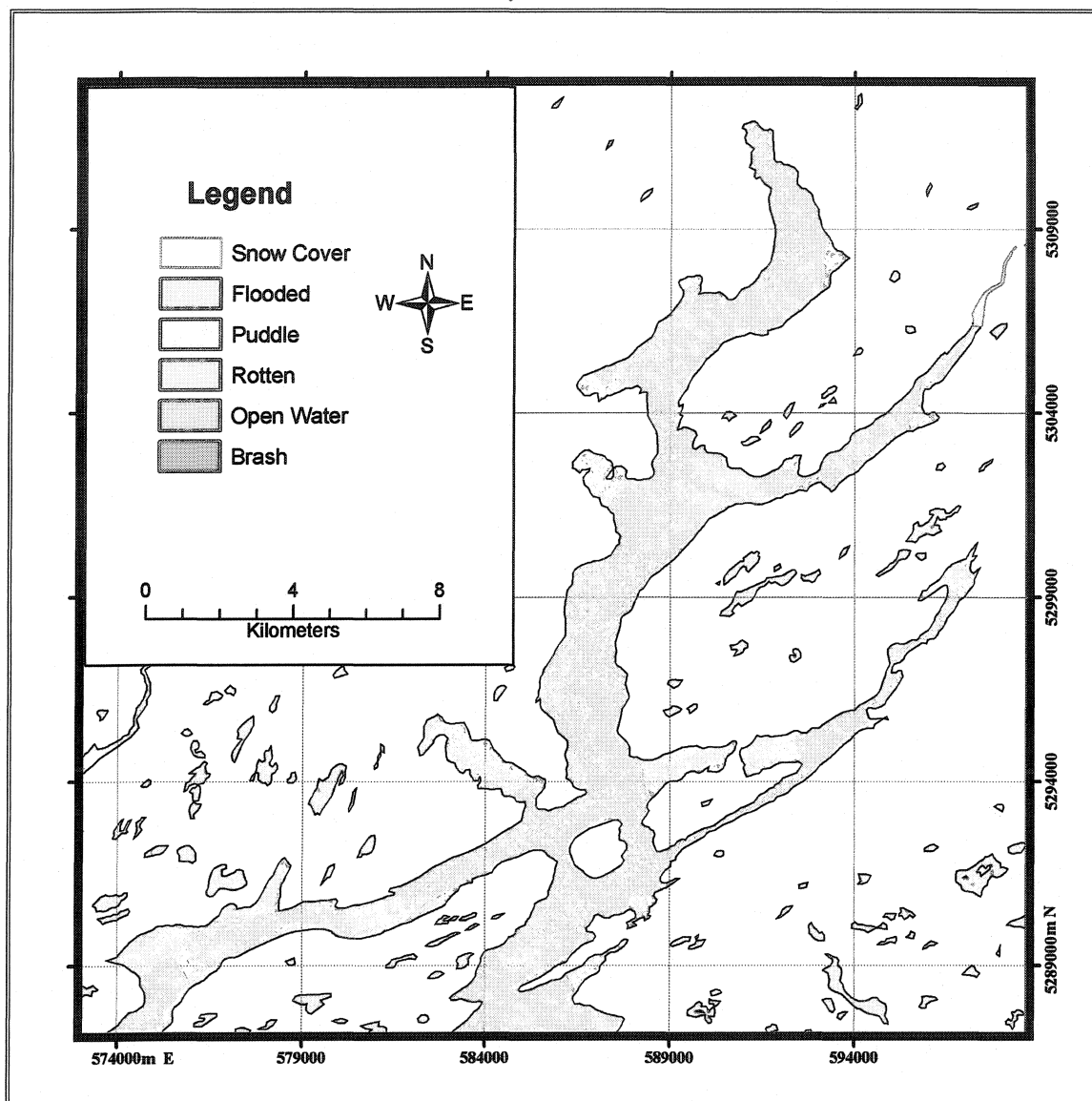


Figure 6.19 Homogeneity ice classification results

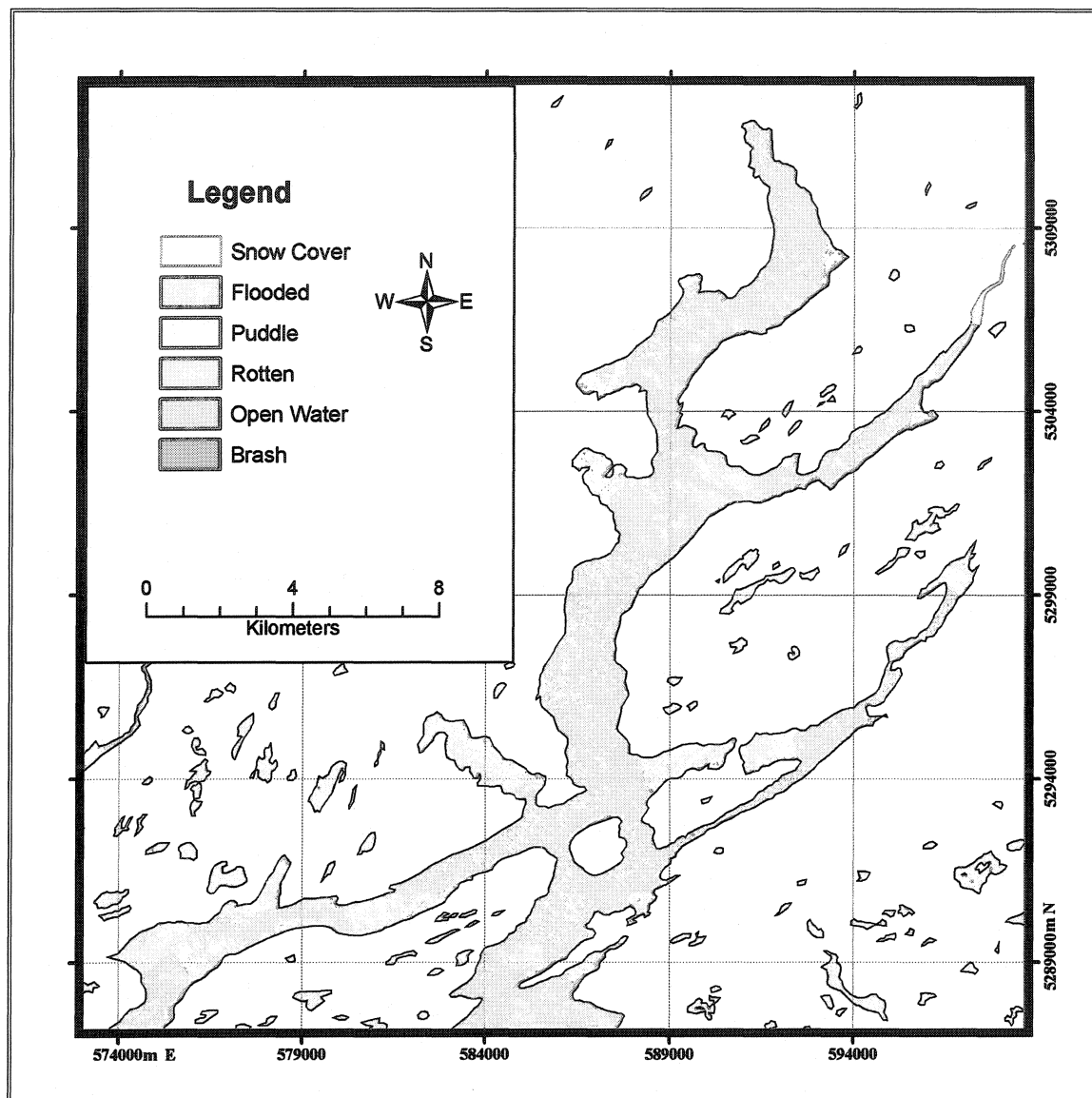


Figure 6.20 Entropy ice classification results

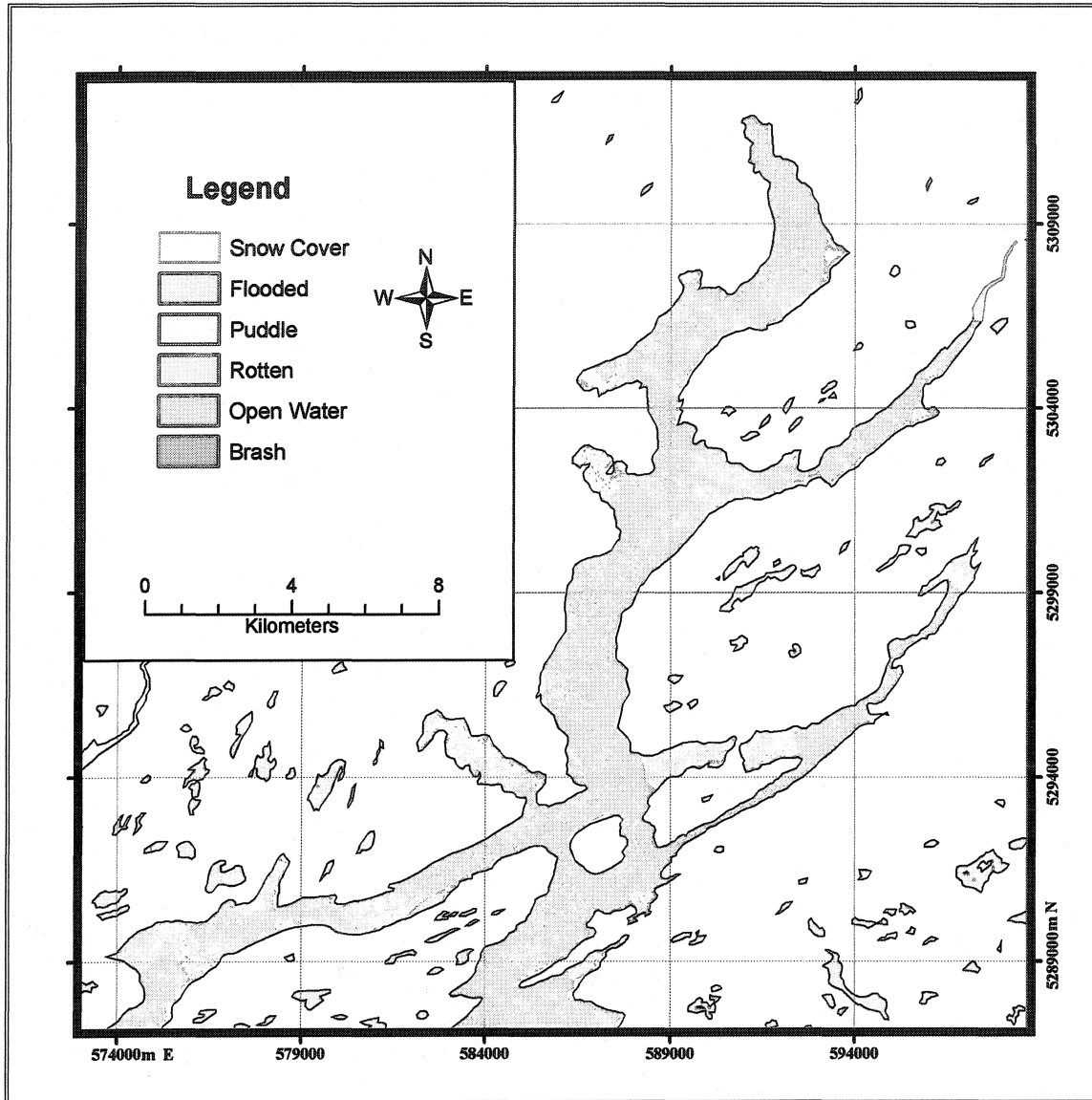


Figure 6.21 Correlation ice classification results

Table 6.17 shows the percent coverage for each ice type in the study area, as classified using each texture measure. As expected the majority of the study area was covered by open water (nearly 50%) in the classified images. The percent total coverage for each texture approach is compared to the video mosaic result, which includes the

classified video only, and does not include the large areas of unclassified data. This is evident when comparing the total coverage of open water. In the video mosaic there was only 22% classified open water, while in reality the study area contains a much higher amount at the time of video acquisition, but was not included in the video. There is also a difference in the coverage of puddle and rotten ice with the respective coverage switching magnitudes between the video and the classification. This is attributed to change in the ice cover between video acquisition and image acquisition or through similarities in surface characteristics of these two classes.

Table 6.17 Percent total coverage of ice type as calculated by texture measures.

Ice type	Video mosaic (%)	ASM (%)	HOM (%)	ENT (%)	COR (%)	SD (%)
SC	8	8.1	5.5	4.4	7.1	4.4
FL	29	20.4	24.4	26.3	16.6	26.5
PD	32	1.6	3.6	2.1	7.3	1.4
RT	7	24.9	22.6	16.0	17.4	22.6
OW	22	41.4	42.1	49.1	47.2	41.5
BR	15	3.6	1.9	2.1	4.3	3.6

6.5 Accuracy assessment

This section reports the accuracy assessed for each ice type classification and compares the performance of the texture measures for each class and overall error. The accuracy assessment of the classified images by means of the verification data resulted in the error matrices for each of the texture based neural networks.

6.5.1 Classification accuracy

The results of each of the error matrices showed very similar behavior between texture measures with comparable accuracies reported across each ice type, the standard deviation texture measure exhibited the lowest overall accuracy and a description of the errors are presented as an example. The standard deviation based texture method has an overall accuracy of 58.11% with a Kappa statistic of 0.45 indicating that the classifier is 45 % better than the chance classifier or random assignment of pixels. Kappa agreement values less than 0.4 are poor, 0.4 to 0.75 are good and greater than 0.75 are excellent (Rosenfield and Fitzpatrick-Lins, 1986) The results show excellent ability to map brash and open water, with user's accuracies of 95% and 86 % respectively. Varying degrees of success with the other classes is also exhibited (Table 6.18).

Brash shows user's accuracy of over 95% with a commission error of 5%. The classification of open water has a user's accuracy of over 86%; this class shows a 12.8% commission error with rotten. This commission error can be attributed to the variability in

the rotten ice verification data. Also rotten ice can change to open water in a matter of hours under heavy wave action or high temperatures. Therefore what was labeled to be rotten ice in the verification data set could have actually been open water.

Table 6.18 Standard deviation error matrix

Classified	Reference								Kappa
	SC	FL	PD	RT	OW	BR	Total	UA (%)	
SC	134	22	110	0	0	0	266	50	0.47
FL	20	270	316	9	206	0	821	33	0.25
PD	28	37	110	0	0	0	175	63	0.55
RT	0	2	0	298	358	74	732	41	0.31
OW	0	0	0	146	975	18	1139	86	0.72
BR	2	2	0	0	1	87	92	95	0.94
Total	184	333	536	453	1540	179	3225		
PA (%)	73	81	21	66	63	49			
Overall Accuracy 58%									
Kappa Statistic 0.45									

Puddle exhibits a user's accuracy of over 63%, commission errors with snow cover are about 16%. This commission error can be attributed to similarities in the ice surface. During the week preceding image acquisition extensive melting occurred, the snow cover ice would result in the presence of considerable liquid water in the snow pack causing the formation of pooled water, also for the puddle ice class, more water has pooled. Puddle exhibits a commission error of 21% with flooded; this error can be attributed directly to the melting progression of the ice surface.

Snow cover shows user's accuracies of over 50% with commission errors with puddle and flooded at 41% and 8 % respectively. The commission error with these ice types can again be attributed to progression of the melting process, with their associated values showing more of the snow covered ice to be at the stage of puddle than through to flooded.

Flooded ice exhibits a user's accuracy of 33% with an associated poor Kappa statistic. These low values can be attributed to problems in discriminating flooded ice from puddle and open water. Flooded shows very high commission errors with puddle and open water at 38% and 25% respectively. The first commission error can be attributed to similarities in surface characteristics. During the progression from snow cover to open water, the boundary between the classes of flooded and puddle is a subjective one based on the amount of standing water visible on the ice surface. The open water commission error can be attributed to change, as the ice progressed from the flooded class through rotten and finally to open water. This error could also be attributed to similarities in the surface itself. If the depth of water on the flooded ice is sufficient and the area is large enough, wave patterns could allow the surface to "look" the same to the radar as open water.

Rotten ice has a poor user's accuracy of 40% with a Kappa statistic of 0.31. The classifier exhibits difficulty in discriminating rotten ice from open water, resulting in the low value. The rotten ice class shows very high commission error with open water at

49%. While much of this error is likely due to change of the ice cover through the progression of the melting cycle, some of this error could be attributed to the variability in the labeling of this class in the verification data as described above.

Tables 6.19 through 6.22 present the accuracy statistics for each of the other texture based neural networks. Each of the texture measures showed high user accuracies with brash and open water, varying degrees of accuracy are reported for the other ice types.

Table 6.19 Angular second moment error matrix

Table 6.20 Homogeneity error matrix

Table 6.21 Entropy error matrix

Table 6.22 Correlation error matrix

Classified	Reference								Kappa
	SC	FL	PD	RT	OW	BR	Total	UA (%)	
SC	148	31	140	0	1	0	320	46	0.43
FL	2	191	131	9	213	0	546	35	0.28
PD	32	101	261	2	7	0	403	65	0.58
RT	0	0	0	226	226	66	518	44	0.34
OW	0	6	0	216	1082	25	1329	81	0.64
BR	2	4	4	0	11	88	109	81	0.80
Total	184	333	536	453	1540	179	3225		
PA	80	57	49	50	70	49			
Overall Accuracy 62%									
Kappa Statistic 0.48									

6.5.2 Texture accuracies comparison

The ability of each of the five-texture measures to classify the ice classes in the study area is similar, with the overall accuracies ranging from 58.11% for standard deviation texture measure to 62.17% for the entropy texture measure. Kappa ranges of 0.45 to 0.49 are observed (Table. 6.23).

Table 6.23 Texture measure accuracy comparison

Texture Neural Network	Overall Accuracy (%)	Kappa statistic	Kappa variance
SD	58.11	0.45	0.000099
ASM	59.57	0.46	0.000138
HOM	61.92	0.49	0.000112
ENT	62.17	0.48	0.000115
COR	61.89	0.48	0.000108

Determination of the statistical difference of each of the textural classifier requires a Z-test. Congalton, (1991) illustrates the analysis of Kappa as a test of significant difference between error matrices as defined by equation 6.1.

$$Z = \frac{\hat{K}_A - \hat{K}_B}{\sqrt{\sigma_{K_A}^2 + \sigma_{K_B}^2}} \quad 6.1$$

where: K :Kappa statistic

σ^2 :variance of Kappa

Using a 95% confidence interval ($\alpha = 0.05$) the test statistic must exceed 1.96 for the Kappa values to be significantly different. Table 6.26 illustrates the pair wise comparison of Kappa values for each textural classifier. The standard deviation textural approach is statistically different from Homogeneity, Entropy and Correlation, while all others are not significantly different.

Table 6.24 Z-value test for significance between Kappa

	SD	ASM	HOM	ENT	COR
SD	0	0.64957	2.753	2.051	2.085
ASM		0	1.897	1.257	1.275
HOM			0	0.6637	0.6742
ENT				0	0
COR					0

Exploring the similarities of the texture measures through the user's accuracy confirms the above similarities as expressed by Kappa. Figure 6.22 illustrates that with respect to user's accuracy there is very little difference between the five neural networks. Open water and brash have the highest user's accuracies across all texture measures; however, the user's accuracy for brash is lower in the correlation texture measure. Puddle, snow cover, rotten, and flooded are next to follow with respect to user's accuracy, showing minimal differences between texture measures.

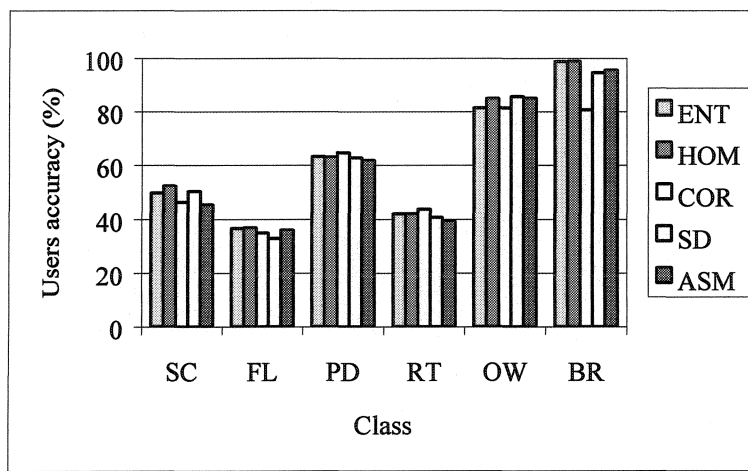


Figure 6.22 User's accuracies across textures by class

Evaluation of the commission error by ice class can be used to identify capabilities of individual textures at identifying particular ice classes. Brash (Figure 6.23), was successfully classified in each of the five texture approaches, with the highest commission error occurring in the correlation texture measure, producing a 10% commission error with open water. The commission error of brash against all other classes exhibit values less than 4% for the five texture measures.

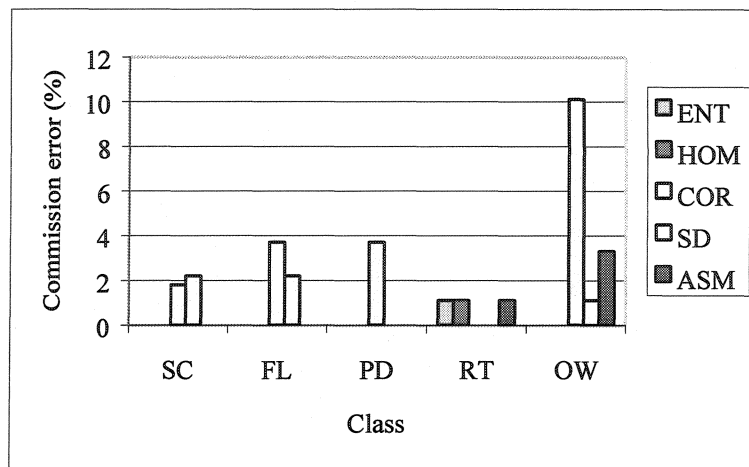


Figure 6.23 Brash, class commission errors by texture measure

Figure 6.24 reports the commission errors of open water as described in section 6.5.1. The commission errors with rotten are evident over all texture approaches. Standard deviation texture exhibits the lowest commission error between open water and rotten at 13 %, while entropy displays the highest error at 16.5 % which is statistically significant at the 95% confidence interval. Less than two percent commission error was exhibited with brash ice, and no other commission errors produced with the other classes.

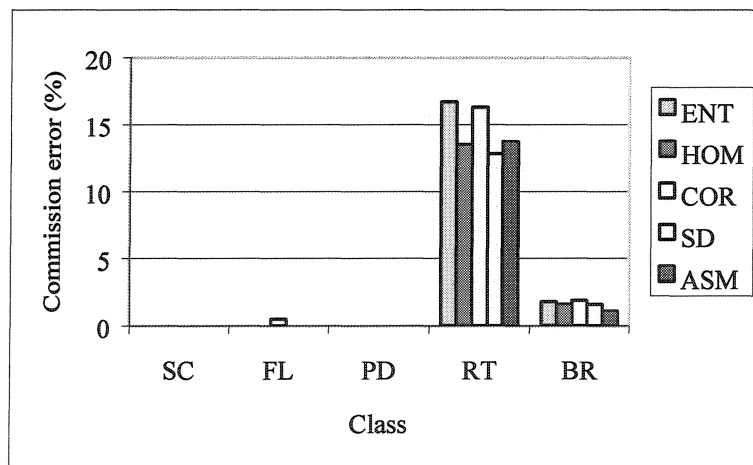


Figure 6.24 Open Water, class commission errors by texture measure

Figure 6.25 displays the commission errors of puddle with the other classes. Errors with snow cover and flooded are evident across all five texture measures, with flooded exhibiting the higher errors in the order of 20% and snow cover producing errors in the order of 15%. However for the correlation texture measure commission errors are reduced for snow cover at 7% and increase in the flooded class to 25%.

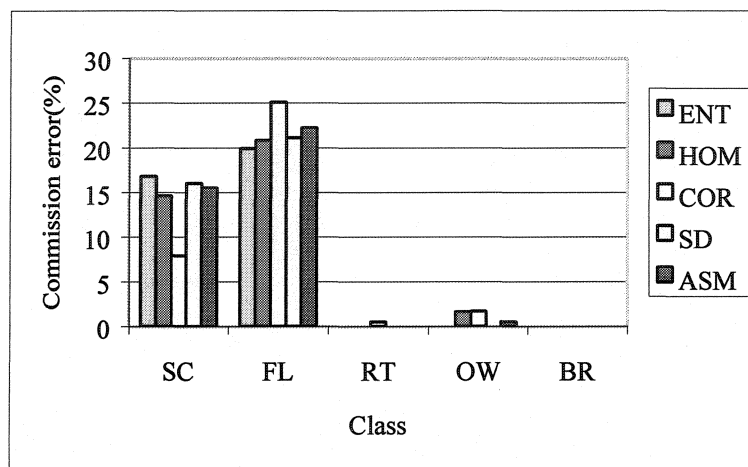


Figure 6.25 Puddle, class commission errors by texture measure

Snow cover commission errors are presented in Figure 6.26, which shows little variation between texture measures. Puddle commission errors on the order of 40% to 45% are evident and flooded exhibits errors on the order of 7% to 11%. No commission errors occur between snow cover and rotten, brash, or open water.

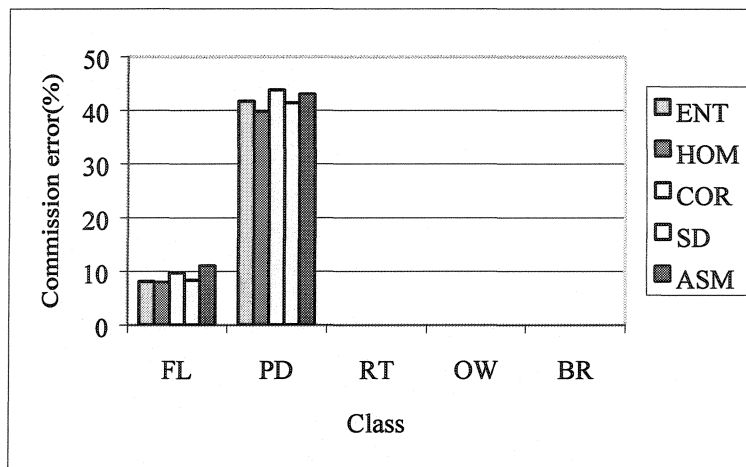


Figure 6.26 Snow Cover, class commission errors by texture measure

The commission errors for flooded show similar values across all texture measures (Figure 6.27). Errors are on the order of 20% to 25% for open water, and 35% to 40% for puddle, while other classes show errors of less than 2%. Again, the correlation texture measure shows some deviation with respect to the commission errors reported. The commission error of open water increases by 15% from the range of 20% to 25% to a high of nearly 40%. Conversely the errors with puddle are reduced by approximately the same amount.

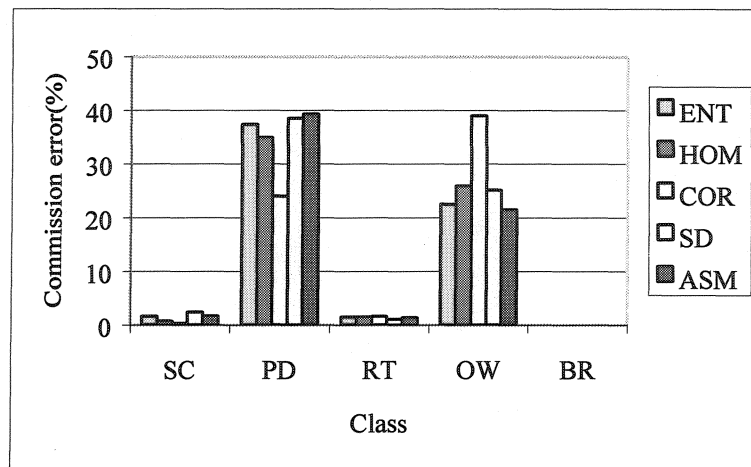


Figure 6.27 Flooded, class commission errors by texture measure

Finally with respect to rotten, the commission errors show little variation between texture measures on each class as seen in Figure 6.28. Errors with open water are on the order 45% to 50% for each texture measure. Commission error between rotten and brash is near 10% for each of the five texture measures.

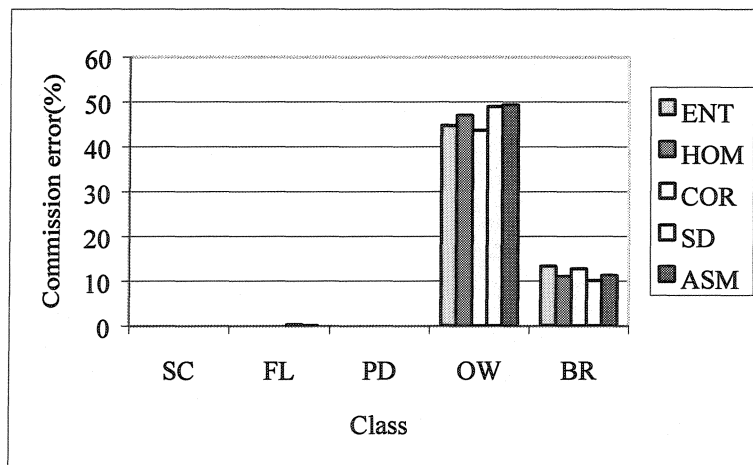


Figure 6.28 Rotten class commission errors by texture measure

7.0 Discussion

The strengths and weaknesses of the methodology with respect to aerial video reconnaissance and radar image processing are presented here. Improvements are suggested and recommendations for future work are made that could increase the success of subsequent research. The overall research is discussed with respect to the objectives stated in chapter three.

7.1 Aerial video reconnaissance

The approach of gathering training and verification data through the use of aerial video shows promise for future studies. The use of video as a means of validating remote sensing data has many benefits considering the vast area that can be covered in only a short period of time, and the ease of use of equipment. For validation of spaceborne remote sensing imagery, georeferencing is the most challenging aspect of an aerial video survey. A two step approach used in this research addressed this problem. Using first an artificial grid to force the image from an oblique view to a near nadir view by means of a spline based image correction coupled with the maintenance of the visual perspective. Once in perspective of a near nadir view, a polynomial based correction proved capable of registering the video imagery.

While this approach showed success, improvements could be made in the actual collection of the video. It is important to ensure the oblique angle at which the ice surface

is captured is not greater than 45°, as it leaves much of the video frame unusable in the far range of the image. A normal perspective would be advantageous, if the altitude of the aircraft enables sufficient coastline is captured in each video frame. Selecting a constant viewing angle for all video acquisition would ensure total coverage and useable video frames. It would also allow conversion to the near nadir view easier, since each image would have the same viewing geometry. Care should also be taken to ensure there are sufficient numbers of coastal features present to allow for selection of ground control points.

One of the major sources of variability in this study was the time lag between the acquisition of the radar image and the aerial video. While the problem was addressed through the clustering procedure described in section 5.2.4, much of the error associated with change in the ice cover would disappear if the times of both acquisitions occurred simultaneously. However, this time difference was unavoidable in this research as both the helicopter time needed for aerial surveillance and the RADARSAT-1 image acquisition were outside control.

7.2 Radar image processing

The wavelet approach to speckle filtering is of considerable utility in research where texture is to be used. The filter leaves little evidence of artifacts of the filter size that could be detected by the texture filter, since the dilating function of the wavelet

family changes according to frequency. Traditional approaches to speckle reduction are to apply texture analysis measures before speckle reduction is performed to ensure texture information is not lost in the speckle reduction procedure. The downfall in this approach is the speckle itself could affect the texture measure.

A secondary objective of this research was to examine image texture measures in first-year ice and open water types, with the goal of selecting one with better distinguishing capabilities. Considering the five texture measure used in this research, Standard Deviation, Angular Second Moment, Correlation, Homogeneity, and Entropy, each of the texture measures performed relatively well with overall accuracies in the range of 58% and 62%. Overall, Homogeneity and Entropy texture parameters showed the highest overall accuracies, however the differences between all five with respect to each of the texture measures abilities is minimal. The reduced overall accuracy can be attributed to one class, puddle, exhibiting a very low producer's accuracy.

Selection of optimum window size and displacement vector for each of the measures showed that a 7x7 texture window is required for each of the texture measure in order to maximize the signature separability for each of the ice classes studied here. A neighborhood of 7x7 relates to an area of approximately 50 square meters. The directionally invariant displacement vector ranged between two and three pixels, which equates to between 12.5 to 18.75 meters. Features on the ice surface that add to the texture of a surface such as snow drifts or melt ponds could in reality exhibit spatial

arrangements less than the smallest texture step available and therefore be missed in the texture classification. However the periodic form of such natural phenomenon should be evident at smaller scales. Other features, such as the random pattern of thaw hole formation, as well as melt water puddles would suggest that no single texture measure is best suited to capturing this phenomenon. This is illustrated in the overall accuracies of each of the texture measures studied here.

The ice classes studied here exhibited non-normal distributions, thus requiring an approach to deal with such distributions. Histogram characterization by means of image filtering based on optimum histogram bin widths captured the distributions in the image data set. The resulting imagery proved useful in increasing the separability of the classes. It was able to capture the entire distribution of the representative training pixels as input to a classifier. While this approach was successful in this research, it facilitated the separation of each of the ice classes with varying levels of success, a review of the literature has found no other application of such a histogram characterization for image classification, with the exception of single value skewness and kurtosis measures for ice classes as reported by Gill and Valeur (1999).

Artificial neural networks allowed the non-normal distributions of the ice classes to be captured and used in a classification algorithm. While many of the operational approaches to sea ice classification use unsupervised clustering algorithms, which are labeled *via* traditional knowledge, a trained neural network is capable of classification of

an unseen image, based on the classifiers ability to generalize. A trained neural network should be tested on an independent image to assess the ability of this approach to be used in an “Unsupervised” operational approach. Verification data should be collected at the time of image acquisition to test the accuracy of the approach on the new image. The neural network uses its learned responses as the knowledge in this approach. A multi layered perceptron model (MLP) was used to classify each of the five texture-based data sets. Each of the neural networks was able to learn the input data set and reach an acceptable level of error. The elevated total error of each network could be attributed to similarities in surface ice types, as well as the variability associated with the change in ice cover due to melt, between the two acquisition times. It is speculated that if this variability was removed from the approach then the total error of each neural network would be improved, and the resulting image classification accuracies would improve as well.

Further work into the architecture of the MLP model could prove useful. In this study a single hidden layer was used to allow the neural network to generalize. A higher number of hidden layers may allow the network to discriminate between differences in ice class but not be able to generalize new inputs. An extensive study exploring different network architectures could improve the results of ice type classification.

7.3 First-year ice mapping capabilities

The principal objective of this research was to develop a methodology to accurately classify the subdivision of first-year ice types during the spring melt period. Users of the coastal environment need accurate information about the type and extent of ice during the spring melt period to safely work and protect valuable assets, such as aquaculture infrastructure.

During the melt process, ice proceeds from the snow covered class which is evident most of the winter months, through puddle ice at the beginning of melt, further progressing to flooded, rotten and finally open water ends the life cycle of the consolidated ice cover. At any time during the process, if the ice cover is subject to sufficient mechanical energy, it can break into ice particles called brash that are free to move about the coastal zone with wind and wave action and present problems to aquaculture sites.

With respect to the six classes identified in the spring melt environment, the methodology showed varying levels of success with respect to end user's accuracies. The measure of user's accuracy is designed to assess the "useability" of the resultant ice classifications by an operational end user. Of the six classes identified in this study, brash, perhaps the most important ice class for aquaculture facilities was classified with a very high user's accuracy, ranging between 80 and 99 %. The Kappa statistic for this ice

class ranged from 0.79 and 0.99. In decreasing order of classification user's accuracy were open water (79 – 82%), puddle (60-65%), snow cover (40-50%), rotten (38-44%), and flooded (35-40 %).

The lower accuracies for snow cover and flooded can be attributed to confusion of these classes with puddle, and to some extent the confusion of flooded with open water. Considering the snow cover inaccuracies, it is suggested that the saturation of the snow cover with melt water had begun and puddles were beginning to form, resulting in the confusion with the puddle ice class. Also, the flooded class may have begun drying with the emergence of thaw holes with remnant snow cover, resulting in a surface similar to that of puddle.

In the presence of high winds, standing water on flooded ice could exhibit waves sufficiently large to allow the surface to appear as open water, thus explaining the confusion of these classes. Rotten produces suppressed user's accuracies mainly due to confusion with open water, as described in the results section. This error is mainly due to change in the melting process and variability in the cluster label for this class. While the last three classes show low user's accuracies, and taking into consideration the open water accuracies, the end user can be quite certain that ice is present as opposed to open water but with less certainty in the type of ice that is present.

Many errors associated with classification can be attributed to change in the ice cover from the time of acquisition of training data and the acquisition of the radar image itself. Also, similarities in surfaces during the transitions between one ice class and another such as flooded and puddle can contribute to the commission errors. Flooded and puddle are very similar in appearance and the distinction was made based on the amount of standing water on the ice surface. Further work in this area should consider these two ice classes as one, or a more objective means of separating the two, based on *in situ* field measurements of the amount of standing water within a neighborhood. If we consider the ASM texture measure as an example of combining these classes, the overall accuracy increases from 59% to 70% and the user's accuracy for the flooded/puddle ice class approaches 87%, increased from individual user's accuracies of 62% and 36% as separate ice classes.

Table 7.1 Accuracy assessment of ASM texture measure with flooded and puddle combined

Classified	Reference						
	SC	FL/PD	RT	OW	BR	Total	UA (%)
SC	140	167	0	2	0	309	45
FL/PD	44	700	10	150	0	805	87
RT	0	1	275	344	78	698	39
OW	0	1	167	1040	14	1222	85
BR	0	0	1	3	87	91	96
Total	184	869	453	1540	179	3225	
PA (%)	76	81	61	68	49		
Overall Accuracy 70%							

The accuracies reported for each of the texture measures indicate the ability of the methodology to accurately classify the ice types studied. This research has addressed the

objectives set out and proved the incorporation of new image analysis techniques, namely, wavelet analysis and histogram binning to be very useful in further extending the capabilities of SAR imagery in the identification of ice classes.

8.0 Conclusion

The applicability of RADARSAT imagery for first-year ice classification in the coastal environment has been investigated. While traditional sea ice classification has been dedicated to navigational problems, problems associated with ice in the coastal zone prove significant, as is evident in the concerns associated with ice in the Bay d'Espoir region of Newfoundland and Labrador with respect to the aquaculture industry.

The classification approach used here addresses the needs of users of the coastal zone with respect to the need for adequate, accurate information about the type and extent of ice during the spring melt. It employs new approaches to radar image processing, including wavelet based speckle reduction, selection of training data using aerial video, and a unique approach to histogram characterization. Each procedure is integral to processing of information for use in an artificial neural network image classification.

The study of texture revealed that each of the five measures, namely, homogeneity, angular second moment, standard deviation, correlation, and entropy are equally capable of classifying the six ice types studied. Overall accuracies of the range of 60% were achieved for each texture measure; more importantly kappa statistics showed ranges from 0.45 to 0.48, which indicate the methodology is 45% to 48% better than chance at identifying the ice classes. Classification accuracy can be improved to 70% by combining two of the ice classes studied, namely flooded and puddle, indicating the similarities in the surface characteristics of these ice classes.

The complex surface nature of ice types during spring melt resulted in non-normal distributions of the signature statistics. The ability of artificial neural networks to handle non-normal feature statistics was instrumental in the methodology's success. A multi-layer perceptron model with one hidden layer was able to distinguish between the six ice classes with varying levels of success. Brash ice, of most importance to the aquaculture industry, was successfully classified with accuracies approaching 100%. Further results were promising, with the methodology accurately distinguishing ice from open water and further sub-classifying ice into brash, snow covered, flooded, puddle, and rotten.

9.0 References

- Atkinson, P. M. and A. R. L. Tatnall, 1997. Neural networks in remote sensing, *International Journal of Remote Sensing*, Vol. 18, No. 4, pp 699-709.
- Baraldi, A. and F. Parmiggiani, 1995. An investigation of the textural characteristics associated with grey level cooccurrence matrix statistical parameters, *IEEE Transactions on Geoscience and Remote Sensing*, Vol. 33, No. 2, pp. 293-304.
- Barber, D. G., 1989. Texture Measures for SAR Sea Ice Discrimination: An evaluation of Univariate Statistical Distributions, *Earth Observations Lab Technical Report*, Series ISTS-EOL-TR89-005, Department of Geography, University of Waterloo, Waterloo: publisher, 56p.
- Barber, D. G. and E. F. LeDrew, 1989. Multivariate Analysis of Texture Statistics for SAR Sea Ice Discrimination, Proceedings: *IGARSS '89 12th Canadian Symposium on Remote Sensing*, Vol. 2, pp. 759 – 762.
- Barber, D. and E. LeDrew, 1991. SAR sea ice discrimination using texture statistics: a multivariate approach, *Photogrammetric Engineering and Remote Sensing*, Vol. 57, No. 4, pp. 385-395.
- Barber, D., M. Shokr, R. Fernandes, E. Soulis, D. Flett and E. LeDrew, 1993. A comparison of second order classifiers for SAR sea ice discrimination, *Photogrammetric Engineering and Remote Sensing*, Vol. 59, No. 9, pp 1397-1408.
- Cavalieri, D. J., P. Gloersen and W. J. Campbell, 1984. Determination of sea ice parameters from Nimbus 7 SMMR, *Journal of Geophysical Research*, Vol. 89, pp 5355-5369.
- Canadian Ice Service, 1997. National Atlas of Canada, Retrieved June 1997, from Natural Resources Canada Web site, <http://alert.ccm.emr.ca>.
- Congalton, R., 1991. A Review of Assessing the Accuracy of Classifications of Remotely Sensed Data, *Remote Sensing of Environment*, Vol. 37, pp 35-46.
- Dong, Y., B. C. Forster, A. K. Milne and G. A. Morgan, 1998. Speckle suppression using recursive wavelet transforms, *International Journal of Remote Sensing*, Vol. 10, No. 2, pp 317-330.
- Donoho, D. L., 1995. De-Noising by soft-thresholding, *IEEE Transaction of Information Theory*, Vol. 41, pp 613-627.

- Drobot, S. D. and M. R. Anderson, 2000. Spaceborne microwave remote sensing of arctic sea ice during spring, *Professional Geographer*, Vol. 52, No. 2, pp 315-322.
- Eckes, C. and B. Fritzke, 2001. Classification of sea-ice with neural networks – results of the EU research project ICE ROUTES, *Institut Fur Neuroinformatik, Ruhr-Universitat Bochum, FRG, Internal Report IR-INI 2001-02*, ISSN. 0943-2752.
- Eppler D. T., L. D. Farmer, A. W. Lohanick, M. R. Andereson, D. J. Cavalieri, J. Comiso, P. Gloersen, C. Garrity, T. C. Grenfell, M. Hallikainen, J. A. Maslanik, C. Matzler, R. A. Melloh, I. Rubinstein and C.T. Swift, 1994. Passive Microwave Signatures of Sea Ice, *Microwave Remote Sensing of Sea Ice*, Frank D. Carsey, Editor.
- Falkingham, J., 1992. RADARSAT and Ice information, Chapter 11, *Remote Sensing of Sea Ice*, Simon Haykin *et al.* editors, John Wiley and Sons.
- Foody, G. M. and M. K. Arora, 1997. An evaluation of some factors affecting the accuracy of classification by artificial neural network, *International Journal of Remote Sensing*, Vol. 18, No. 4. pp 799-810.
- Foody, G. M., 1995. Land cover classification by artificial neural network with ancillary information, *International Journal of Geographic Information Systems*, Vol. 9, pp. 527-542
- Franke, R., 1985. Thin plate spline with tension, *Computer Aided Geometrical Design.*, Vol. 2, pp 87-95.
- Frost, V. S., K. S. Shanmugan and J. C. Holtzman, 1984. The influence of sensor and flight parameters on texture in radar images, *IEEE Transactions on Geoscience and Remote Sensing*, Vol. 25, No. 5, pp 440-448.
- Gagnon, L., 1999. Wavelet Filtering of speckle noise- some numerical results, *Presented at conference Vision Interface '99, Trois- Rivieres, Quebec, Canada*, May 1999. 8 pages.
- Gagnon, L. and F. D. Smaili, 1996. Speckle Noise Reduction of Airborne SAR Images with Symmetric Daubechies Wavelets, *SPIE proceedings, Wavelet Applications in signal and Image processing IV*, No. 2759.
- Gill, R. S. and H. H. Valeur, 1999. Ice cover discrimination in the Greenland waters using first-order texture parameters of ERS SAR images, *International Journal of remote Sensing*, Vol. 20, No. 2, pp. 373-385.

- Guo, H., J. E. Odegard, M. Lang, R. A. Gopinath, I. Selesnick and C. S. Burrus, 1994. Wavelet Based Speckle Reduction with Application to SAR Based ATD/R, *Proceedings of International Conference of Image Processing*, Austin, TX., November 1994.
- Guindon, B., D. G. Goodenough and P.M. Teillet, 1982. The Role of Digital Terrain Models in the Remote Sensing of Forests, *Canadian Journal Of Remote Sensing*, Vol. 8, pp 4-16.
- Hara, Y., R. G. Atkins, S. H. Yueh, R. T. Shin and J. A. Kong, 1994. Application of neural networks to radar image classification, *IEEE Transactions on Geoscience and Remote Sensing*, Vol. 32, pp. 100-109.
- Haralick, R. M., K. Shanmugan and I. Dinstein, 1973. Textural features for image classification, *IEEE Transactions on Systems, Man and Cybernetics*, Vol. 6, pp 610-621.
- Holmes, Q. A., D. R. Nuesch and R. A. Shuchman, 1984. Textural analysis and real-time classification of sea-ice types using digital SAR data, *IEEE transactions on Geoscience and Remote Sensing*. Vol. 22, pp 113 – 120.
- Jensen, J., 1996, *Introductory Digital Image Processing: A remote Sensing Perspective*, second edition, Prentice-Hall, Upper Saddle River, New Jersey.
- Kanellopoulos, I. and G. G. Wilkinson, 1997. Strategies and best practice for neural network image classification, *International Journal of Remote Sensing*, Vol. 18, No. 4, pp 711-725.
- Kwok, R., E. Rignot and B. Holt, 1992. Identification of Sea Ice Types in Spaceborne Synthetic Aperture Radar Data, *Journal of Geophysical Research*, Vol. 91, No. C2, pp 2391-2402.
- Kwok, R., S. V. Nghiem, S. Martin, D. P. Winebrenner, A. J. Gow, D. K. Perovich, C. T. Swift, D. G. Barber, K. M. Golden and E. J. Knapp, 1998. Laboratory Measurements of Sea Ice: Connections to Microwave Remote Sensing, *IEEE Transactions on Geoscience and Remote Sensing*, Vol. 36, No. 5, pp 1716-1730.
- Leshkevich, G., W. Pichel, P. Clemente-Colon, R. Carey and G. Hufford, 1995. Analysis of coastal ice cover using ERS-1 SAR data, *International Journal of Remote Sensing*, Vol. 16, No. 17, pp 3459-3479.
- Lopes, A., E. Nezry, R. Touzi and H. Laur, 1993. Structure detection and statistical adaptive speckle filtering in SAR images, *International Journal of Remote Sensing*, Vol. 14, No. 9, pp. 1735-1758.

Lyden, J. D., B. A. Burns and A. L. Maffet, 1984. Characterization of sea ice types using synthetic Aperture Radar, *IEEE Transactions on Geoscience and Remote Sensing*, Vol. 22, No. 5, pp 431-439.

Lythe, M., A. Hauser and G. Wendler, 1999. Classification of sea ice types in the Ross Sea, Antarctica from SAR and AVHRR imagery, *International Journal of Remote Sensing*, Vol. 20, No. 15&16, pp 3073-3085.

Martin, F. J. and R. W. Turner, 1993. SAR speckle reduction by weighted filtering, *International Journal of Remote Sensing*, Vol. 14. No.9, pp 1759-1774.

Melling, H., 1998. Detection of features in first-year pack ice by synthetic aperture radar (SAR), *International Journal of Remote Sensing*, Vol. 19, No. 6, pp 1223-1249.

Nystuen, J. A. and F. W. Garcia, Jr., 1992. Sea ice classification using SAR backscatter statistics, *IEEE transactions on Geoscience and Remote Sensing*, Vol. 30, pp. 502-509.

Olaussen, T., O. Johannessen, and R. Karpuz. 1990. Extraction of Sea Ice Information from SAR Imagery, *IGARR '90*, pp 394-399.

Onstott, R. G., 1992. SAR and scatterometer signatures of sea ice (Chapter 5). In *Microwave Remote Sensing of Sea Ice*, F. D. Carsey Editor, Geophysical Monograph 68 (Washington, D.C.: American Geophysical Union), pp. 73-104.

Rajesh, K., C. V. Jawahar, S. Sengupta, and S. Sinha, 2001. Performance analysis of textural features for characterization and classification of SAR images, *International Journal of Remote Sensing*, Vol. 22, No. 8, pp 1555-1569.

Ramsay, B., T. Hirose, M. Manore, J. Falkingham, R. Gale, D. Barber, M. Shokr, B. Danielowicz, B. Gorman and C. Livingston, 1993. Potential of RADARSAT For Sea Ice Applications, *International Journal of Remote Sensing*, Vol. 19, No. 4, pp 352-362.

Rumelhart, D. E., G. E. Hinton and R. J. Williams, 1986. Learning internal representation by error propagation, *Parallel Distributed Processing: Explorations in the Microstructure of Cognition*, D. E. Rumelhart and J. L. McClelland Editors, Cambridge, Mass., MIT press, pp. 318-362

Rosenfield, G. and K. Fitzpatrick-Lins, 1986. A coefficient of agreement as a measure of thematic classification accuracy, *Photogrammetric Engineering and Remote Sensing*, Vol. 52, No. 2, pp 223-227.

Sandven, S., H. Gronvall, A. Seina, H. H. Valeur, M. Nizovsky, H. Steen Anderson and V. E. J. Haugen, 1998. Operational Sea Ice Monitoring by Satellites In Europe, *OSIMS Report no. 4 NERSC Technical reports*, No. 148, 91 pages.

- Sabins, F., Jr., 1997. *Remote Sensing Principles and Interpretation, Third Ed.*, W. H. Freeman and Company, New York.
- Scott, D. W., 1979. On optimal and data-based histograms, *Biometrika*, Vol. 66, No. 3, pp 605-610.
- Sheppard, N., 1998. Extraction of Beta Nought and Sigma Nought from RADARSAT CDPF products, Revision 2 - 22 May 1998, *ALTRIX systems Report No.: AS97-5001*, 8 pages.
- Shi, Z. and K. B. Fung, 1994. A comparison of digital speckle filters, *Surface and Atmospheric Remote Sensing: Technologies, Data Analysis and Interpretation, IGARSS'94*, Pasadena, Aug. 1994, Stein, T. I. (ed.), pp. 2129-2133.
- Shokr, M., 1991. An evaluation of second-order textural parameters for sea ice classification in radar images, *Journal of Geophysical Research*, Vol. 96, No. C6, pp 10625-10640.
- Shokr, M., B. Ramsay and C. Falkingham, 1996. Operational use of ERS-1 SAR Images in the Canadian Ice Monitoring Program, *International Journal of Remote Sensing*, Vol. 1, No. 4, pp. 667-682.
- Simila, M., Lepparanta, M., Granberg, H. B. and Lewis, J. E., 1992. The relation between SAR imagery and regional sea ice ridging characteristics from BEPERS-88, *International Journal of Remote Sensing*, Vol. 13, No. 8, pp 2415- 2432.
- Skriver, H., 1994. On the accuracy of estimation of ice type concentration from ERS-1 SAR images, *Sensors and Environmental Applications of Remote Sensing, Proceedings of the 14th EARSeL Symposium*, Gotteborg, Sweden, June 6-8, 1994, pp 219 –226.
- Smith, D. M., E. C. Barrett and J. C. Scott, 1996. Sea Ice type classification from ERS-1 SAR data based on grey level and texture information, *Polar Record*, Vol. 31, pp 135-146.
- Soh, L. and C. Tsatsoulis, 1999. Texture analysis of SAR sea ice imagery using gray level co-occurrence matrices, *IEEE Transactions on Geoscience and Remote Sensing*, Vol. 37, No. 2, pp 780-795.
- Soh, L. and C. Tsatsoulis, 1999. Unsupervised segmentation of ERS and RADARSAT sea ice images using multiresolution peak detection and aggregated population equalization, *International Journal of Remote Sensing*, Vol. 20, No. 15&16, pp 3087-3109.

Solaiman, B. and M. C. Mouchot, 1994. A comparative study of conventional and Neural Network classification of multispectral data, *International Geoscience and Remote Sensing Symposium, IGARSS'94, Pasadena*, pp. 1413-1416, 8-12 August.

Steffen, K. J., D. J. Key, D. J. Cavalieri, J. Comiso, P. Gloersen, K. St. Germain and I. Rubinstein, 1992. The estimation of geophysical parameters using passive microwave remote sensing of sea ice, *Geophysical Monograph Series*, Vol. 68, F. Carsey, Editor, Washington, DC: AGU, pp 201-231.

Sun, Y., A. Carlstrom and J. Askne, 1992. SAR image classification of ice in the Gulf of Bosnia, *International Journal of Remote Sensing*, Vol. 13, No. 9, pp 2489-2514.

Swain, P. H. and S. M. Davis, (ed.), 1978. *Remote Sensing: The Quantitative Approach*. New York: McGraw-Hill Book Company, 396 pages.

Tlusty, M. F., V. A. Pepper and M. R. Anderson, 1999. Environmental monitoring of finfish aquaculture sites in Bay d'Espoir, Newfoundland during the winter of 1997, *Canadian Technical Report of Fisheries and Aquatic Sciences*, No. 2273, 32 pages.

Ulaby, F., F. Kouyate, B. Brisco and T. Lee Williams, 1986. Textural information in SAR images, *IEEE Transactions on Geoscience and Remote Sensing*, Vol. 24, No. 2, pp 235-245.

Wand, M. P., 1997. Data-based choice of histogram bin width, *Statistical computing and graphics*, Vol. 51, No. 1, pp 59-64.

Wheaton, F.W., 1987. Energy in Aquatic Systems, *Aquatic Engineering*, Robert E. Krieger Publishing Company, Malabar, Florida, p 100-101.

World Meteorological Organization, 1985. WMO sea-ice nomenclature, terminology, codes and illustrated glossary, *WMO/DMM/BMO 259-TP-145*, Secretariat of the WMO, Geneva.

Zibordi, G. and M. Van Woert, 1993. Antarctic sea ice mapping using the AVHRR, *Remote Sensing of Environment*, Vol. 45, pp 155-163.

